Acta Pharmaceutica Sinica B 2025;15(8):3888−3924

Chinese Pharmaceutical Association
Institute of Materia Medica, Chinese Academy of Medical Sciences

Acta Pharmaceutica Sinica B

www.elsevier.com/locate/apsb
www.sciencedirect.com

REVIEW

Advances in immunoPET/SPECT imaging: The role of Fab and F(ab′)$_2$ fragments in theranostics

Wenpeng Huang[a,†], Jingwei Zhou[b,†], Yanchen Liu[c,†], Yihan Yang[a], Rachel J. Saladin[d], Jessica C. Hsu[d], Weibo Cai[d,*], Lei Kang[a,*]

[a]*Department of Nuclear Medicine, Peking University First Hospital, Beijing 100034, China*
[b]*Department of Plastic and Reconstructive Surgery, Shanghai Ninth People's Hospital, Shanghai Jiao Tong University School of Medicine, Shanghai 200011, China*
[c]*State Key Laboratory of Biochemical Engineering, Institute of Process Engineering, Chinese Academy of Science, Beijing 100190, China*
[d]*Departments of Radiology and Medical Physics, University of Wisconsin−Madison, Madison, WI 53705, USA*

Received 28 January 2025; received in revised form 5 April 2025; accepted 10 May 2025

KEY WORDS

ImmunoPET;
ImmunoSPECT;
Fab;
F(ab′)$_2$;
Antibody fragment;
Molecular imaging;
Therapy;
Diagnostics

Abstract With the advent of precision medicine and personalized treatment, targeted therapies have become pivotal in oncology. Noninvasive molecular imaging, especially immunoPET/SPECT, plays a crucial role in refining cancer diagnostics and treatment monitoring by visualizing biological processes at the molecular level. This review explores the dynamic field of immunoPET/SPECT imaging using Fab and F(ab′)$_2$ fragments, characterized by advantageous pharmacokinetics and swift clearance from the bloodstream, making them suitable for same-day imaging procedures. We examine contemporary strategies for radiolabeling these fragments with PET and SPECT radionuclides and discuss potential advancements and the challenges anticipated in the further development of Fab and F(ab′)$_2$ fragments. Despite the complexities involved in their development, these fragments hold significant promise for advanceing personalized cancer treatment. Keys to this advancement are innovative radiolabeling techniques, site-specific conjugation chemistries, and short-lived radionuclides, all of which are crucial for overcoming existing limitations and enhancing the clinical utility of these imaging agents. As research progresses, Fab and F(ab′)$_2$ fragments are expected to become central to the future of cancer diagnostics and therapeutic monitoring, thereby improving patient management and contributing significantly to the evolution of personalized medicine.

*Corresponding authors.
E-mail addresses: wcai@uwhealth.org (Weibo Cai), kanglei@bjmu.edu.cn (Lei Kang).
[†]These authors made equal contributions to this work.
Peer review under the responsibility of Chinese Pharmaceutical Association and Institute of Materia Medica, Chinese Academy of Medical Sciences.

https://doi.org/10.1016/j.apsb.2025.05.030

1. Introduction

Cancer mortality rates have continued to decline, attributed to advances in prevention, early detection, and treatment. However, the increasing incidence rates of six major cancers, including breast, pancreatic, and prostate cancers—which have seen annual increases of between 0.6% and 3%—pose significant challenges to global healthcare systems[1]. Chemotherapy remains a cornerstone of clinical cancer treatment, yet its long-term use can result in multi-drug resistance, bone marrow suppression, and other severe side effects. Consequently, the development of more effective treatment options and precise diagnostic strategies for cancer remains a critical priority.

As the molecular pathogenesis of cancers becomes clearer and our understanding of the host immune system deepens, the development of molecularly targeted therapies—such as small-molecule inhibitors and monoclonal antibodies (mAbs)—and immunotherapies, including immune checkpoint inhibitors, has advanced significantly. These targeted therapies enhance drug delivery to tumor sites, improving therapeutic outcomes and minimizing side effects on non-targeted cells. Monoclonal antibodies natural ligands with high specificity and affinity, are central to research in targeted tumor therapy. The effectiveness of mAbs in cancer treatment is influenced by their homology with human proteins, strong affinity for tumor-associated antigens, high solubility, stability, and the absence of protease-sensitive domains[2]. Most major pharmaceutical companies are actively pursuing antibody development programs.

Computed tomography (CT) and magnetic resonance imaging (MRI) are extensively employed for anatomical imaging, delivering high-resolution visualization of tissue structures. However, their utility in detecting molecular and cellular alterations within tumors is limited. These modalities primarily yield static images, making them less effective for tracking dynamic processes such as receptor expression or responses to treatment. Positron emission tomography (PET) and single-photon emission computed tomography (SPECT), utilizing tracers like [^{18}F]-fluorodeoxyglucose (FDG) or [^{99m}Tc]Tc-MDP, are established methods for metabolic and functional imaging. Despite their widespread use, these tracers lack specificity, offering only limited insights into distinct molecular targets or tumor phenotypes.

Noninvasive molecular imaging is defined as "the visualization, characterization, and measurement of biological processes at molecular and cellular levels in humans and other living systems"[3]. The integration of innovative molecular imaging approaches into the standard diagnostic arsenal is crucial for advancing the clinical management of both cancerous and noncancerous diseases. Molecular imaging probes based on antibodies have an essential role in assessing receptor expression and deriving *in vivo* pharmacokinetic profiles. As medicine shifts from empirical approaches to more precise molecular-based strategies, there is a burgeoning demand for corresponding molecular diagnostics. An increasing array of molecular imaging tracers has become an essential component of the clinical toolkit. These tracers, which include small organic compounds, peptides, proteins, protein scaffolds, mAbs, and antibody-derived fragments, consist fundamentally of a targeting vehicle coupled to a detection label. In recent years, the development of diverse molecular imaging tracers has expanded across various (pre)clinical research domains such as oncology, cardiology, neurology, and rheumatology, playing a critical role in both the treatment and diagnosis of a wide range of diseases.

ImmunoPET/SPECT represents a paradigm-shifting modality in molecular imaging, fundamentally involving the combination of an antibody or a related molecule with a diagnostic positron-emitting or gamma ray-emitting radionuclide to image specific antigens *in vivo*[4,5]. While the fusion of radionuclides with mAbs for imaging or therapeutic purposes is established, there has been a renewed interest in this approach. This resurgence is driven by advances in antibody engineering, enhancements in radiochemistry and conjugation techniques, the increasing availability of diagnostic PET radionuclides, and the development of novel site-specific chemical conjugation methods[6,7].

In practice, after extensive clinical application and research, imaging agents based on completely intact mAbs have encountered significant limitations, primarily due to their large size (four polypeptide chains, approximately 150 kDa), which exceeds the renal cutoff for glomerular filtration (60 kDa). Additionally, the presence of an Fc-effector part increases retention through interactions with the neonatal Fc receptor, which shields fragment crystallizable (Fc)-bearing molecules from default degradation pathways[8,9]. These agents exhibit slow pharmacokinetics and prolonged circulation times that can often last up to three weeks. Consequently, longer-lived radionuclides such as ^{89}Zr and ^{124}I are required for imaging, but these are less than ideal for clinical use due to higher radiation doses and extended waiting periods for imaging results. Furthermore, the substantial size of intact mAbs generally leads to liver clearance, which complicates the imaging of liver diseases. Thus, they are suboptimal for imaging purposes[10,11]. With advancements in genetic engineering and a deeper understanding of antibody structures, the focus has shifted toward miniaturized and modular antibody fragments, now a principal research area in tumor immunotherapy. The enzymatic digestion of mAbs to produce Fab or F(ab′)$_2$ fragments is increasingly favored in therapeutic applications where Fc-mediated effector functions are unnecessary or harmful. These fragments, devoid of the immunoglobulin Fc region, are cleared more rapidly from the blood, exhibit lower immunogenicity, and have a shortened half-life, reducing dosage requirements and minimizing the risk of immune reactions against the probe[12]. Fab and F(ab′)$_2$ fragments are rapidly cleared through the kidneys, resulting in shorter imaging windows. This characteristic supports the use of shorter-lived radionuclides such as Copper-64 (^{64}Cu), Gallium-68 (^{68}Ga), and Fluorine-18 (^{18}F), which are advantageous for minimizing radiation exposure and enabling same-day imaging[13–15]. This has spurred the development of novel immunoPET/SPECT probes[16]. The rapid clearance from the blood allows for earlier imaging post-injection, leading to higher signal-to-background ratios and substantial practical advantages for routine clinical use. Early imaging is compatible with short-lived radioisotopes, which enhances radioprotection and dosimetry and

reduces potential adverse events[17]. Consequently, an increasing number of researchers and institutions are actively exploring the use of antibody fragments in tumor therapy and imaging[18].

In this review, we first explore recent advancements in the field of immunoPET/SPECT using Fab and $F(ab')_2$ fragments. We then discuss current methodologies for radiolabeling these fragments. Additionally, we provide a comprehensive summary and analysis of the progress and applications of Fab and $F(ab')_2$ fragments in targeted cancer imaging over the past decade (Table 1)[10,11,13−15,19−69,]. Finally, we offer predictions on the future developments and challenges of Fab and $F(ab')_2$ fragments (Fig. 1).

2. Structure of Fab and $F(ab')_2$ fragments

Immunoglobulins, produced as antibodies by the vertebrate immune system in response to pathogens or foreign particles, are complex glycoproteins. As research into antibodies has deepened, the understanding of their structure and function has expanded. Typically Y-shaped, these molecules consist of polypeptide subunits with identical heavy and light chains. The arms of the molecule are known as Fab domains, while the tail, referred to as the Fc domain, plays a role in activating immune cascades. Generally, the heavy chain comprises one variable region and three constant regions, labeled CH1, CH2, and CH3. The light chain is composed of one variable region and one constant region, with each variable region containing four framework regions and three complementarity-determining regions (CDRs). The six CDRs from both heavy and light chains form the antigen-binding site, which is crucial for the antibody's specificity.

With advancements in immunology and molecular biology, antibody fragments such as Fab and $F(ab')_2$ can be produced through chemical/enzymatic digestion or genetic engineering, retaining their antigen-specificity[70−74]. These fragments typically range from 7 to 100 kDa, depending on the type. The production of Fab and $F(ab')_2$ fragments through papain digestion is well-established, straightforward, and requires minimal optimization. In contrast, the preparation of other antibody fragments like VHH, VNAR, or scFv demands extensive expertise and is adaptable to multiple antibodies of various origins and subtypes (Figs. 2 and 3). Fab agents, as the oldest class of mAb fragment therapeutics, are evidenced by the fact that all eight fragment therapeutics that entered clinical development before 1995 were Fabs[75]. They also serve as vectors and targeting moieties in targeted drug delivery systems for administering anti-tumor drugs[76−79]. Each Fab fragment, approximately 50 kDa in size, is composed of one VH and one VL chain connected by disulfide bonds and contains a single antigen-binding site[80,81]. Despite their relative simplicity, the number of Fab and $F(ab')_2$ fragments in clinical development remains significantly smaller than that of intact antibodies.

The $F(ab')_2$ fragment includes interchain disulfide bonds that can be reduced to reveal free thiol groups, providing reactive sites for radionuclide attachment *via* maleimide-based conjugation. This structural characteristic is particularly valuable for labeling approaches, such as those involving Lutetium-177 (^{177}Lu), which are further detailed in subsequent chapters. Additionally, both Fab and $F(ab')_2$ fragments possess primary amine groups on lysine residues, which can be targeted for conjugation through *N*-hydroxysuccinimide (NHS) esters. The availability of these amine groups depends on the fragment's structure and the accessibility of these reactive sites to the labeling reagent.

3. Concept of immunoPET/SPECT

Compared to computed tomography (CT), optical, ultrasound, and photo-acoustic imaging, immunoPET/SPECT has become increasingly vital in the diagnosis, staging, and monitoring of cancer treatment response, leading to its rapid development in recent years. Traditional biopsy methods, while informative, are invasive and can cause significant discomfort to patients. Furthermore, biopsies may yield diagnostic inaccuracies due to the heterogeneous nature of receptors within a tumor mass. In contrast, immunoPET/SPECT imaging is minimally invasive and offers more precise quantitative data about both the primary tumor mass and secondary lesions.

Compared to [^{18}F]FDG PET and [^{99m}Tc]Tc-MDP SPECT, which are commonly used in clinical practice to monitor metabolic uptake, immunoPET/SPECT provides crucial biomarker information by directly targeting specific receptors. Key considerations in constructing imaging tracers include half-life, permeability, and biodistribution. Unlike mAbs, Fab and $F(ab')_2$ fragments, which have a shorter half-life and enhanced permeability, are better suited for tumor imaging. On one hand, due to their significantly smaller size, Fab and $F(ab')_2$ fragments are primarily excreted *via* the kidneys and are neither substantially metabolized nor retained by the liver[34]. On the other hand, lacking the Fc region, these fragments do not bind to the Fc receptor, leading to reduced blood circulation time and a lower imaging background.

Numerous studies have demonstrated the effectiveness of Fab and $F(ab')_2$ fragment-based immunoPET/SPECT in detecting a wide range of diseases. This technology is extensively utilized for several key purposes: (1) non-invasive detection of tumors; (2) real-time guidance during surgical procedures; (3) monitoring the expression status of tumorigenic receptors, tumor development, and prognosis of tumor treatment. To date, its most frequent application has been in imaging tumors associated with overexpressed antigens, particularly focusing on receptor tyrosine kinases (RTK) and clusters of differentiation (CD) (Fig. 4). An emerging application of immunoPET/SPECT imaging is the direct targeting of pathogen-specific antigens on viruses, bacteria, and fungi. The expanding use of antibody fragments further positions immunoPET/SPECT as an invaluable diagnostic tool for monitoring the effectiveness of antibody-based therapies.

4. Labeling strategies and applications

4.1. Labeling strategies

In the realm of nuclear imaging with Fab and $F(ab')_2$ fragments, targeted fragments are chemically bonded with radionuclides through a bifunctional chelator, forming a radioimmunoconjugate that enables precise tumor visualization. Various PET and SPECT radionuclides are utilized for this purpose. The choice of radionuclide and its physical properties—such as half-life, decay characteristics, and chemical compatibility for labeling—dictate the appropriate fragment and labeling approach. The selection of the labeling strategy hinges on the specific radionuclide and the chemical functionalities present on the fragment for effective conjugation. A critical factor in successful tracer labeling is aligning the radionuclide's half-life with the biological dynamics of the target process, ensuring optimal tracer accumulation for effective imaging.

Due to the intricate noncovalent bonds that define the structures of Fab and $F(ab')_2$ fragments, the conditions during the radiolabeling process, such as extreme temperatures, pH variations, and reducing environments, can compromise their structural integrity. And maintaining mild labeling conditions is essential to preserve the integrity and functionality of these fragments. Although higher temperatures can accelerate labeling kinetics, they also pose the risk of antibody denaturation, which can result in diminished binding affinity and altered biodistribution[82,83]. Thus, choosing a suitable radiolabeling approach is crucial to maintain the affinity and specificity of the antibody fragment. The radionuclide must be covalently attached to the fragment and remain both kinetically and thermodynamically stable throughout the imaging duration. Moreover, several factors such as the chelate's position on the fragment, the type of chelate used, the number of chelators attached, and the chelate's size relative to the fragment can influence the targeting efficacy of the fragment.

Labeling strategies predominantly utilize the reactive primary amine groups found on lysine residues or the thiol groups on cysteines for conjugation. For instance, cysteine residues often form disulfide bonds within proteins. In $F(ab')_2$ or Fab fragments, these cysteines can be modified to yield free thiol groups suitable for conjugation. Through mild reduction, cysteine thiols are generated, which can then swiftly react with a maleimide-containing label at a pH between 6.5 and 7.5 to form a stable thioether linkage.

4.2. *^{18}F labeling*

^{18}F is the radionuclide of choice for PET imaging due to its optimal characteristics, including high positron yield, low positron energy, a convenient half-life of approximately 2 h, and its routine production in cyclotrons by proton bombardment of $[^{18}O]H_2O$ to generate [^{18}F]fluoride. To radiolabel antibody fragments, various [^{18}F]-labeled prosthetic groups can be used, circumventing the harsh conditions typically associated with direct labeling. While prosthetic group labeling introduces additional steps in preparation and purification, it avoids direct exposure of the fragments to extreme conditions. Initial studies successfully labeled $F(ab')_2$ fragments using para-[^{18}F]fluorophenacyl bromide and the *N*-hydroxysuccinimide ester of [^{18}F]fluorobenzoate, targeting lysine residues for conjugation[84,85].

Additionally, aluminum chelate complexes, particularly the aluminum-[^{18}F]fluoride ([^{18}F]AlF) method developed by McBride et al.[86], have become prominent. This technique involves reacting a bifunctional chelator with [^{18}F]AlF, produced *in situ* from ^{18}F and $AlCl_3$, and can be applied before or after conjugating the chelator to the target molecule. This method enhances radiochemical yields (RCY) and molar activities, streamlining the labeling process[13].

Enzymatic approaches have also been employed, with the lipoic acid ligase (LplA) enzyme catalyzing the site-selective attachment of [^{18}F]fluorooctanoic acid ([^{18}F]FA) to a lysine residue within a specific peptide sequence on the antibody fragment that targets the urokinase plasminogen activator receptor[87].

Recent developments in labeling strategies have leveraged click chemistry for its efficiency and speed. Various reactions such as the 1,3-dipolar azide−alkyne cycloaddition catalyzed by copper, strain-promoted azide−alkyne cycloaddition (SPAAC), Staudinger ligation, and inverse electron demand Diels−Alder (IEDDA) reactions have been explored for the quick and efficient bioconjugation of radiolabeled prosthetic groups to biomolecules[88,89].

4.3. *^{64}Cu, ^{124}I, ^{89}Zr, ^{68}Ga and ^{44}Sc labeling*

The half-life of ^{64}Cu (12.7 h) aligns well with the imaging requirements for larger antibody fragments like Fab and $F(ab')_2$. The chelation techniques using 1,4,7,10-tetraazacyclododecane-1,4,7,10-tetraacetic acid (DOTA) and 1,4,7-triazacyclononane-1,4,7-triacetic acid (NOTA) have traditionally been employed for ^{64}Cu labeling of fragments[90,91]. [^{64}Cu]Cu-DOTA labeled antibodies fragments, however, have exhibited high levels of radioactivity in circulation and nonspecific uptake in the kidney, liver, and spleen. NOTA chelators, forming more stable copper complexes in shorter labeling durations, have shown reduced nonspecific uptake in the liver and spleen[92,93], making them the preferred choice for ^{64}Cu labeling of fragments.

Iodine-124 (^{124}I), a positron-emitting radiotracer with a prolonged half-life of approximately 4.18 days, enhances the duration of imaging capabilities. It can be seamlessly incorporated into antibodies as well as Fab and $F(ab')_2$ fragments by iodinating tyrosine residues. This method preserves both the structural integrity and the binding specificity of these molecules, thereby bypassing the potential structural alterations induced by chelators. However, the primary drawback of using ^{124}I lies in its tendency to undergo deiodination, potentially leading to unwanted iodine accumulation in the thyroid. Consequently, robust thyroid-blocking measures are essential to counteract this risk effectively.

Zirconium-89 (^{89}Zr), with a half-life of 78.41 h, is typically chelated using the Desferrioxamine (DFO) ligand. However, due to DFO's hexadentate coordination, which falls short of the octadentate requirement for ^{89}Zr, the binding is suboptimal. This incomplete coordination compromises *in vivo* stability, leading to the dissociation of ^{89}Zr from the DFO complex and subsequent accumulation in bones, as ^{89}Zr has a high affinity for hydroxyapatite. This results in an elevated radiation dose to healthy bone tissue[94]. To mitigate these challenges, modified DFO derivatives have been developed, offering eight coordination sites for ^{89}Zr, thereby significantly enhancing the stability of the chelate and reducing bone uptake[95].

The exploration of shorter-lived radiometals like ^{68}Ga (half-life of 67.7 min) and Scandium-44 (^{44}Sc, half-life of 3.9 h) is becoming more prevalent due to their pharmacokinetic compatibility with Fab and $F(ab')_2$ fragments, facilitating same-day imaging. ^{68}Ga is particularly advantageous for radiolabeling because it can be sourced from a ^{68}Ge/^{68}Ga generator, eliminating the need for cyclotron facilities. While [^{68}Ga]Ga-DOTA labeling typically requires elevated temperatures for efficient reaction, NOTA chelators offer a more feasible option for direct ^{68}Ga labeling of Fab and $F(ab')_2$ fragments at milder conditions[15,28]. Currently, ^{44}Sc is garnering interest due to its high positron yield, and flexible production methods[96]. Typically produced from ^{44}Ca in a cyclotron[97], there is potential for more convenient production *via* a ^{44}Ti/^{44}Sc generator system[98], aligning well with the imaging duration required for antibody fragment studies.

4.4. *^{99m}Tc, ^{111}In, and ^{177}Lu labeling*

Technetium-99m (^{99m}Tc) is a highly utilized radioisotope in medical imaging due to its short half-life of approximately 6 h and the emission of gamma rays with a moderate energy of 140 keV, making it ideal for gamma camera imaging. Its short half-life paired with effective imaging characteristics allows for the labeling of Fab and $F(ab')_2$ fragments. Facca et al.[33] successfully labeled Fab fragment conjugates with ^{99m}Tc-tricarbonyl complex

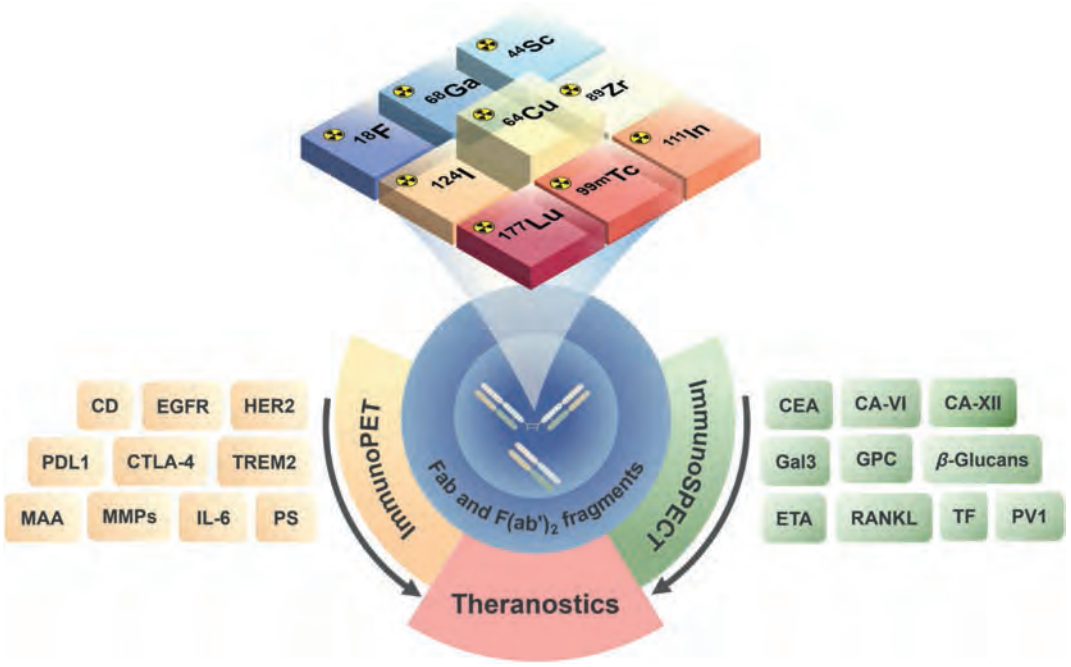

Figure 1 ImmunoPET/SPECT imaging of Fab and F(ab′)$_2$ fragments. CD, cluster of differentiation; CTLA-4, cytotoxic T-lymphocyte-associated protein 4; CEA, carcinoembryonic antigen; CA−VI, carbonic anhydrase VI; CA-XII, carbonic anhydrase XII; EGFR, epidermal growth factor receptor; ETA, endothelin A receptor; Her2, human epidermal growth factor receptor 2; GPC, glypican; Gal3, galectin 3; IL-6, interleukin-6; MAA, malondialdehyde-acetaldehyde; MMPs, matrix metalloproteinases; PDL1, programmed death-ligand 1; PS, phosphatidylserine; PV1, plasmalemma vesicle associated protein-1; RANKL, the receptor activator of nuclear factor kappa B ligand; TF, transferrin; TREM2, triggering receptor expressed on myeloid cells 2; TNC, tenascin-C.

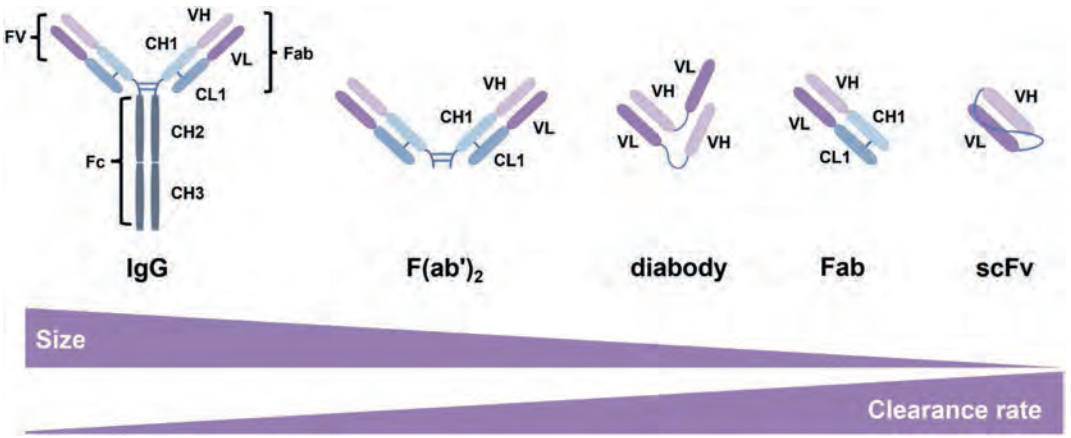

Figure 2 Antibody fragment types. Depiction of a full-sized antibody along with various types of antibody fragments. lgG, immunoglobulin; CH, constant heavy chain; CL, constant light chain; scFv, single chain variable fragment; VH, variable heavy chain; VL, variable light chain.

[^{99m}Tc(CO)$_3$(H$_2$O)$_3$]+, using an IsoLink® kit. Additionally, the HYNIC (hydrazinonicotinamide) chelation method has proven to be effective for stably labeling Fab fragments with ^{99m}Tc[64]. Other research has involved conjugating Fab and F(ab′)$_2$ fragments with the chelator MAG$_3$ (mercaptoacetyltriglycine) using NHS-MAG$_3$ ester, which provides a reactive ester for coupling to the amino groups on the antibody fragments, further enhancing the versatility and efficacy of ^{99m}Tc in targeted imaging[25,61].

Indium-111 (^{111}In), with its substantial half-life of about 2.8 days, emits gamma rays at energies of 171 and 245 keV, making it an optimal choice for immunoSPECT imaging. This isotope's decay characteristics enable extended imaging sessions, which are crucial for detailed studies. For ^{111}In labeling, the chelator CHX-A″-DTPA is preferred due to its strong affinity for ^{111}In. It effectively binds to the amino acid residues like lysine on Fab and F(ab′)$_2$ fragments through the carboxyl groups in its structure[36,62].

^{177}Lu primarily decays by emitting beta particles (electrons) and has a relatively long half-life of about 6.65 days. This radionuclide also emits gamma rays during its decay, allowing us to monitor its distribution within a patient's body using an external gamma camera. This capability is instrumental in evaluating the biodistribution and therapeutic efficacy of radiopharmaceuticals

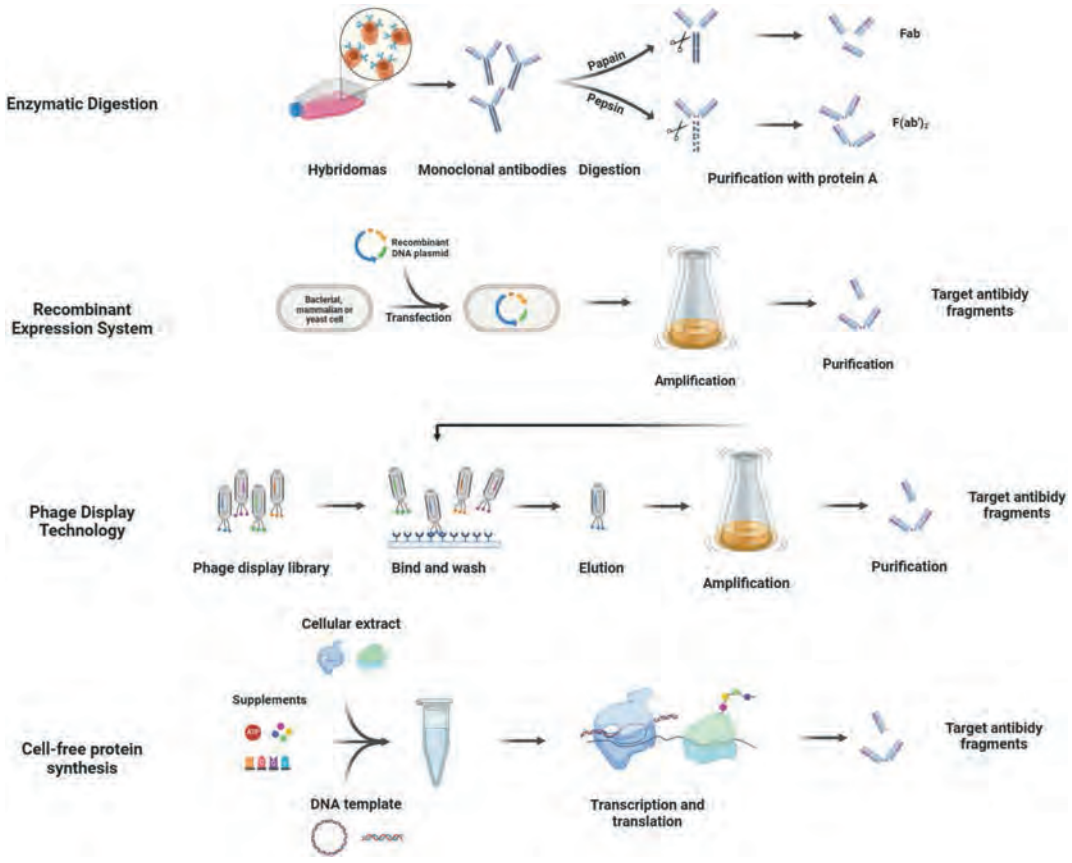

Figure 3 Flowchart depicting the production process of Fab and $F(ab')_2$ fragments.

during treatment. For labeling $F(ab')_2$ fragments, ^{177}Lu is commonly conjugated with DOTA or the newer bifunctional chelating agent DOTAGA anhydride, which are both noted for their widespread application[23,26]. The stability provided by DOTA not only ensures the retention of radioactivity within the target sites but also enhances the quality and safety of the imaging process, minimizing undesired radiolabeling in the body.

5. ImmunoPET/SPECT imaging targeting different targets

5.1. Receptor tyrosine kinases

Receptor tyrosine kinases (RTKs) are a crucial family of integral cell surface membrane receptors that initiate diverse intracellular signaling cascades in response to extracellular stimuli. Their pivotal role in pro-growth signaling networks makes them key players in various cellular phenotypes and in the regulation of essential processes in endothelial biology, including growth, proliferation, migration, differentiation, and angiogenesis[99–101]. Indeed, mAbs and small-molecule tyrosine kinase inhibitors (TKIs) that target RTKs or their ligands represent the most common forms of targeted cancer therapies, reflecting the significant therapeutic potential of modulating RTK activity.

5.1.1. Epidermal growth factor receptor

The epidermal growth factor receptor (EGFR), a member of the receptor tyrosine kinase family, can be activated through ligand binding, overexpression, or mutation. It is widely recognized for its role in promoting oncogenic activities *via* its tyrosine kinase function across various human cancers. Consequently, a substantial number of EGFR inhibitors have been developed for cancer therapy[102]. Among these, several mAbs such as cetuximab, panitumumab, and nimotuzumab target the extracellular domain of EGFR, while TKIs like erlotinib focus on the intracellular domain. These therapies have been approved for the treatment of cancers expressing high levels of EGFR, showcasing the critical therapeutic value of targeting EGFR pathways.

Colorectal cancer (CRC) represents a significant complication of inflammatory bowel disease (IBD), with patients exhibiting a heightened incidence due to chronic inflammation that escalates the risk of neoplastic transformation. Turker et al.[14] have developed a novel EGFR-targeted PET probe, utilizing cetuximab $F(ab')_2$ fragments conjugated with DOTA and labeled with ^{64}Cu. This probe was designed to differentiate between neoplastic and inflamed tissues in CRC models. Demonstrating high specificity and maintaining impressive target-to-background ratios (TBR) in colitis settings (3.78 ± 0.06), the probe signifies a potential advancement in the detection of CRC among IBD patients. This advancement could pave the way for a novel screening method for high-risk individuals. Moreover, the probe's performance notably surpassed that of [^{18}F]F-FDG (TBR $= 1.54 \pm 0.08$), which lacks the ability to effectively discriminate between cancerous and inflamed tissues.

Chakravarty et al.[21] have developed a ^{64}Cu radiolabeled Fab fragment of cetuximab, which was then separated from the Fc fragments using protein-A affinity chromatography to enhance its pharmacokinetics and therapeutic efficacy for cancer treatment. This purification significantly improved the binding specificity

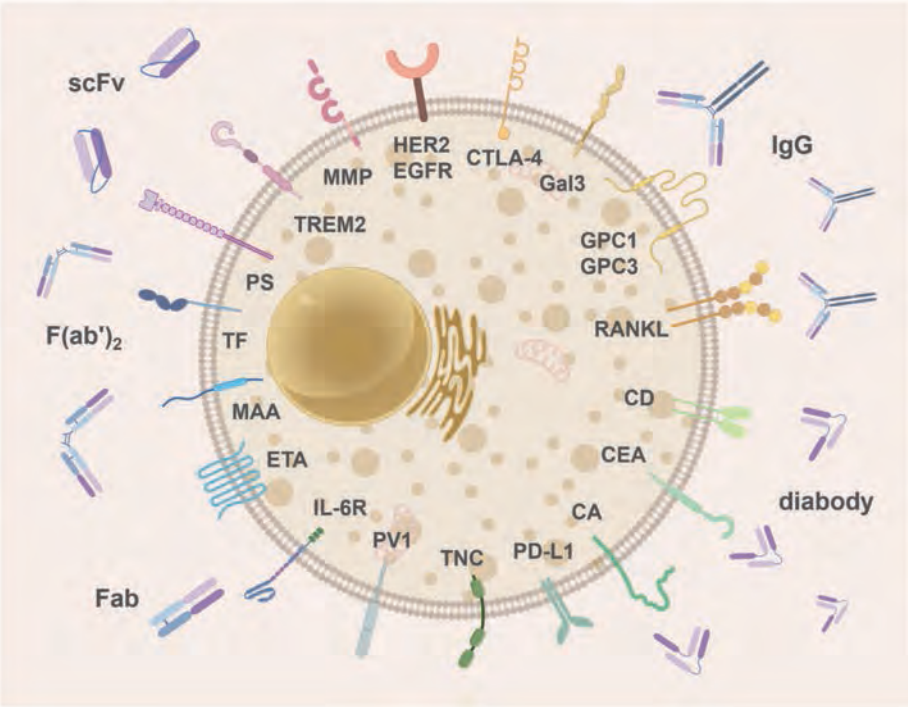

Figure 4 Antibodies and antibody fragments are engineered to specifically recognize and bind to target antigens, enabling precise molecular imaging. CD, cluster of differentiation; CTLA-4, cytotoxic T-lymphocyte-associated protein 4; CEA, carcinoembryonic antigen; CA, carbonic anhydrase; EGFR, epidermal growth factor receptor; ETA, endothelin A receptor; Her2, human epidermal growth factor receptor 2; GPC, glypican; Gal3, galectin 3; IL-6R, interleukin-6R; MAA, malondialdehyde-acetaldehyde; MMPs, matrix metalloproteinases; PDL1, programmed death-ligand 1; PS, phosphatidylserine; PV1, plasmalemma vesicle associated protein-1; RANKL, the receptor activator of nuclear factor kappa B ligand; TF, transferrin; TREM2, triggering receptor expressed on myeloid cells 2; TNC, tenascin-C.

and therapeutic efficacy of the radiolabeled Fab fragments, resulting in faster blood clearance and higher tumor retention compared to the unpurified fragments. The use of protein-A chromatography is essential for optimizing the pharmacokinetics and biodistribution of these fragments. Furthermore, Chakravarty et al.[20] employed CHX-A″-DTPA for efficient and stable radiolabeling of cetuximab Fab fragments with ^{44}Sc at room temperature. The maximum tumor uptake of [^{44}Sc]Sc-CHX-A″-DTPA-cetuximab-Fab was observed at 12.7 ± 0.7% ID/g at 4 h p.i. This study introduces ^{44}Sc as a promising new radioisotope for immunoPET, with a half-life that aligns well with the biological half-life of Fab fragments, potentially enhancing the clinical utility of this imaging modality.

Head and neck squamous cell carcinoma (HNSCC) typically requires treatments such as surgery followed by radiation or chemoradiotherapy (CRT), which often result in severe side effects and may not be sufficiently effective in advanced stages of the disease. To address the limitations of full antibody tracers, such as prolonged circulation times and high non-specific uptake, Lu et al.[22] and Boyle et al.[27] have utilized F(ab′)$_2$ fragments of panitumumab, which offer a more targeted approach. Ku et al.[23] further advanced this field by evaluating a PET theranostic strategy employing [^{64}Cu]Cu-DOTA-panitumumab F(ab′)$_2$ for specific EGFR imaging and assessing the dosimetry of radioimmunotherapy with [^{177}Lu]Lu-DOTA-panitumumab F(ab′)$_2$. Their research supports the feasibility of using PET theranostics to tailor and enhance treatment strategies for patients with HNSCC, suggesting a promising direction for clinical application (Fig. 5)[23]. Future research should focus on conducting human trials to validate the safety and effectiveness of this theranostic approach. These trials are essential for fine-tuning dose calculations and imaging protocols to improve precision, particularly concerning liver and whole-body imaging, thereby optimizing treatment protocols for HNSCC.

Lu et al.[24] focus on the development of EGFR-targeted metal chelating polymers (MCPs) for enhanced immunoPET imaging of pancreatic cancer. These MCPs were synthesized with varying numbers of pendant PEG_{2K} chains, conjugated to panitumumab F(ab′)$_2$ fragments, and labeled with ^{64}Cu. The MCPs with 2, 4, and 8 PEG_{2K} chains displayed distinct biodistribution profiles, with those containing more PEG chains showing reduced nonspecific uptake in the liver and kidneys. This design aims to improve tumor targeting and imaging contrast while minimizing off-target effects. However, the synthesis and conjugation process for MCPs with multiple PEG chains is complex and may require further optimization for large-scale production. Additionally, previous *in vitro* studies have shown that trastuzumab treatment can increase EGFR homodimerization and subsequent downregulation in tumors that express both EGFR and HER2. Building on this, Ma et al.[103] explore the utility of NIRF and PET imaging using panitumumab F(ab′)$_2$ fragments in patients undergoing trastuzumab therapy. This approach aims to provide complementary information on EGFR expression and its downregulation, offering a more nuanced understanding of the tumor's biological response to treatment.

Bellaye et al.[26] developed F(ab′)$_2$ fragments of cetuximab, which were conjugated with chelating agent DOTAGA. These fragments were subsequently radiolabeled with ^{111}In for diagnostic imaging and ^{177}Lu for therapeutic purposes. The [^{111}In]In-DOTAGA-F(ab′)$_2$-cetuximab demonstrated peak tumor uptake at 24 h p.i., exhibiting high tumor specificity, as evidenced by a

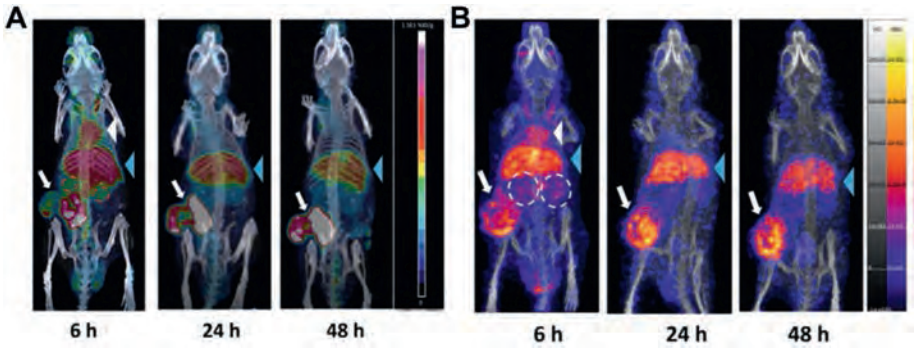

Figure 5 ImmunoPET/SPECT imaging of EGFR expression. (A) ImmunoPET images depicting an NRG mouse with a subcutaneously implanted head and neck squamous cell carcinoma (HNSCC) patient-derived xenograft (PDX) at 6, 24, and 48 h p.i. of [^{64}Cu]Cu-DOTA-panitumumab F(ab′)$_2$. The tumors were clearly visible at all assessed time points. (B) ImmunoSPECT images of the same NRG mouse model imaged of [^{177}Lu]Lu-DOTA-panitumumab F(ab′)$_2$. Tumors are indicated by the white arrows in the images. Reprinted with the permission from Ref. 23. Copyright © 2021 Springer.

marked reduction in tumor uptake following the administration of an excess of unlabeled DOTAGA-F(ab′)$_2$-cetuximab. Furthermore, radioimmunotherapy using [^{177}Lu]Lu-DOTAGA-F(ab′)$_2$-cetuximab resulted in significant tumor growth reduction at both 4 and 8 MBq doses. This dual approach highlights significant advancements in both targeted imaging and treatment of EGFR-expressing tumors, offering promising therapeutic strategies for effective cancer management.

Gastric and colon cancers rank among the deadliest malignancies affecting the digestive system. Shi et al.[25] developed a [^{99m}Tc]Tc-labeled cetuximab F(ab′)$_2$ fragment (Cet-F(ab′)$_2$) and assessed its efficacy both *in vitro* and *in vivo*. This imaging agent exhibited rapid uptake and sustained high contrast in EGFR-positive tumors, showcasing its potential for clinical application. Furthermore, Boyle et al.[104] investigated the use of [^{64}Cu]Cu-NOTA-panitumumab F(ab′)$_2$ in PET imaging and its extension to radioimmunotherapy (RIT) for pancreatic cancer. This approach utilized the therapeutic potential of β-particles and Auger electrons emitted by ^{64}Cu. Although RIT with [^{64}Cu]Cu-NOTA-panitumumab F(ab′)$_2$ alone did not significantly impact tumor growth or survival, its combination with gemcitabine (GEM) and rucaparib markedly improved median survival and delayed tumor progression. However, the tumors eventually continued to grow exponentially. The study concluded that ^{64}Cu may be suboptimal for RIT of pancreatic cancer due to low tumor absorbed doses, suggesting that radionuclides like ^{177}Lu might offer more effective results.

5.1.2. Human epidermal growth factor receptor 2

Human epidermal growth factor receptor 2 (HER2) is a transmembrane receptor that is notably overexpressed in various cancers. The overexpression of HER2 is associated with more aggressive tumor behavior, increased resistance to chemotherapy, and a generally poorer prognosis. The clinical approval of HER2-targeted antibody therapeutics, such as trastuzumab, trastuzumab emtansine (T-DM1), and pertuzumab, has not only enhanced treatment options but also bolstered its relevance as a target for molecular imaging. As these therapies gain traction, the utilization of HER2 as a molecular imaging target is expanding, offering new avenues for diagnosing and monitoring the progression of cancers characterized by HER2 overexpression.

Suman et al.[28] developed Fab and F(ab′)$_2$ fragments of trastuzumab through enzymatic digestion and utilized NOTA for efficient and stable ^{68}Ga labeling at ambient temperatures, enhancing their suitability for clinical applications. The resulting [^{68}Ga]Ga-NOTA-Fab-trastuzumab and [^{68}Ga]Ga-NOTA-F(ab′)$_2$-trastuzumab demonstrated high radiolabeling yields (>99%) and radiochemical purity (>98%), without the need for further purification—a key advantage for clinical translation. Rathore et al.[29] further explored this area by developing and evaluating [^{68}Ga]Ga-labeled trastuzumab Fab fragments for PET imaging in patients with HER2/neu-expressing breast cancer, focusing on assessing biodistribution and imaging efficacy. The ^{68}Ga trastuzumab Fab showed specific uptake in HER2/neu-positive breast cancer lesions and lymph nodes, with SUV_{max} values ranging from 3 to 5.8. Notably, high physiological uptake was observed in the liver, kidneys, and blood pool. However, the small sample size of the study limits the generalizability of these findings, highlighting the need for larger clinical trials to validate the results and confirm the potential of this imaging approach in routine clinical practice.

Lam et al.[30] developed [^{64}Cu]Cu-NOTA-pertuzumab F(ab′)$_2$ for PET imaging to monitor changes in HER2 expression in response to trastuzumab treatment. Building on this concept, Kwon et al.[31] refined the application of trastuzumab Fab by creating a bispecific radioimmunoconjugate, [^{64}Cu]Cu-NOTA-Fab-PEG$_{24}$-EGF, which targets both HER2 and EGFR. This dual targeting strategy aims to improve both imaging accuracy and potential therapeutic effectiveness. The use of a PEG$_{24}$ spacer to connect the trastuzumab Fab with EGF has successfully prolonged the conjugate's blood residence time, thereby enhancing its pharmacokinetics and tumor targeting efficiency. Biodistribution studies conducted 48 h post-injection (p.i.) in NOD/SCID mice bearing MDA-MB-231/H2N tumors showed a significantly higher tumor uptake of [^{64}Cu]Cu-NOTA-Fab-PEG$_{24}$-EGF (4.9 $\pm$ 0.4%ID/g) compared to [^{64}Cu]Cu-NOTA-Fab (1.9 $\pm$ 0.3%ID/g) and [^{64}Cu]Cu-NOTA-EGF (0.7 $\pm$ 0.2%ID/g), with statistical significance ($P < 0.0001$). These findings demonstrate the feasibility of using PET imaging with the newly developed bispecific radioimmunoconjugate, offering promising insights into its application for both diagnostic and therapeutic purposes in cancer management.

Compared to conventional Fabs, which often experience premature kidney clearance, a moderately prolonged plasma half-life can enhance tumor uptake and the tumor-to-blood ratio. PASylation, a technique that extends the *in vivo* lifetime of a recombinant protein by increasing its hydrodynamic molecular volume and

thereby reducing renal filtration, addresses this issue[105]. Mendler et al.[11] developed and evaluated [^{89}Zr]Zr and [^{124}I]I-labeled PASylated αHER2 Fab tracers for their effectiveness in imaging HER2-positive tumors *in vivo*. This method significantly improved the pharmacokinetics and imaging contrast by extending the plasma half-life of the Fab (Fig. 6)[11]. PET imaging revealed high tumor-to-blood and tumor-to-muscle ratios for both tracers. However, the [^{89}Zr]Zr-labeled Fab demonstrated superior *in vivo* stability and higher tumor uptake, establishing it as the preferred tracer for clinical translation. Mendler et al.[106] also explored PASylated Fab creation by attaching PAS sequences of varying lengths to the Fabs, finding that PASylation markedly enhanced tumor imaging by increasing tumor uptake and tumor-to-blood ratios. Fab-PAS$_{100}$ and Fab-PAS$_{200}$ emerged as the most promising formats, providing excellent imaging contrast and specific tumor targeting. Building on these advancements, Richter et al.[32] conducted the first clinical application of a PASylated Fab fragment for PET imaging in a human patient. The SUV$_{max}$ recorded values were 5.4 for the axillary lymph node and 4.2 for a presumed primary tumor in the breast. However, no significant activity was noted in the brain metastases. While these findings are promising, they are based on a single patient, which limits the generalizability of the results. Further studies involving a larger cohort are necessary to validate these findings and fully assess the potential of PASylated Fab fragments in clinical settings. The blood−brain barrier (BBB) is a significant obstacle in treating brain metastases because of its selective permeability. Full-sized antibodies often struggle to penetrate the BBB. In contrast, smaller antibody fragments have demonstrated superior penetration across the BBB. Their smaller size allows for better diffusion into brain tissue, increasing the likelihood of reaching brain metastases.

Facca et al.[33] developed a novel approach for immunoSPECT imaging of HER2-positive tumors by creating a radiolabeled pertuzumab Fab fragment conjugated with hexahistidine (His$_6$) peptides. This innovative conjugation allowed for efficient and stable radiolabeling with [^{99m}Tc(CO)$_3$(H$_2$O)$_3$]+. Their study demonstrated that [^{99m}Tc]Tc-His$_6$-pertuzumab Fab specifically visualized HER2-positive tumors at 24 h p.i., highlighting its potential as a diagnostic tool. Notably, tumors with intermediate HER2 expression, MDA-MB-361, showed significantly higher uptake (5.6 ± 1.4%ID/g) compared to those with low HER2 expression, MDA-MB-231 (0.8 ± 0.1%ID/g), underscoring the fragment's ability to discriminate based on the level of HER2 expression. This targeted imaging approach can enhance the accuracy of tumor characterization and aid in the tailored treatment of breast cancer.

5.2. *Clusters of differentiation*

Clusters of differentiation (CD) antigens have been extensively studied as potential diagnostic and therapeutic targets across a wide range of diseases. These surface molecules are crucial for the characterization and classification of cellular components within the immune system and have significantly advanced our understanding and treatment of various medical conditions. In this review, we will provide a detailed examination of several markers: CD20, CD38, CD44v6, CD103, and CD105.

5.2.1. *CD20*

CD20 is primarily expressed on B cells and has been effectively targeted in the treatment of B-cell malignancies such as non-Hodgkin lymphoma (NHL) and chronic lymphocytic leukemia (CLL). The advent of anti-CD20 monoclonal antibodies, including rituximab, ofatumumab, and obinutuzumab, has significantly enhanced the management of these diseases[107]. While standard diagnostic imaging for NHL often involves [^{18}F]-FDG PET/CT,

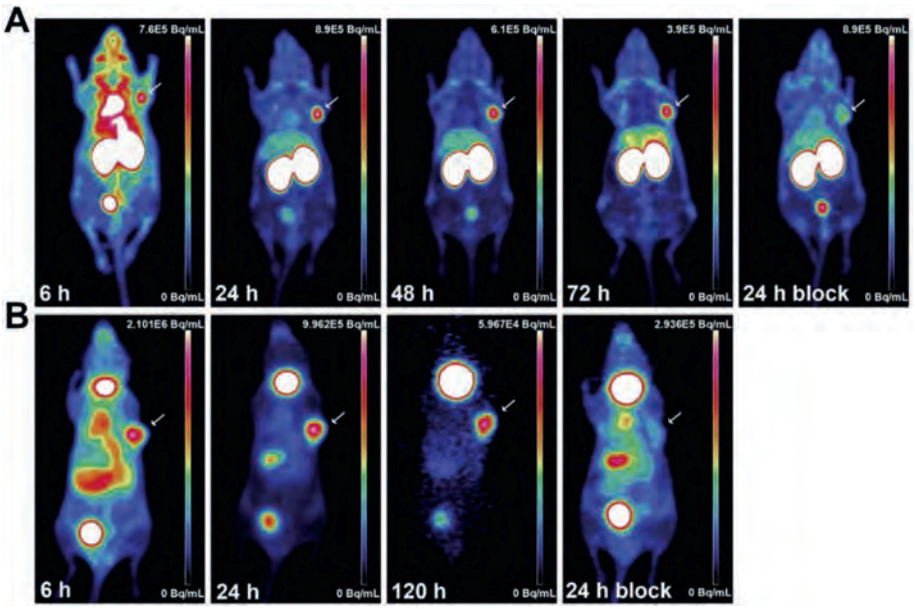

Figure 6 ImmunoPET imaging of HER2 expression. (A) [^{89}Zr]Zr-labeled αHER2 Fab and (B) [^{124}I]I-labeled αHER2 Fab were evaluated for their effectiveness in *in vivo* PET imaging using mice models with subcutaneous HER2-positive human tumor xenografts. The specificity of each tracer was verified through blocking experiments using an excess of unlabeled trastuzumab. For both PASylated αHER2 Fab tracers, optimal imaging contrast was achieved as early as 24 h p.i., demonstrating high tumor-to-normal tissue contrast and maintaining stable tumor uptake for several days. Reprinted with the permission from Ref. 11. Copyright © 2015 SNMMI.

this method can struggle with detecting indolent lymphomas and distinguishing between residual tumors and inflammation.

Addressing these challenges, Suman et al.[15] developed [^{68}Ga]Ga-labeled rituximab fragments [Fab and F(ab′)$_2$] as PET imaging agents, capitalizing on the smaller antibody fragments for enhanced imaging resolution and specificity. However, as the study was conducted *in vitro* and in normal mice, further validation of NHL animal models and clinical trials is necessary to confirm their efficacy and applicability in clinical settings. Expanding on this approach, Kang et al.[34] generated F(ab′)$_2$ fragments of obinutuzumab using the IdeS enzyme, which were then purified for PET imaging of CD20 in lymphoma xenograft models. The [^{64}Cu]Cu-NOTA-F(ab′)$_2$-obinutuzumab demonstrated peak uptake in Ramos tumors of 9.08 ± 1.67%ID/g at 12 h p.i., significantly surpassing uptake in CCL-155 tumors and the [^{64}Cu]Cu-NOTA-F(ab′)$_2$-IgG control (Fig. 7)[34]. These findings indicate that [^{64}Cu]Cu-NOTA-F(ab′)$_2$-obinutuzumab is a potential imaging agent for the noninvasive evaluation of CD20 expression in lymphoma.

The next step in this research trajectory involves evaluating the safety, efficacy, and diagnostic utility of [^{64}Cu]Cu-NOTA-F(ab′)$_2$-obinutuzumab in patients with CD20-positive lymphomas, aiming to refine its application as a reliable diagnostic tool in clinical oncology.

5.2.2. CD38

CD38, a multifunctional enzyme, is predominantly expressed on multiple myeloma cells and, to a lesser extent, is expressed on normal lymphoid and myeloid cells[108]. This enzyme has become a pivotal target in the treatment of multiple myeloma, as demonstrated by the use of therapeutic antibodies like daratumumab and isatuximab. These agents are instrumental not only in directly inducing cytotoxicity in tumor cells, but also in modulating the immune microenvironment to bolster anti-tumor activity. This mechanism of action highlights the significant therapeutic potential of targeting CD38 in enhancing treatment efficacy against multiple myeloma.

Kang et al.[35] utilized an enzymatic digestion method to prepare F(ab′)$_2$ fragments from daratumumab, which enhanced the efficiency and speed of imaging CD38-positive tumors. The specific binding affinity of the F(ab′)$_2$ fragments to CD38 was validated through surface plasmon resonance (SPR), flow cytometry, and confocal microscopy. The [^{64}Cu]Cu-NOTA-Dara-F(ab′)$_2$ fragment demonstrated rapid and substantial tumor uptake, with peak levels reaching 9.5 ± 0.7%ID/g at 12 h p.i (Fig. 8)[3.5]. This fragment offered significantly improved tumor-to-blood and tumor-to-muscle ratios compared to the full-length [^{64}Cu]Cu-NOTA-Dara antibody, yielding superior imaging contrast and enhanced tumor visualization. However, the [^{64}Cu]Cu-NOTA-Dara-F(ab′)$_2$ fragment exhibited high renal uptake due to its smaller size, potentially restricting its use for imaging tumors located near the kidneys. Future research directions could involve developing strategies to minimize renal uptake.

5.2.3. CD44v6

CD44 is a transmembrane glycoprotein, and the CD44 gene undergoes alternative splicing to produce various isoforms from its pre-messenger RNA (mRNA)[109]. This mRNA consists of ten standard exons, with the sixth variant exon encoding CD44v6, an isoform involved in critical biological processes such as cell growth, apoptosis, migration, and angiogenesis. CD44v6 is notably overexpressed in over 90% of head and neck squamous cell carcinomas (HNSCC), and it is prevalent in other cancers including lung, esophageal, and breast cancers.

Haylock et al.[36] developed and characterized the first fully human Fab fragment targeting CD44v6 specifically designed for molecular imaging. They conducted a comprehensive evaluation of the *in vivo* properties of these Fab fragments labeled with two different radionuclides, ^{111}In and ^{125}I. Their findings concluded that the [^{111}In]In-labeled Fab exhibited superior tumor targeting and imaging characteristics compared to the [^{125}I]-labeled Fab. The [^{111}In]In-labeled Fab demonstrated higher tumor uptake, slower dissociation from the tumor, and better tumor-to-blood ratios, making it a promising candidate for further clinical imaging studies aimed at detecting CD44v6-expressing tumors. ^{111}In, when bound to Fab fragments *via* chelators such as DTPA or CHX-A″-DTPA, tends to form more stable complexes. This reduces the likelihood of isotope dissociation, resulting in higher tumor uptake and clearer imaging. In contrast, ^{125}I is typically attached through direct iodination of tyrosine residues, which can lead to deiodination over time, particularly in tissues like the thyroid, leading to off-target uptake and reduced imaging specificity.

Continuing this research, one year later, Haylock et al.[37] evaluated the *in vitro* and *in vivo* binding properties of the radioiodinated human bivalent antibody fragment AbD19384, which targets CD44v6. This probe exhibited favorable biodistribution with pronounced clearance from non-target tissues over time and high tumor-to-blood ratios, particularly at 48 h p.i. It demonstrated high affinity and specificity for CD44v6, favorable biodistribution, and superior imaging properties compared to traditional [^{18}F]-FDG PET imaging, highlighting its potential as an effective targeting agent for molecular imaging of CD44v6-expressing tumors (Fig. 9)[37].

5.2.4. CD103

CD103, also known as αE integrin, is primarily expressed on intraepithelial lymphocytes and some regulatory T-cell subsets. It plays a crucial role in mediating adhesion to E-cadherin, facilitating the retention of lymphocytes within epithelial and tumor environments. This attribute identifies CD103 as a potential marker for tumor-infiltrating lymphocytes, which often signify an active immune response in the tumor microenvironment. Consequently, CD103 is being explored as a biomarker for monitoring therapeutic responses[110].

Fan et al.[38] advanced this research by generating Fab fragments from anti-CD103 antibodies and conjugating them with radiometals (^{89}Zr and ^{68}Ga) using TFP-N-Suc-Desferal-Fe. The resulting [^{89}Zr]Zr- and [^{68}Ga]Ga-labeled Fab fragments achieved high radiochemical purity (>95%). The study highlighted that [^{89}Zr]Zr-hCD103.Fab01A serves as a promising tracer for noninvasive PET imaging of CD103$^+$ T-cell infiltration, exhibiting high tumor uptake and low background signal at 24 h p.i. While the [^{68}Ga]Ga-hCD103.Fab01A tracer also demonstrated potential, its effectiveness was limited by the shorter half-life of ^{68}Ga, resulting in a more constrained effective imaging timeframe (Fig. 10)[38].

5.2.5. CD105

Tumor vasculature targeting presents a promising strategy for cancer imaging due to the critical role of angiogenesis in tumor development. CD105, a component of the TGF-beta receptor complex, is predominantly expressed on vascular endothelial cells and plays a pivotal role in angiogenesis. It is highly expressed in

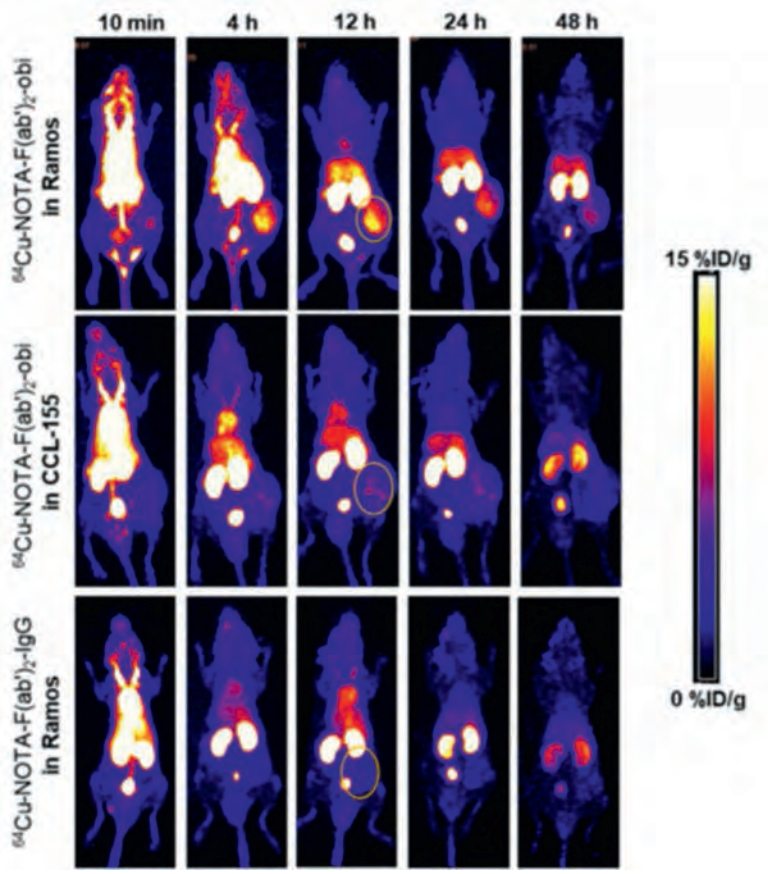

Figure 7 ImmunoPET imaging of CD20 expression. The imaging agent [^{64}Cu]Cu-NOTA-F(ab′)$_2$-obi demonstrated a clear visualization of the Ramos tumor as early as 4 h p.i., indicating its high specificity and effectiveness in targeting. In contrast, the [^{64}Cu]Cu-NOTA-F(ab′)$_2$-IgG, a control imaging agent, barely delineated the tumor, showcasing significantly lower specificity and effectiveness. Additionally, the CCL-155 tumor could not be visualized at any time post-injection of [^{64}Cu]Cu-NOTA-F(ab′)$_2$-obi. In the images, circles were used to indicate the locations of the tumors. Reprinted with the permission from Ref. 34. Copyright © 2020 SNMMI.

the proliferating blood vessels of solid tumors, making it a prime target for anti-angiogenic therapies. Agents targeting CD105, such as the monoclonal antibody TRC105, are under investigation in clinical trials to assess their efficacy in inhibiting tumor growth by impeding angiogenesis[111]. Additionally, CD105 is significantly implicated in the pathology of abdominal aortic aneurysm (AAA), a serious vascular condition characterized by the dilation and weakening of the abdominal aorta. Angiogenesis is a prominent pathological feature of AAA, with CD105 extensively expressed on the newly formed vessels within the aneurysm.

Shi et al.[40] leveraged this targeting potential by using the TRC105 antibody, which was enzymatically digested with papain to produce Fab fragments. These fragments were then conjugated to NOTA and radiolabeled with ^{64}Cu for imaging purposes. PET imaging conducted on mice with experimentally induced AAA revealed that the uptake of [^{64}Cu]Cu-NOTA-TRC105-Fab was significantly higher in regions affected by AAA compared to normal aortic tissues and blocking groups. This study demonstrated the feasibility of using [^{64}Cu]Cu-NOTA-TRC105-Fab PET imaging as a noninvasive method to monitor the biological activity associated with AAA. Such imaging could potentially assist in the early diagnosis and inform treatment decisions for this potentially fatal condition, illustrating the broad applicability of CD105-targeted imaging in both oncological and vascular diseases.

Chen et al.[39] have developed dual-labeled mesoporous silica nanoparticles (MSNs) conjugated with TRC105(Fab) specifically targeting CD105 in tumor vasculature. Through PET and NIRF imaging of 4T1 tumor-bearing mice (CD105-positive), it was observed that [^{64}Cu]Cu-MSN-800CW-TRC105(Fab) achieved significantly higher tumor uptake (5.4 ± 0.2%ID/g at 4 h p.i.) compared to non-targeted MSNs (2%ID/g) and the blocking groups (2.3 ± 0.2%ID/g). This evidence establishes [^{64}Cu]Cu-MSN-800CW-TRC105(Fab) as an effective dual-modality imaging agent for visualizing CD105 in tumor vasculature. The dual-labeled nanoparticles showcased high specificity, enhanced tumor uptake, and excellent imaging contrast, underlining their potential for future cancer theranostics applications.

The research conducted by Cai's group[41] introduced a novel bispecific antibody fragment (Bs-F(ab′)$_2$), crafted through click chemistry to link anti-EGFR and anti-CD105 Fab fragments. This Bs-F(ab′)$_2$ demonstrated superior binding affinity to U87MG cells, which express both EGFR and CD105, surpassing that of monovalent Fab fragments (Fig. 11)[41]. The study's findings revealed that the bispecific antibody fragment, [^{64}Cu]Cu-NOTA-Bs-F(ab′)$_2$,

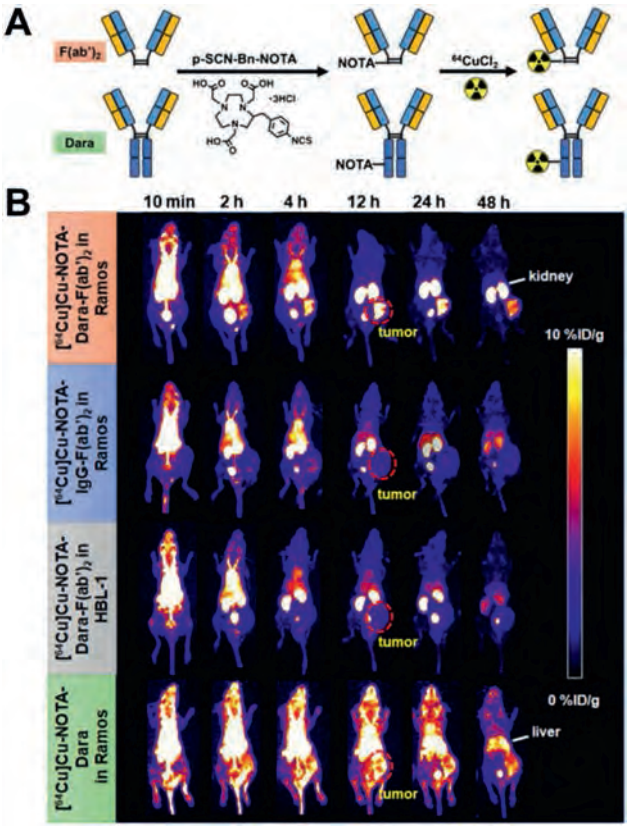

Figure 8 ImmunoPET imaging of CD38 expression. (A) Both F(ab′)$_2$ fragments and daratumumab (Dara) were conjugated with NOTA and subsequently radiolabeled with ^{64}Cu for imaging purposes. (B) The [^{64}Cu]Cu-NOTA-Dara-F(ab′)$_2$ demonstrated clear visualization of the Ramos tumor as early as 2 h p.i., with peak tumor uptake occurring at 12 h. In contrast, there was no noticeable tumor uptake in either the IgG-F(ab′)$_2$ or the HBL-1 control groups. Tumor regions in the images are outlined with red circles to highlight areas of interest. Reprinted with the permission from Ref. 35. Copyright © 2021 Springer.

significantly enhanced tumor targeting and imaging contrast in glioblastoma multiforme (GBM). The dual targeting mechanism of EGFR and CD105 leverages synergistic effects, leading to increased tumor uptake and more favorable tumor-to-background (T/B) ratios compared to monovalent fragments. By simultaneously targeting two different antigens, the bispecific approach can improve the specificity of tumor targeting, reduce off-target effects, and increase therapeutic efficacy. While the strategy is promising, there are challenges to consider. For instance, the production of bispecific fragments requires precise engineering to ensure proper folding and functionality of both Fab arms. Additionally, bispecific antibodies may have more complex pharmacokinetics due to their size and structure, potentially affecting their distribution and clearance.

5.3. *Immune system*

Cancer immunotherapy is rapidly establishing itself as the standard-of-care for a wide range of cancers[112]. Traditional methods such as IHC, polymerase chain reaction (PCR)-based assays, and serum or blood biomarkers are commonly employed to predict responses to immunotherapy treatments. However, accurately selecting suitable patients for immunotherapy and precisely evaluating treatment responses remain as significant challenges. Additionally, the incidence of immune-related adverse events associated with these therapies is on the rise. At present, effective surveillance strategies to detect these unexpected complications are lacking. There is growing evidence that suggests integrating Fab and F(ab′)$_2$ fragments with immunoPET imaging could improve the management of cancer patients by providing more precise monitoring of therapeutic effects and earlier detection of adverse reactions.

5.3.1. *Immune checkpoint-related molecules*

5.3.1.1. PDL1. The interaction between Programmed Death-Ligand 1 (PD-L1) and its receptor, PD-1, is crucial in facilitating tumor immune escape by suppressing T cell activation. This interaction contributes to the induction of immune tolerance and adaptive immune resistance, often leading to T cell exhaustion[113]. Within the tumor microenvironment, the PD-1/PD-L1 engagement plays a central role in enabling tumor cells to evade immune detection and thwarting the immune system's ability to launch an effective attack by cytotoxic T cells[114]. This mechanism is a significant barrier to effective immune responses against tumors and highlights the need for therapeutic strategies that can disrupt these interactions to enhance cancer immunotherapy efficacy.

Approximately 50%−60% of patients with non-small cell lung cancer (NSCLC) express PD-L1, making it a critical target for

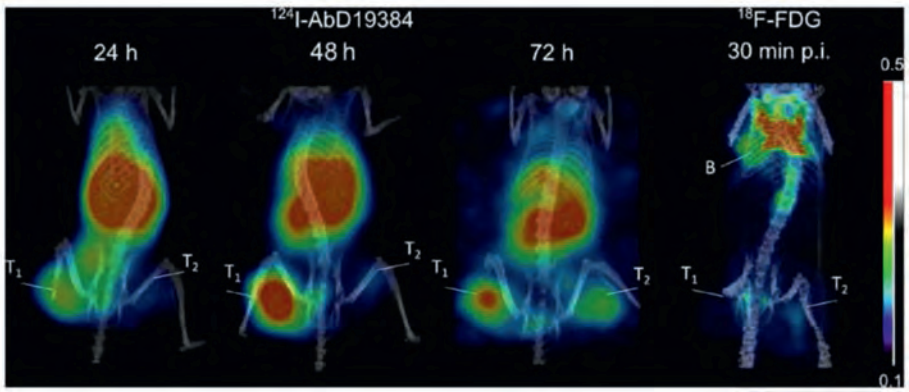

Figure 9 ImmunoPET imaging of CD44v6 expression. ImmunoPET imaging of [^{124}I]I-AbD19384 in mice bearing high CD44v6-expressing tumors on the left 'T1' and low CD44v6-expressing tumors on the right 'T2'. Uptake is also seen in kidneys, liver and spleen. [^{18}F]-FDG-PET is shown on the right at 30 min p.i., showing uptake in brown fat 'B'. Reprinted with the permission from Ref. 37. Copyright © 2016 Spandidos.

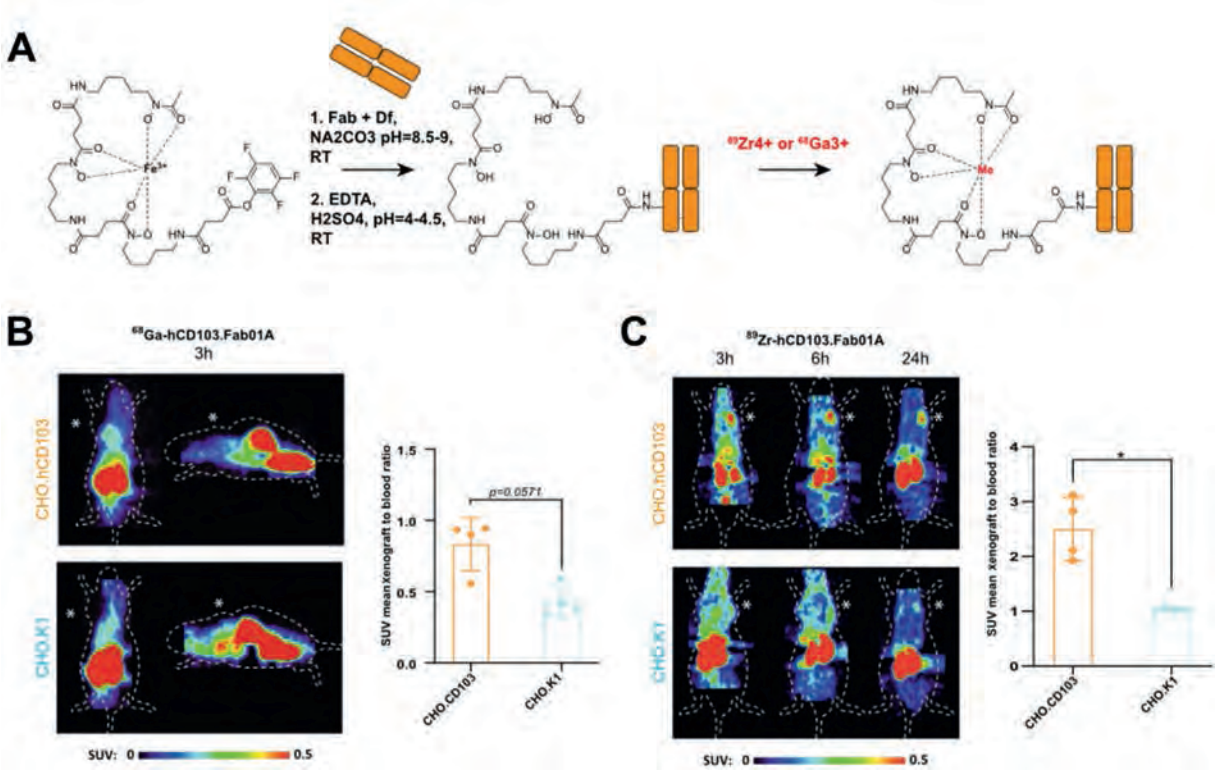

Figure 10 ImmunoPET imaging of CD103 expression. (A) Schematic representation of the TFP-N-Suc-desferal-Fe chelator conjugation with hCD103.Fab and subsequent radiolabeling with ^{89}Zr/^{68}Ga. (B) Representative coronal and sagittal [^{68}Ga]Ga-hCD103.Fab01A PET images in CHO.CD103 (top) and CHO.K1 (bottom) xenograft mice, recorded 3 h p.i. The xenograft area is indicated by an asterisk. The *in vivo* [^{68}Ga]Ga-hCD103.Fab01A xenograft-to-blood ratio at 3 h p.i. is expressed as SUV_{mean}. (C) Representative coronal [^{89}Zr]Zr-hCD103.Fab01A PET images in CHO.CD103 (top) and CHO.K1 (bottom) xenograft mice, recorded at 3, 6, and 24 h p.i. The xenograft area is indicated by an asterisk. The *in vivo* [^{89}Zr]Zr-hCD103.Fab01A xenograft-to-blood ratio at 24 h p.i. is expressed as SUV_{mean}. Reprinted with the permission from Ref. 38. Copyright © 2023 Springer.

immunotherapy using anti-PD-1/PD-L1 antibodies such as durvalumab. Cheng et al.[43] processed durvalumab into F(ab′)$_2$ fragments using IdeS protease, subsequently labeling them with ^{124}I. *In vivo* studies revealed that [^{124}I]I-Durva-F(ab′)$_2$ exhibited faster blood clearance and higher T/B ratios compared to full-length [^{124}I]I-Durva. Notably, peak tumor uptake of [^{124}I]I-Durva-F(ab′)$_2$ occurred at 12 h p.i.—considerably sooner than the 48 h observed for [^{124}I]I-Durva, suggesting its utility as an effective tool for noninvasive PD-L1 evaluation and as an aiding patient stratification for immunotherapy (Fig. 12)[43].

Despite these advantages, the initial specific activity and high blood accumulation of this probe were suboptimal. To address these issues, the structure of durvalumab was modified using *N*-succinimidyl-3-(4-hydroxyphenyl) propionate (SHPP), aimed to improve the accessibility of tyrosine residues on the protein surface. This modification led to [^{124}I]I-HPP-Durva-F(ab′)$_2$, which showed a significant increase in specific activity and enhanced *in vivo* clearance rates. These improvements not only reduced the effective dose required for subjects, but they also increased the T/B ratio, making [^{124}I]I-HPP-Durva-F(ab′)$_2$ a more effective and safer option for clinical imaging and evaluation of PD-L1 expression[44].

Bridgwater et al.[42] utilized pepsin digestion to create F(ab′)$_2$ fragments from a full anti-PD-L1 antibody. They successfully synthesized [^{89}Zr]Zr-Df-F(ab′)$_2$, achieving high radiochemical purity and stability. However, the study, conducted in mouse models, noted that the long half-life of ^{89}Zr could limit the dosage administered due to the associated risk of excessive radiation exposure to patients. Bouleau et al.[45] evaluated three radioligands derived from the anti-PD-L1 IgG1 C4 antibody: the full-length IgG C4, the fragment antigen-binding (Fab) C4, and a double mutant IgG C4 (H310A/H435Q) with reduced affinity for the murine neonatal Fc receptor (FcRn), all labeled with ^{89}Zr. The study concluded that both [^{89}Zr]Zr-Fab C4 and the [^{89}Zr]Zr-IgG C4 (H310A/H435Q) effectively and specifically detected PD-L1 expression in NSCLC models, providing earlier and higher contrast imaging compared to the full-length [^{89}Zr]Zr-IgG C4. These results endorse further clinical exploration of these optimized radioligands for noninvasive PD-L1 imaging.

Tran et al.[46] focused on enhancing the pharmacokinetics and imaging efficiency of anti-PD-L1 Fab fragments by comparing site-specific and random radiolabeling strategies. They assessed enzymatic site-specific radiofluorination using ^{18}F and random lysine radiolabeling with ^{89}Zr. The study found that site-specific radiofluorination through LplA-mediated conjugation yielded anti-PD-L1 Fab fragments with superior pharmacokinetics and higher specific activity compared to random radiolabeling techniques. The site-specific [^{18}F]-labeled Fab exhibited faster clearance and improved T/B ratios, positioning it as a promising candidate for immunoPET imaging of PD-L1 expression. This comprehensive

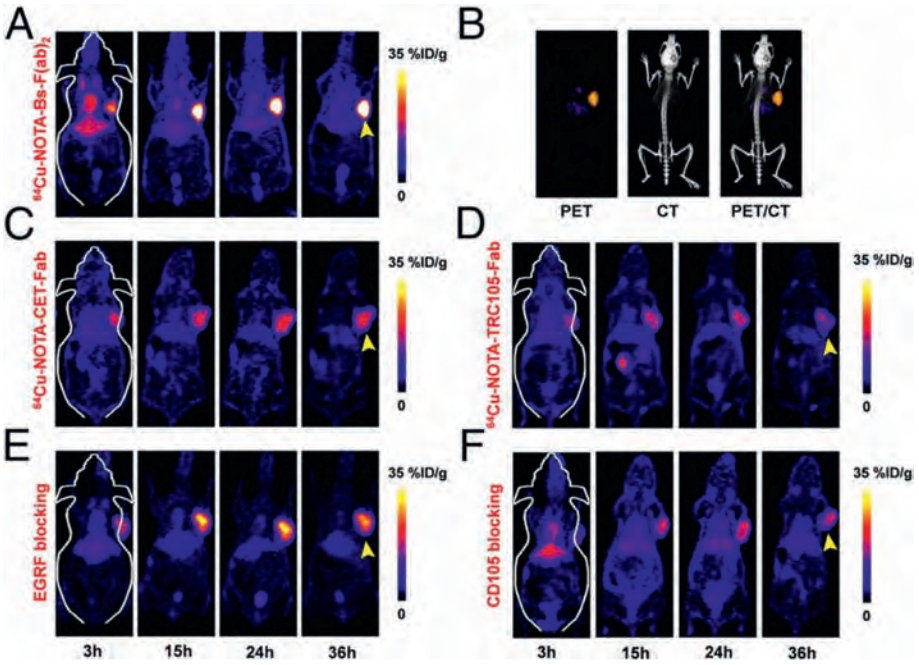

Figure 11 ImmunoPET imaging of CD105 expression. (A) [^{64}Cu]Cu-NOTA-Bs-F(ab′)$_2$ exhibited significantly higher tumor accumulation compared to the two monovalent fragments. (B) Coregistered PET/CT images of U87MG-bearing mice highlighted the pronounced tumor contrast and provided detailed anatomical information. (C, D) [^{64}Cu]Cu-NOTA-Bs-F(ab′)$_2$ showed early and substantial tumor uptake (32.1 ± 6.9%ID/g at 3 h p.i.), peaking at 47.5 ± 6.7%ID/g at 15 h p.i. The maximum tumor uptake of [^{64}Cu]Cu-NOTA-CET-Fab and [^{64}Cu]Cu-NOTA-TRC105-Fab was significantly lower ($P < 0.01$), with values of 14.4 ± 1.1%ID/g and 14.3 ± 6.6%ID/g, respectively. (E, F) The peak tumor uptake values of [^{64}Cu]Cu-NOTA-Bs-F(ab′)$_2$ decreased significantly to 13.7 ± 2.6%ID/g and 20.3 ± 2.4%ID/g following CD105 and EGFR blocking, respectively. Reprinted with the permission from Ref. 41. Copyright © 2015 National Academy of Sciences.

study underscores the advantages of site-specific radiolabeling strategies in optimizing the pharmacokinetics and imaging capabilities of antibody fragments.

5.3.1.2. CD276. CD276, also known as B7−H3, is a member of the B7 family of immune checkpoint molecules and serves as a biomarker expressed on both tumor vasculature and tumor cells. Unlike normal tissue angiogenesis where CD276 is not expressed, its presence on malignant cells and their vasculature makes it an ideal target for the tumor-specific delivery of anticancer therapeutics[115].

Bao et al.[47] engineered a novel therapeutic agent by conjugating the Fab fragment of an anti-CD276 antibody with the photosensitizer IRDye700, resulting in IRD-αCD276/Fab. This conjugate was evaluated for its efficacy in both subcutaneous and lung metastatic 4T1 tumor models. The study also employed PET imaging to dynamically monitor PD-L1 expression following photodynamic therapy (PDT). Notably, the combination of IRD-αCD276/Fab PDT with anti-PD-L1 therapy significantly enhanced tumor growth inhibition and reduced lung metastasis, demonstrating superior efficacy compared to either treatment alone. This synergistic effect underscores the potential of integrating targeted photodynamic therapy with immune checkpoint inhibition as a powerful strategy for cancer treatment (Fig. 13)[47].

5.3.1.3. CTLA-4. CTLA-4, a T-cell surface glycoprotein akin to CD28, interacts with B7-1 and B7-2 and is predominantly expressed on activated T cells. It serves as a crucial regulator in the inflammatory response[116]. To address the challenge of tracking CTLA-4$^+$ T cells during immunotherapy, Cai's lab[48] developed PET imaging tracers based on the therapeutic antibody ipilimumab and its F(ab′)$_2$ fragment. These tracers specifically accumulated in the salivary glands of humanized mice, indicating successful localization of CTLA-4$^+$ T cells (Fig. 14)[48]. Both [^{64}Cu]Cu-NOTA-ipilimumab and [^{64}Cu]Cu-NOTA-ipilimumab-F(ab′)$_2$ demonstrated efficacy in PET imaging of CTLA-4$^+$ T cells. The full antibody tracer showed higher absolute uptake in target tissues, suggesting robust targeting ability. In contrast, the F(ab′)$_2$ fragment provided higher imaging contrast due to its faster clearance from non-target tissues. These findings highlight the potential of these tracers for noninvasive monitoring of CTLA-4 expression, which can significantly enhance patient stratification and therapy monitoring in clinical settings.

5.3.2. Lineage-associated antigens

5.3.2.1. CD4. In the realm of T cell tracking, novel immunoPET techniques that target general T cell markers, such as CD4 and CD8, offer significant advantages over traditional methods like *ex vivo* direct labeling or reporter gene imaging. CD4 T cells with cytotoxic activity (CD4 CTL) are increasingly recognized for their role in various immune responses[117]. The molecular imaging of CD4$^+$ T cells is gaining importance, especially in the monitoring of inflammatory diseases such as rheumatoid arthritis (RA), IBD, and multiple sclerosis.

Clausen et al.[49] have developed a novel PET tracer, [^{64}Cu]Cu-NOTA-CD4-F(ab′)$_2$, specifically for imaging CD4$^+$ T cells in RA using a collagen-induced arthritis (CIA) mouse model. This advancement aims to improve early detection and treatment

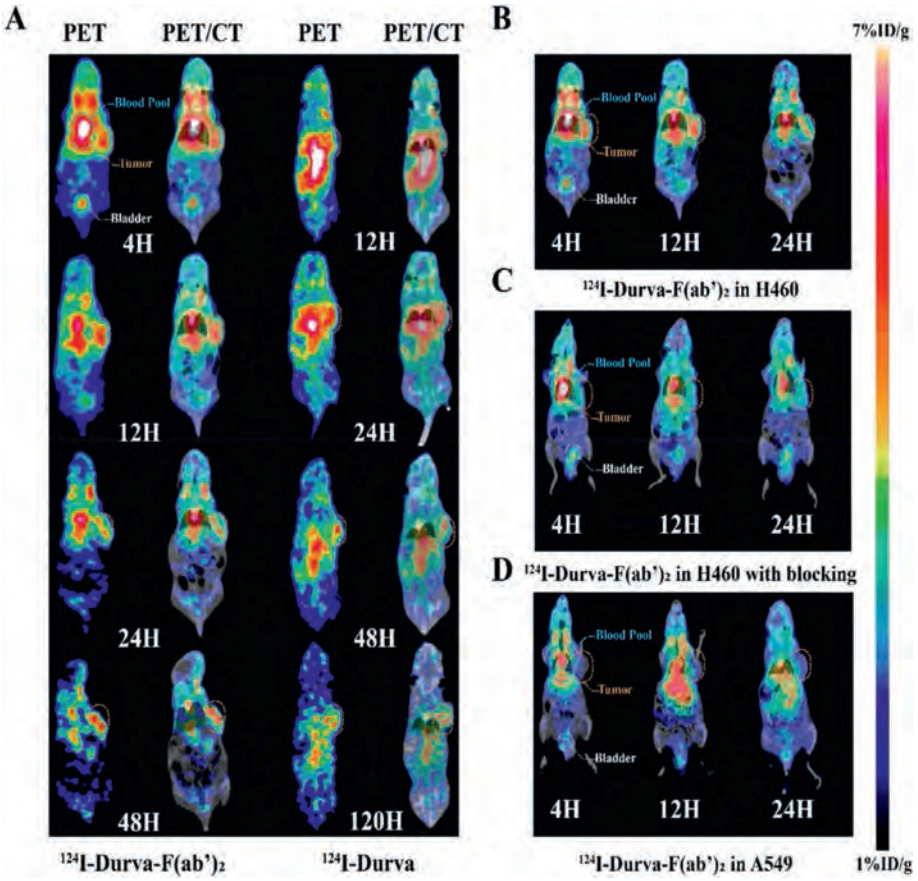

Figure 12 ImmunoPET imaging of PD-L1 expression. (A) [^{124}I]I-Durva-F(ab′)$_2$ and [^{124}I]I-Durva PET and PET/CT images. Compared to [^{124}I]I-Durva, mice injected with [^{124}I]I-Durva-F(ab′)$_2$ exhibited higher contrast and faster blood clearance. (B, D) [^{124}I]I-Durva-F(ab′)$_2$ PET/CT images were obtained from H460 and A549 tumor-bearing mice. The H460 tumor was visible as early as 4 h p.i. of [^{124}I]I-Durva-F(ab′)$_2$, whereas the A549 tumor was scarcely detectable. Furthermore, the visualization of the H460 tumor was blocked by the administration of an excess amount of unlabeled intact durvalumab. Reprinted with the permission from Ref. 43. Copyright © 2022 American Chemical Society.

monitoring. The tracer showed significant accumulation in T cell-rich tissues, notably in the spleen and thymus. PET imaging effectively differentiated between untreated and dexamethasone (DXM)-treated mice, illustrating its potential for evaluating therapeutic responses. However, the study also observed non-specific accumulation in severely inflamed tissues, which underscores the need for further refinement of the tracer to improve its specificity and utility in clinical settings. This finding highlights the ongoing challenge of balancing targeted imaging capabilities with minimizing non-specific uptake to optimize the effectiveness and accuracy of immunoPET tracers (Fig. 15)[49].

5.3.2.2. CD8. CD8$^+$ T cells are pivotal to the body's adaptive immune system, particularly in their role as cytotoxic lymphocytes that drive anti-tumor responses. Their activation and infiltration into tumors make them key markers for assessing the efficacy of immunotherapies. In this context, Kristensen et al.[50] developed a [^{64}Cu]Cu-labeled F(ab′)$_2$ fragment specifically designed for targeting and imaging CD8a$^+$ T cells. The tracer achieved a maximum tumor uptake of 6.39 ± 0.88% ID/g at 1 h p.i., with the uptake peaking at 9.25 ± 0.48% ID/g at 6 h. The study concluded that [^{64}Cu]Cu-NOTA-CD8a PET imaging effectively monitors CD8a$^+$ T cell responses, particularly to therapies combining radiation (XRT) and anti-CTLA-4 treatment. This imaging agent enables early detection of therapeutic responses and can differentiate between responders and non-responders before changes in tumor volume become apparent. This capability positions [^{64}Cu]Cu-NOTA-CD8a PET imaging as a promising prognostic tool in the field of immunotherapy, potentially enhancing treatment strategies and patient outcomes (Fig. 16)[50].

5.4. Carbonic anhydrase

5.4.1. Carbonic anhydrase VI

CA6 (Carbonic Anhydrase VI), also known as salivary carbonic anhydrase, is predominantly located in the salivary glands and secreted into saliva. SAR566658 (huDS6-DM4) is an antibody-drug conjugate comprising a humanized monoclonal antibody (huDS6) that targets the tumor-associated mucin 1-sialoglycotope, CA6[118], linked to the cytotoxic maytansinoid derivative DM4[119]. This immunoconjugate is designed to release DM4 upon the binding and internalization of the antibody and/or antigen, which then binds to microtubules, disrupting their dynamics and inducing mitotic arrest in CA6-expressing tumor cells.

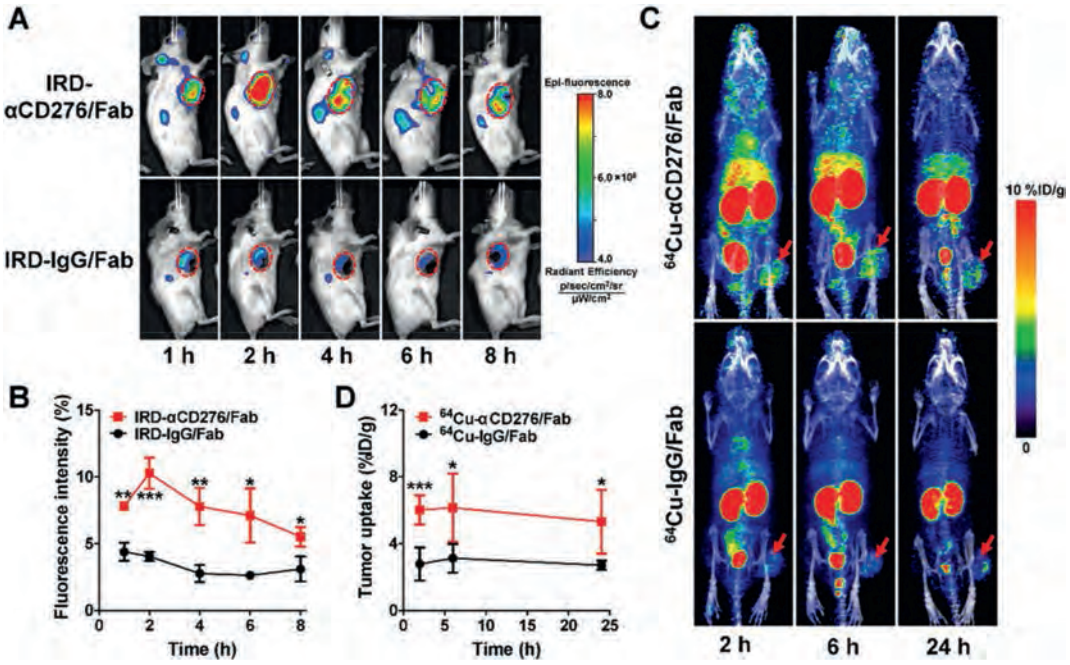

Figure 13 ImmunoPET imaging of CD276 expression. (A, B) *In vivo* optical imaging and quantification of tumor uptake in 4T1 tumor-bearing BALB/c mice at 1, 2, 4, 6, and 8 h p.i. of IRD-αCD276/Fab or IRD-IgG/Fab. (C, D) *In vivo* PET/CT imaging and quantification of tumor uptake in 4T1 tumor-bearing BALB/c mice at 2, 6, and 24 h p.i. of [^{64}Cu]Cu-NOTA-αCD276/Fab or [^{64}Cu]Cu-NOTA-IgG/Fab. Reprinted with the permission from Ref. 47. Copyright © 2019 American Chemical Society.

Building on this therapeutic approach, Ilovich et al.[51] have developed three [^{64}Cu]Cu-labeled antibody fragments derived from the CA6-targeting antibody huDS6. These fragments include B-Fab, Cross-over dual variable (CODV)-Fab, and Diabody. The B-Fab fragment demonstrated high stability (retaining over 95% stability after 24 h in human serum) and immunoreactivity (exceeding 70%). Notably, it enabled differentiation between CA6-positive and CA6-negative tumors as early as 6 h p.i., exhibiting a 1.7-fold higher uptake ratio in CA6-positive tumors. On the other hand, CODV-Fab and Diabody fragments showed their highest uptake values in the kidneys, followed by the liver and CA6-positive tumors. While these fragments displayed high specificity, there was observable non-specific uptake in both tumor models. The rapid clearance of these fragments from the bloodstream led to reduced tumor uptake. This study underscores the potential and challenges of using radiolabeled antibody fragments for targeted imaging and therapy, indicating the need for further optimization to enhance their therapeutic efficacy and reduce non-specific uptake.

5.4.2. *Carbonic anhydrase XII*

Carbonic anhydrase XII (CA-XII) is a cell surface glycoprotein that is overexpressed in glioma cells but not found in healthy brain parenchyma[120]. GBM, an aggressive brain tumor, typically has a poor prognosis. Standard treatment includes surgical resection followed by radiotherapy and chemotherapy. However, the absence of approved maintenance therapies after standard treatment often leads to tumor recurrence near the resection cavity. Intracavitary radioimmunotherapy (iRIT), which involves the direct administration of radiolabeled antibody fragments into the resection cavity, represents a novel method for targeted tumor control, specifically exploiting the overexpression of CA-XII in glioma cells.

Fiedler et al.[121] established a fully automated production routine for ^{64}Cu using the Alceo system, which yielded high-purity and high-activity ^{64}Cu suitable for radiolabeling. The [^{64}Cu]Cu-DOTA-6A10 Fab fragment showed effective targeting of CA XII-expressing tumors in small animal PET imaging, achieving a high tumor-to-muscle ratio. These results indicate that [^{64}Cu]Cu-6A10 Fab holds considerable promise for the diagnostic imaging of CA XII-positive tumors. Roll et al.[52] addressed the gap in effective maintenance therapies for glioblastoma by developing a targeted approach that delivers high doses of radiation directly to residual tumor cells in the resection cavity. This approach utilizes [^{177}Lu]Lu-labeled 6A10-Fab fragments that bind specifically to CA-XII, ensuring that the radiopharmaceutical concentrates in the tumor cells while sparing healthy brain tissue. A fractionated dosing schedule was designed to maximize therapeutic effects while minimizing side effects. The therapy demonstrated promising initial efficacy, with two out of three patients showing stable disease following treatment. However, this early-phase pilot study lacks long-term efficacy and safety data, highlighting the need for further research to validate this innovative therapeutic approach.

5.5. *Galectin-3*

Thyroid cancer (TC) encompasses a range of malignancies, from the relatively indolent papillary thyroid microcarcinoma to the highly aggressive anaplastic thyroid carcinoma (ATC). Although the incidence of thyroid cancer is on the rise, accurately differentiating malignant from benign thyroid nodules continues to present significant challenges. This difficulty is partly due to the

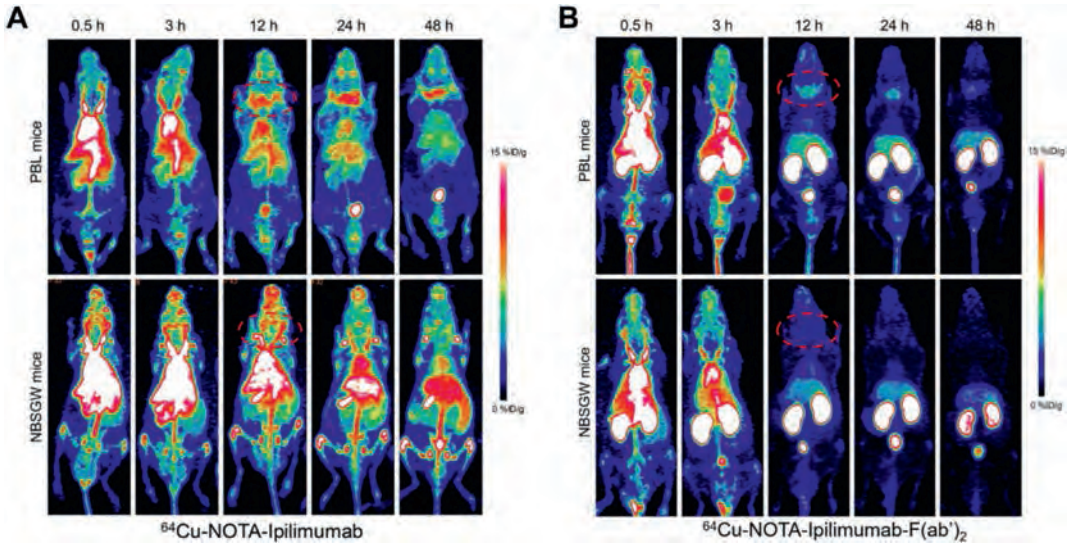

Figure 14 ImmunoPET imaging of CTLA-4 expression. (A) ImmunoPET imaging of [^{64}Cu]Cu-NOTA-ipilimumab in humanized (PBL) and control (NBSGW) mice. The salivary glands (sites of T-cell infiltration) are outlined with red dashed circles. The highest salivary gland uptake was observed at 24 h p.i. of [^{64}Cu]Cu-NOTA-ipilimumab, with a value of 7.00 $\pm$ 2.19%ID/g. (B) ImmunoPET imaging of [^{64}Cu]Cu-NOTA-ipilimumab-F(ab$'$)$_2$ in PBL and NBSGW mice. The salivary gland uptake of [^{64}Cu]Cu-NOTA-ipilimumab-F(ab$'$)$_2$ was highest immediately post-injection, with a measured uptake of 2.40 $\pm$ 0.86%ID/g at the 24 h scan. Reprinted with the permission from Ref. 48. Copyright © 2019 American Journal of Cancer Research.

limited effectiveness of thyroid scintigraphy, which often fails to clearly distinguish between malignant and benign conditions. Additionally, the diagnostic process is further complicated in some thyroid cancers that lose the ability to uptake radioiodine, typically due to decreased expression of the sodium-iodide symporter (NIS). This often results in unnecessary thyroidectomies when benign nodules are mistakenly assessed as malignant. Galectin-3 (Gal3), a β-galactoside-binding protein involved in various cellular processes including proliferation, adhesion, differentiation, angiogenesis, and apoptosis, emerges as a significant biomarker in this context. It is overexpressed in most thyroid cancers but not in normal thyroid cells, offering a promising avenue for more specific diagnostic imaging[122,123].

De Rose et al.[53] validated the targeting of Gal3 as an effective method for detecting non-radioiodine-avid thyroid cancers using PET and fluorescence imaging in orthotopic tumor models. The PET imaging provided specific and selective visualization of thyroid tumors through Gal3 targeting, with no detectable signal in the tumor-free thyroid lobe (Fig. 17)[53]. This method successfully identified thyroid cancers that did not absorb radioiodine, overcoming a major limitation of conventional thyroid cancer diagnostics. Peplau et al.[54] developed and validated a chimeric Fab directed against human Gal3, employing it as an immunoPET tracer for imaging thyroid cancer. To enhance the plasma half-life of the Fab fragments, PASylation was employed; specifically, αGal3-Fab-PAS$_{200}$ was conjugated with DFO and labeled with ^{89}Zr. PET imaging demonstrated highly selective and rapid accumulation in orthotopic thyroid tumors, with strong contrast evident 24 h p.i. Notably, there was no uptake in the tumor-free thyroid lobe. Future research directions should explore the application of this tracer in other Gal3-expressing cancers or inflammatory conditions to broaden its clinical utility. Two years later, Peplau et al.[55] further advanced this research by humanizing the chimeric Fab, enhancing its clinical applicability and reducing its immunogenicity. This modification is aimed at facilitating the transition of the tracer into clinical settings, potentially offering a more effective diagnostic option for patients with thyroid cancer and other Gal3-related diseases.

5.6. *Tissue factor*

Tissue factor (TF) is highly expressed in various cancers, including TNBC, and is associated with cancer progression, metastasis, and poor survival outcomes. Given its prevalent overexpression in TNBC, TF presents a viable target for both diagnostic and therapeutic interventions[124]. Shi et al.[56] focused on the production, characterization, and evaluation of a TF-targeting Fab fragment derived from the chimeric antibody ALT-836, which was radiolabeled with ^{64}Cu for PET imaging purposes. The resulting imaging agent, [^{64}Cu]Cu-NOTA-ALT-836-Fab, has demonstrated effectiveness in detecting TF expression in TNBC. It offers rapid blood clearance and high tumor uptake, yielding excellent T/B contrast (Fig. 18)[56]. The specificity of the Fab fragment for TF and its capacity for same-day imaging highlight its potential as a promising candidate for clinical adoption. This development could significantly enhance the diagnosis and management of TNBC, providing a more targeted approach that could lead to preferrable patient outcomes.

Luo et al.[57] developed and evaluated a bispecific heterodimer targeting both TF and CD105 for PET imaging of pancreatic cancer, aiming to overcome the limitations associated with single-target imaging agents. This innovative approach involved synthesizing the heterodimer through a bio-orthogonal "click" reaction that conjugated Fab fragments targeting TF and CD105, followed by labeling with ^{64}Cu for PET imaging. The PET imaging results with the [^{64}Cu]Cu-labeled heterodimer demonstrated

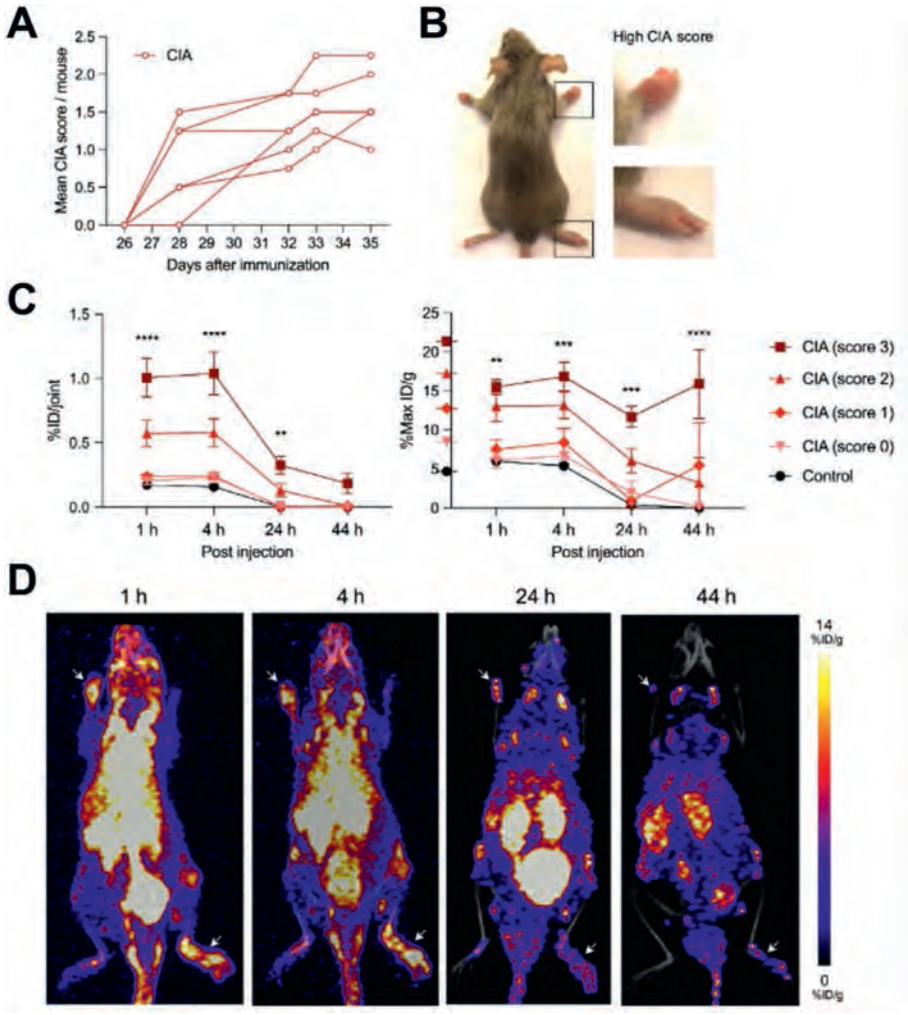

Figure 15 ImmunoPET imaging of $CD4^+$ T cells expression. (A) Collagen-induced arthritis (CIA) mice were scored based on the degree of inflammation. (B) Representative images of a CIA mouse on Day 35, showing pronounced arthritis in the right carpal and tarsal joints. (C) [^{64}Cu]Cu-NOTA-CD4 uptake per joint and maximum activity in the carpal and tarsal joints of CIA mice compared to control mice. (D) Representative maximum intensity projections of a CIA mouse with pronounced arthritis in the left carpal and right tarsal joints at 1, 4, 24, and 44 h p.i. of [^{64}Cu]Cu-NOTA-CD4. Reprinted with the permission from Ref. 49. Copyright © 2022 Springer.

significantly higher tumor uptake (28.8 ± 3.2%ID/g) at 30 h p.i., compared to the monospecific Fab tracers (12.5 ± 1.4 and 7.1 ± 2.6%ID/g). This dual-targeting strategy is anticipated to enhance tumor localization and uptake more effectively than single-target agents, providing a more accurate and efficient diagnostic tool. A year later, Luo integrated PET and NIRF imaging within a single agent, facilitating high-sensitivity, real-time imaging, and precise tumor delineation[58]. Although NIRF imaging exhibited weaker signals compared to PET that are likely due to tissue attenuation and dye degradation, this combination still holds significant potential for clinical applications.

5.7. Glypican

5.7.1. Glypican-1

Glypican-1 (GPC-1), a heparan sulfate proteoglycan, is notably overexpressed in various solid tumors, including GBM, making it a valuable biomarker for targeted immunotherapy and diagnostic imaging[125]. GBM represents the most aggressive type of primary brain cancer, constituting approximately 85% of all primary central nervous system tumors[126]. Despite advances in surgical techniques, radiation therapy, and chemotherapy, the prognosis for GBM patients remains dire.

In response to this challenge, Ghosh et al.[59] developed and evaluated [^{89}Zr]Zr-conjugated Miltuximab—a clinical-stage anti-GPC-1 mAb—and its fragments (Fab, F(ab′)$_2$, and scFv) for use as immunoPET tracers to detect GPC-1-positive GBM tumors. The study found that [^{89}Zr]Zr-DFO-Miltuximab exhibited significantly higher tumor uptake (5.7 ± 0.94% ID/g) compared to its F(ab′)$_2$ (2.9 ± 0.56% ID/g), Fab (1.4 ± 0.22% ID/g), and scFv (0.9 ± 0.15% ID/g) counterparts. These results suggest a superior utility of the Fc-containing whole mAb format over the smaller antibody fragments for targeting this specific biomarker. However, further refinement of antibody fragments is necessary to enhance

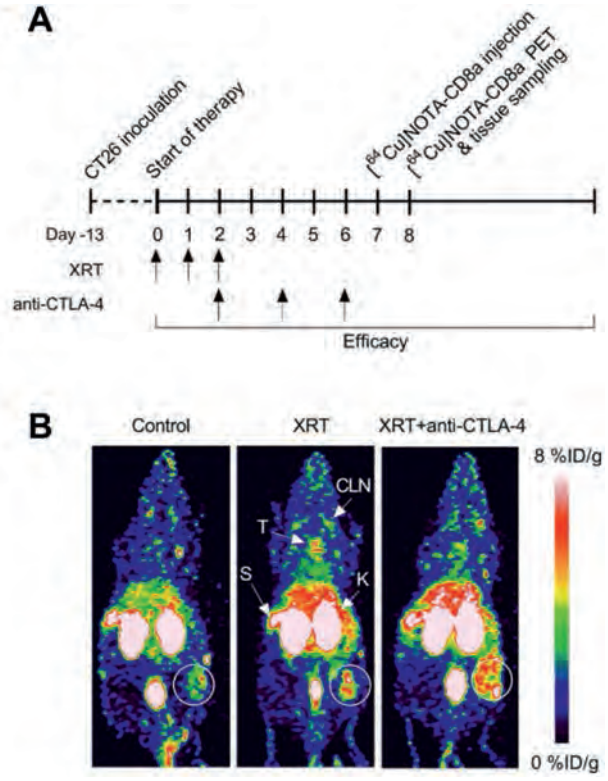

Figure 16 ImmunoPET imaging of $CD8^+$ T cells expression. (A) Overview of the timing for model establishment, therapy regimen, and [^{64}Cu]Cu-NOTA-CD8a injection and scanning. Radiation therapy (XRT) was administered in fractionated doses over three consecutive days (3 × 2 Gy), and anti-mouse CTLA-4 antibody was administered intraperitoneally at 10 mg/kg on three occasions. (B) Representative maximum intensity projection PET images of a mouse from each treatment group at 24 h p.i. of [^{64}Cu]Cu-NOTA-CD8a, illustrating uptake primarily in lymphoid tissues and tumors. The images highlight uptake in the thymus (T), cervical lymph nodes (CLN), spleen (S), kidneys (K), and tumors (designated by circles). Reprinted with the permission from Ref. 50. Copyright © 2020 Springer.

their pharmacokinetics and minimize off-target effects, which could potentially lead to more effective and less invasive diagnostic tools for GBM.

5.7.2. *Glypican-3*

Hepatocellular carcinoma (HCC) stands as one of the most lethal malignancies worldwide, with its management critically dependent on precise imaging for both diagnosis and treatment planning. Conventional imaging techniques such as multiphase CT and MRI, while widely used, are limited by spatial resolution and tissue specificity. Glypican-3 (GPC3), a cell surface receptor, is notably overexpressed in most cases of HCC and presents a promising target for molecular diagnostics[127].

Sham et al.[60] produced F(ab′)$_2$ fragments from αGPC3 mAbs through immobilized ficin digestion, achieving a 26% yield. immunoPET imaging using these fragments provided clear visualization of HepG2 (GPC3-positive) tumors as early as 4 h p.i. of [^{89}Zr]Zr-αGPC3-F(ab′)$_2$. Notably, the peak tumor-to-liver contrast ratio reached 23.3 at 24 h, significantly enhancing tumor-to-liver contrast ratios and reducing imaging times compared to whole mAbs (Fig. 19)[60]. These findings underscore the potential of [^{89}Zr]Zr-αGPC3-F(ab′)$_2$ as an effective imaging agent in HCC. Moving forward, it is crucial to conduct clinical trials to evaluate the safety, efficacy, and potential nephrotoxicity of [^{89}Zr]Zr-αGPC3-F(ab′)$_2$ in human patients, potentially paving the way for its integration into routine clinical practice for HCC management.

5.8. *Carcinoembryonic antigen*

Carcinoembryonic antigen (CEA) is a tumor-associated antigen predominantly synthesized by tumor cells, playing roles in cell adhesion, proliferation, differentiation, and metastasis[128]. hMN-14 is a humanized monoclonal antibody that targets CEA. Lütje et al.[13] advanced the field by developing a two-step [^{18}F]AlF-labeling method designed to maintain the integrity of heat-sensitive antibody fragments. Their study revealed that the [^{18}F]AlF-hMN-14-Fab and [^{18}F]AlF-hMN-14-Fab-AD2 fragments achieved higher tumor-to-blood ratios compared to the diabody format, indicating their enhanced imaging capabilities. These results underscore the potential of using [^{18}F]AlF-labeled antibody fragments for specific, high-contrast PET imaging of CRC. However, the significant uptake of these labeled fragments in the liver and kidneys pose challenges for imaging tumors in these regions.

Additionally, the integration of a radiofluorinated prosthetic group with the Fab fragment is under investigation. Richard et al.[129] successfully developed a radiofluorinated dibromopyridazine dione prosthetic group specifically for disulfide rebridging, demonstrating its efficacy in labeling disulfide-containing biomolecules. This innovative method results in the production of homogeneous, well-defined labeled biomolecules that retain their biological activity, offering promising avenues for the development of precise and effective diagnostic tools in oncology.

5.9. *TREM2*

Triggering receptor expressed on myeloid cells 2 (TREM2), a single-pass membrane receptor of the immunoglobulin superfamily, is primarily expressed on the surfaces of microglia and macrophages[130]. Shi et al.[10] developed a monoclonal antibody (5-mAb) targeting hTREM2, which was subsequently fragmented into F(ab′)$_2$ fragments to enhance tissue penetration and reduce circulation time. These fragments were successfully labeled with ^{124}I using the Iodogen method, resulting in the creation of [^{124}I]I-5-F(ab′)$_2$—an effective imaging agent for the diagnosis of gastric carcinoma. The tracer demonstrated high specificity for hTREM2, exhibiting a rapid clearance from the bloodstream, significant tumor uptake, and excellent imaging contrast. These characteristics make [^{124}I]I-5-F(ab′)$_2$ a promising tool for improving the diagnosis of gastric cancer, particularly in instances where traditional [^{18}F]-FDG PET imaging falls short. This advancement could significantly enhance diagnostic accuracy and facilitate earlier treatment interventions for gastric cancer patients.

Recognizing the limitations associated with ^{124}I, such as its challenging acquisition and long half-life which have impeded clinical adoption, Shi et al.[61] endeavored to develop novel molecular probes targeting TREM2 that would be more suitable for clinical use. To address these challenges, they synthesized a new probe, [^{99m}Tc]Tc-MAG$_3$-5-Fab, which demonstrated pharmacokinetics and imaging performance improvement. The uptake measurements for [^{99m}Tc]Tc-MAG$_3$-5-Fab in targeted tissues at 1, 3, and 6 h p.i. were 1.14 ± 0.17, 1.63 ± 0.06, and 1.86 ± 0.22,

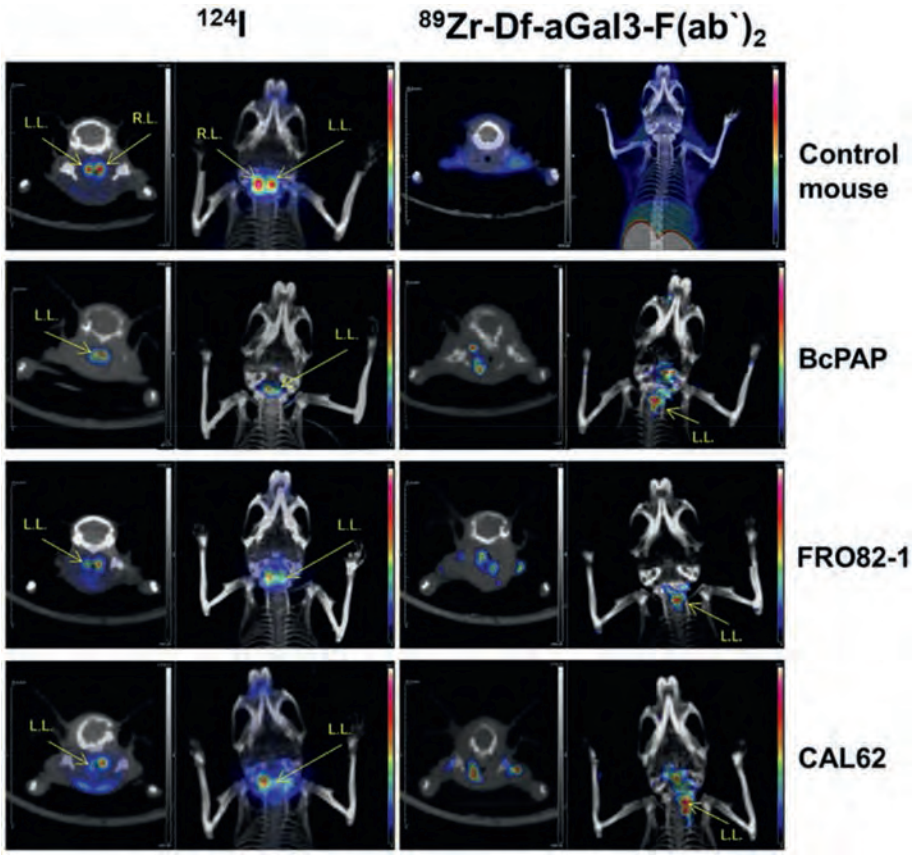

Figure 17 ImmunoPET imaging of Galectin3 expression. In control mice injected with [^{124}I]I−NaI, radioiodine accumulation was observed in both thyroid lobes within 1 h. Control mice injected with [^{89}Zr]Zr-DFO-aGal3-F(ab′)$_2$ showed no accumulation in the normal thyroid. Tumor-bearing mice exhibited strong ^{124}I accumulation in the right thyroid, with a weaker and progressively decreasing signal in the left thyroid across models, with BcPAP > FRO82-1 > CAL62, respectively. In contrast, a strong signal confined to the left thyroid was evident in all mouse models injected with [^{89}Zr]Zr-DFO-aGal3-F(ab′)$_2$. L. L. = left lobe; R. L. = right lobe. Reprinted with the permission from Ref. 53. Copyright © 2019 SNMMI.

respectively. Notably, the probe provided clear tumor visualization while maintaining low uptake in non-tumor tissues, showcasing its potential for enhanced lung cancer imaging (Fig. 20)[61].

5.10. Tenascin-C (TNC)

Inflammation following myocardial infarction (MI) plays a critical role in ventricular remodeling, which can lead to severe complications such as congestive heart failure and arrhythmia. Early detection and precise monitoring of cardiac inflammation are essential for effective management of these conditions. Tenascin-C (TNC), a large extracellular matrix (ECM) glycoprotein belonging to the matricellular protein family, is typically minimally expressed under normal conditions but is significantly upregulated in response to tissue injury and inflammation[131].

Ageyama et al.[62] conducted a pivotal study validating the use of [^{111}In]In-labeled TNC Fab fragments for non-invasive imaging of myocardial inflammation in a primate model. This study serves as a crucial bridge between rodent research and potential human clinical applications. It was concluded that [^{111}In]In-TNC Fab imaging effectively identifies inflammatory regions within the hearts of cynomolgus monkeys post-MI. The imaging outcomes demonstrated strong correlation with histological evaluations, underscoring the potential of this method as a non-invasive tool for detecting cardiac inflammation.

5.11. RANKL

The receptor activator of nuclear factor kappa B ligand (RANKL) is a type 2 transmembrane protein belonging to the tumor necrosis factor (TNF) superfamily. Under normal physiological conditions, RANKL and its receptor, RANK, primarily regulate bone remodeling by initiating osteoclast formation and activation. Beyond its role in bone metabolism, RANKL is also implicated in various cancer-related processes, including the regulation of immune suppression within the tumor microenvironment (TME)[132].

Dewulf et al.[63] addressed the limitations of previous imaging agents, such as an [^{89}Zr]Zr-DFO-denosumab tracer that exhibited prolonged blood circulation and delayed tumor uptake. In response, they developed a smaller, radiolabeled Fab fragment of denosumab, designated as [^{64}Cu]Cu-NOTA-denos-Fab, to enhance imaging characteristics. The radiolabeling yield of this novel tracer was 58 ± 9.2%, with a specific activity of 0.79 ± 0.11 MBq/μg, showing potential for improved performance in clinical imaging applications. However, the study was primarily conducted using a single xenograft model. For broader validation and to establish its efficacy and safety profiles more robustly,

additional studies involving diverse models and clinical samples are essential.

5.12. Interleukin-6

Interleukin-6 (IL-6) is a crucial cytokine in innate immunity, performing a wide range of physiological functions that are traditionally linked to the host defense, regulation, proliferation, and differentiation of immune cells[133]. The IL-6 receptor (IL-6R) is uniquely targeted by IL-6. Tocilizumab, a humanized monoclonal antibody against IL-6R, has been utilized in therapeutic contexts. Camacho et al.[64] developed dual-labeled Fab fragments of Tocilizumab, incorporating both ^{99m}Tc for SPECT/CT imaging and Cy7 for fluorescent imaging, aiming for targeted imaging of IL-6R in multiple myeloma (MM). The SPECT/CT and fluorescent imaging results demonstrated the capability of these labeled Fab fragments in detecting MM tumors effectively. The innovation of creating a hybrid, radioactive and fluorescent probe using Fab (Tocilizumab) is particularly intriguing. This approach not only leverages the strengths of both imaging modalities but also sets the stage for the application of advanced surgical guidance techniques.

5.13. Endothelin A receptor

A key factor in GBM's recurrence and resistance are glioblastoma stem cells (GSCs). The endothelin A receptor (ETA), which is overexpressed in GSCs and notably within GBM's vascular endothelium, has emerged as a potential therapeutic target[134,135]. Hautiere et al.[65] developed an antibody, rendomab A63 (RA63), targeting the human ETA receptor and further explored its chimeric version (xiRA63) and its Fab fragment (ThioFab-xiRA63) for their potential in imaging and therapeutic applications in GBM through immunoPET technology. The study found that [^{89}Zr]Zr-xiRA63, the full-length antibody, is a promising candidate for specifically targeting and imaging ETA-positive GBM. It demonstrated superior tumor retention and higher specific uptake compared to the Fab fragment. This finding positions the full-length antibody as a viable option for future clinical applications, both as a diagnostic and potentially as a therapeutic agent.

5.14. PV1

Kidney diseases, particularly chronic kidney disease (CKD), are a significant global health issue due to their widespread prevalence and the limited effectiveness of current treatments. These treatments often have a narrow therapeutic index, constraining their efficacy and potentially causing severe side effects[136,137]. A promising approach to enhance kidney disease treatments involves targeted drug delivery systems designed to increase drug concentration specifically in the kidneys while reducing systemic exposure and minimizing side effects. Antibody-based therapeutics are well-suited for this purpose because of their specific targeting capabilities and the potential for customization to different molecular targets[138].

Plasmalemma vesicle-associated protein (PV1), a protein associated with caveolae, is found predominantly in the lungs and kidneys[139,140]. Research has shown that systemic administration of monoclonal antibodies against PV1 can selectively target these organs[139,141]. Building on this premise, Li et al.[66] developed a delivery system that utilizes F(ab′)$_2$ fragments targeting PV1 for the kidneys. The main focus of their research was to adjust the binding affinity of the anti-PV1 antibodies to enhance their specificity for kidney tissue. By using F(ab′)$_2$ fragments, they took advantage of the smaller size of these molecules for improved tissue penetration and faster clearance, which is crucial for effective kidney targeting. This strategy, which combines kidney filtration and specific PV1 targeting, provides a novel framework for developing targeted therapies for kidney diseases.

5.15. PS

Laforest et al.[67] conducted the development and first-in-human evaluation of [^{124}I]I-PGN650, a PET tracer intended to detect phosphatidylserine (PS) as a biomarker within the solid tumor microenvironment. Phosphatidylserine is normally positioned on the inner leaflet of the cell membrane but shifts to the outer leaflet in response to cellular stress, apoptosis, and other prevalent conditions in tumors. This translocation makes PS an appealing target for both imaging and potential therapeutic applications. The study involved eleven patients with biopsy-proven solid tumors. Observations showed mild to minimal uptake of the tracer in known tumor sites, with the highest uptake recorded during the latest imaging time points. The average tumor SUV_{max} was 4.02, and the T/B ratio was 0.62. These initial clinical findings indicate the safety and efficacy of [^{124}I]I-PGN650 in imaging solid tumors. To further substantiate these findings and to assess the broader applicational scope of [^{124}I]I-PGN650 across various tumor types and therapeutic settings, it is recommended that larger studies be conducted, and efficacy findings and to explore the full potential of [^{124}I]I-PGN650 in different tumor types and treatment settings.

5.16. β-Glucans

Invasive fungal infections (IFIs), such as pulmonary aspergillosis, pose significant health risks, particularly to immunocompromised individuals. Diagnosing these infections is notoriously challenging due to the low sensitivity and specificity of traditional diagnostic tests. Conventional imaging methods often struggle to differentiate fungal infections from bacterial or viral infections, neoplasms, or inflammatory processes. Molecular imaging methods such as PET, hold the potential for rapid, non-invasive, and accurate diagnostics if appropriate tracers are developed. One promising target for such imaging is the fungal cell wall, particularly β-glucans. These structures are unique to fungi and play crucial roles in fungal growth, viability, and virulence. They also stimulate the immune system by activating Dectin-1, a pattern-recognition receptor (PRR), which triggers the innate immune response[142].

Lai et al.[68] advanced this field by developing a novel [^{89}Zr]Zr-labeled Fab fragment specifically targeting β-glucans, aimed at the precise detection of fungal infections. Their study concluded that [^{89}Zr]Zr-DFO-HA-βG-Fab is a promising tracer for non-invasive PET imaging of Aspergillus infections. This tracer exhibited high specificity for fungal pathogens, effectively distinguishing them from bacterial infections and sterile inflammation, thereby significantly enhancing the capabilities beyond those of conventional imaging methods. However, some level of binding to bacterial infections was noted, suggesting potential cross-reactivity. This finding highlights the need for further refinement of the tracer to improve its specificity and ensure its reliability in clinical settings (Fig. 21)[68].

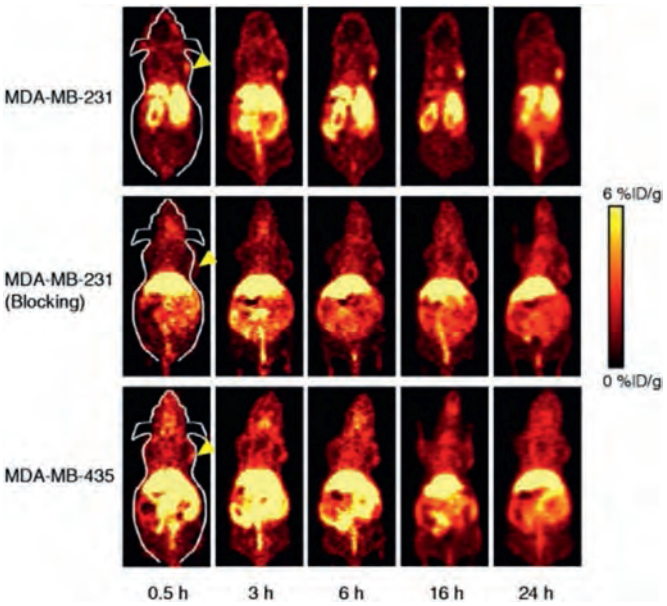

Figure 18 ImmunoPET imaging of TF expression. PET images were acquired at different time points following the injection of [^{64}Cu]Cu-NOTA-ALT-836-Fab in MDA-MB-231 tumor-bearing mice, MDA-MB-231 tumor-bearing mice pre-injected with 2 mg ALT-836 (blocking), and MDA-MB-435 tumor-bearing mice. The results demonstrate that MDA-MB-231 tumors became clearly visible as early as 0.5 h p.i. (3.0 $\pm$ 0.2%ID/g) and remained relatively stable through 24 h p.i. (3.9 $\pm$ 0.5, 4.6 $\pm$ 0.8, 4.7 $\pm$ 0.2, 5.1 $\pm$ 0.5%ID/g at 3, 6, 16, and 24 h, respectively). Reprinted with the permission from Ref. 56. Copyright © 2015 Springer.

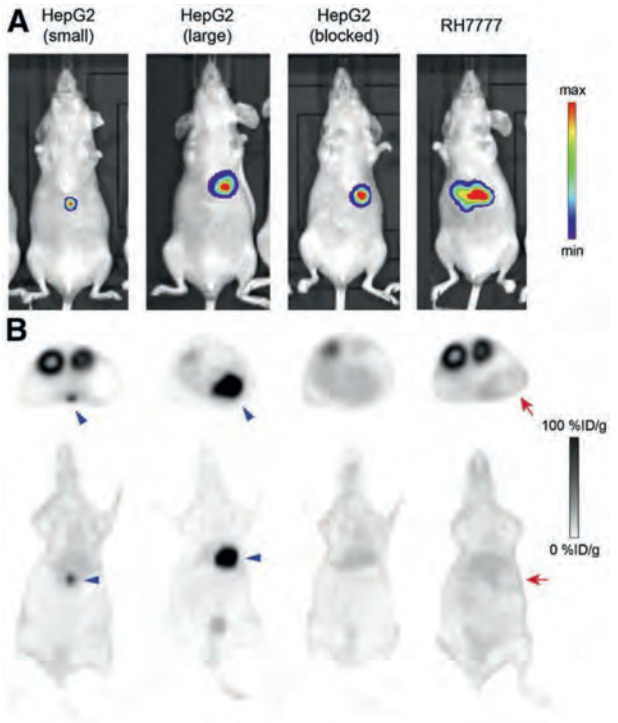

Figure 19 ImmunoPET imaging of Glypican-3 expression. (A) IVIS luminescent images captured after intraperitoneal administration of luciferin (75 mg/kg), verifying the presence of intrahepatic tumors prior to the administration of [^{89}Zr]Zr-αGPC3-F(ab′)$_2$. (B) Axial and coronal PET images of the same animals, taken 24 h post-injection, demonstrating tumor concordance in HepG2-bearing mice and the absence of PET signal in RH7777 tumors and blocked HepG2 controls. Blue arrowheads indicate HepG2 tumors, while red arrows point to RH7777 tumors. Reprinted with the permission from Ref. 60. Copyright © 2014 SNMMI.

5.17. Malondialdehyde-acetaldehyde

Atherosclerosis is a chronic inflammatory disease that primarily affects medium and large arteries and is the leading cause of cardiovascular disease (CVD). The disease progresses through the accumulation and oxidation of lipids, leading to chronic inflammation and the formation of advanced plaques that are prone to rupture and thrombotic events. Oxidation-specific epitopes (OSEs), such as malondialdehyde-acetaldehyde (MAA) epitopes, are indicators associated with high cardiovascular risk[143].

In their innovative study, Senders et al.[69] investigate the potential of a novel PET radiotracer, [^{89}Zr]Zr-labeled human antibody Fab fragment LA25, which targets MAA epitopes for noninvasive imaging of atherosclerotic lesions. This research was conducted in atherosclerotic mice and rabbits, where [^{89}Zr]Zr-LA25 demonstrated significantly higher uptake in atherosclerotic lesions compared to controls and non-relevant epitopes. The tracer exhibited high specificity for OSEs, making it a potentially valuable tool for identifying high-risk atherosclerotic plaques and potentially guiding therapeutic interventions. However, it is noted that partial volume effects might have influenced the measurement values in the aortic vessel wall, although SUV_{max} is a well-established parameter in nuclear imaging. In a clinical setting, target-to-blood ratios might be employed to compensate for these effects, enhancing the diagnostic accuracy of this imaging technique. This approach could lead to improved risk assessment and patient-specific management in cardiovascular care.

5.18. Matrix metalloproteinases

IBD, which includes Crohn's disease and ulcerative colitis, involves chronic, episodic inflammation of the lower gastrointestinal tract. A prevalent complication associated with IBD is intestinal fibrosis, leading to stricture and stenosis in approximately 30% of patients. This condition results from recurrent inflammation episodes that promote excessive ECM proteins, such as collagen, contributing to the development of these obstructions[144].

Dmochowska et al.[19] have pioneered the use of immunoPET imaging to address this issue through the deployment of [^{89}Zr]Zr-labeled pro-MMP-9 F(ab′)$_2$ fragments, targeting matrix metalloproteinases (MMPs), particularly pro-MMP-9, which are key players in the fibrotic process. Their study demonstrated that [^{89}Zr]Zr-pro-MMP-9 F(ab′)$_2$ fragments had significantly higher uptake in the colon and kidneys of fibrotic mice, as validated by PET imaging and subsequent *ex-vivo* analysis. This suggests a potent non-invasive method for diagnosing fibrosis effectively. Furthermore, the study underscored the presence of kidney fibrosis within the DSS-induced colitis model, highlighting the dual diagnostic capability of immunoPET to identify fibrosis in multiple organs. This dual-functionality underscores the potential of immunoPET not only in diagnosing but also in potentially guiding therapeutic approaches for fibrosis in IBD and beyond.

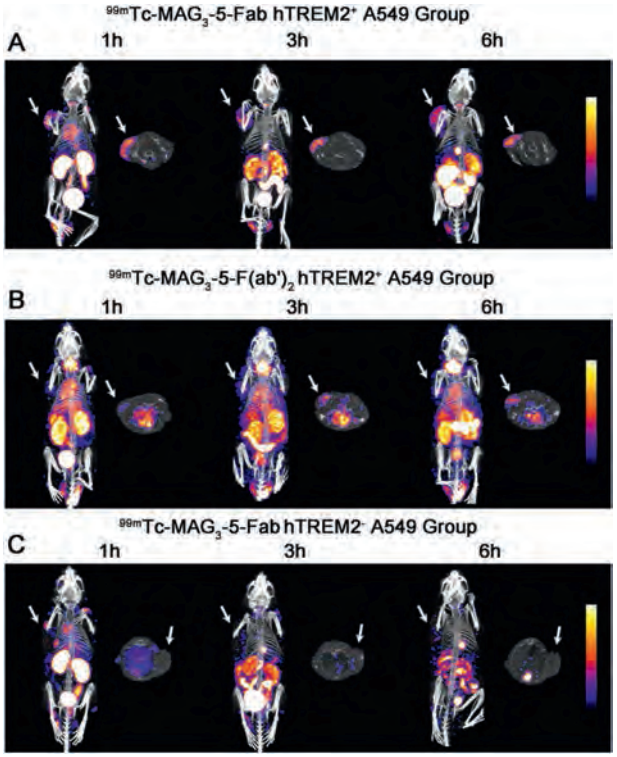

Figure 20 ImmunoSPECT imaging of TREM2 expression. (A) In the hTREM2+ A549 group, [^{99m}Tc]Tc-MAG$_3$-5-Fab was concentrated in the hTREM2+ A549 tumor, blood, kidneys, and bladder 1 h p.i. By 3 h, the concentration of [^{99m}Tc]Tc-MAG$_3$-5-Fab increased at the tumor site, and by 6 h, the imaging agent was even more concentrated in the tumor. (B) In the hTREM2+ A549 group, the concentration of [^{99m}Tc]Tc-MAG$_3$-5-Fab in the tumor site showed a slight increase over time. (C) In the hTREM2− A549 group, no tumor imaging was observed at 1, 3, or 6 h p.i. of [^{99m}Tc]Tc-MAG$_3$-5-Fab, indicating the favorable *in vivo* specificity of [^{99m}Tc]Tc-MAG$_3$-5-Fab. Reprinted with the permission from Ref. 61. Copyright © 2024 American Chemical Society.

6. Future perspectives and challenge

Targeted therapy represents a transformative advancement in cancer treatment. Fab and F(ab′)$_2$ fragments maintain antigen-specific binding capabilities while eliminating the limitations associated with mAbs, such as prolonged circulation half-lives and inconsistent clinical outcomes. Moreover, these fragments exhibit superior biochemical properties. A wide array of molecular targets is being extensively explored in immunoPET/SPECT studies. Fab and F(ab′)$_2$ fragments provide significant advantages for immunoPET/SPECT applications by substantially reducing the time between injection and imaging to mere hours, as opposed to the days required for clearance of whole antibodies. A variety of PET/SPECT radionuclides, including ^{18}F, ^{68}Ga, ^{124}I, and ^{64}Cu, have been employed to label Fab and F(ab′)$_2$ fragments for imaging studies, chosen for their availability and half-lives that align with the biological clearance rates of these fragments. These labeled probes also avoid the nonspecific bone accumulation observed with [^{89}Zr]Zr-labeled probes. Furthermore, the introduction of novel radionuclides with optimal physical characteristics, such as ^{44}Sc, is propelling the development of imaging agents based on Fab and F(ab′)$_2$ fragments.

As advancements in both therapeutic and diagnostic Fab and F(ab′)$_2$ fragment developments continue, innovative and gentle labeling techniques that are rapid, site-specific, and robust will be critical in delineating their biological behaviors and expediting their clinical application. Yue et al.[145] have harnessed oxaziridine chemistry to modify methionine residues precisely, creating well-defined immunoconjugates and developing a site-specific method for radiolabeling trastuzumab-derived Fab with ^{68}Ga. This technique can be adapted for other radiometals and Fab derivatives, enhancing its utility across diverse imaging scenarios. Drake et al.[87] have adopted lipoic acid ligase (LplA) to attach [^{18}F]-fluorooctanoic acid ([^{18}F]-FA) to antibody fragments in a site-specific manner under conditions that preserve the functionality of these critical biomolecules. Cai and colleagues[146] have innovated a site-specific PD-L1 Fab conjugate using unnatural amino acid (UAA) technology, significantly improving PET imaging. They demonstrate that the site-specific [^{64}Cu]Cu-NOTA-αPD-L1 Fab conjugate provides highly specific and sensitive imaging of PD-L1 expression. These research initiatives highlightthe profound impact of advanced chemistry on imaging technology. Continued development of new bioconjugation and chelation techniques is likely to revolutionize fragment labeling protocols, markedly influencing their clinical implementation.

A diverse array of prosthetic groups and conjugation techniques now enables reliable labeling of antibody fragments, yet there remains considerable potential for enhancing labeling efficiency, radiochemical yields, and procedural simplicity. The rapid advancement in novel labeling pathways, cutting-edge bioconjugation strategies, and improved chelator chemistry underscores this evolving field[147]. Critical considerations for fragment labeling include aligning the radionuclide's properties with the fragment's pharmacokinetics, conducting labeling under mild conditions to preserve fragment integrity, and ensuring specific site labeling to maintain the fragment's immunoreactivity with its target.

The enzymatic digestion of intact antibodies using enzymes such as papain or pepsin produces Fab and F(ab′)$_2$ fragments; however, these methods are not universally applicable to all antibody subclasses and often require substantial quantities of starting material. Nonetheless, the rapid progress in antibody engineering has facilitated more straightforward preparation methods, reducing the complexity and resource demands of traditional biochemical techniques.

A significant challenge in the use of radiolabeled Fab and F(ab′)$_2$ fragments for nuclear imaging is the high and persistent localization of radioactivity in the kidneys following injection, which can obscure target visualization and increase radiation exposure to non-target tissues[148]. This undesirable accumulation is attributed to the prolonged retention of radiometabolites formed after lysosomal proteolysis of the radiolabeled fragments, which undergo glomerular filtration and subsequent reabsorption in renal cells[149]. This issue persists across various applications of antibody fragments in nuclear imaging. Efforts to mitigate renal radioactivity have included strategies to block or reduce the tubular reabsorption of radiolabeled Fab and F(ab′)$_2$ fragments, such as the pre- or co-injection of basic amino acids like L-lysine or the use of plasma expanders. Additionally, facilitating the excretion of radiometabolites from the renal lysosomal compartment into the urine has been explored. A notable advancement was made by Uehara et al.[149], who developed a $^{67/68}$Ga-labeled Fab fragment

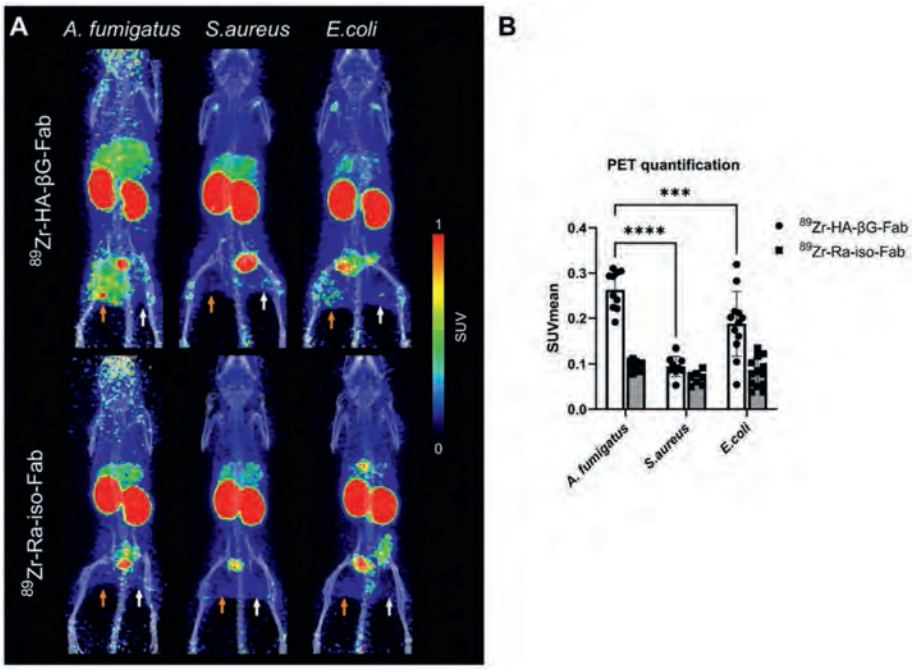

Figure 21 ImmunoPET imaging of β-glucans. (A, B) PET imaging with [^{89}Zr]Zr-DFO-HA-βG-Fab and [^{89}Zr]Zr-DFO-HA-βG-Fab in mice with *A. fumigatus*, *S. aureus*, and *E. coli*, 24 h post-tracer injection. [^{89}Zr]Zr-DFO-HA-βG-Fab binding was higher in A. fumigatus-infected thighs compared to *S. aureus*-infected thighs, with SUV_{mean} values of 0.26 $\pm$ 0.04 *vs.* 0.09 $\pm$ 0.02 for live infections and 0.22 $\pm$ 0.06 *vs.* 0.12 $\pm$ 0.03 for heat-killed inoculations. Reprinted with the permission from Ref. 68. Copyright © 2024 Springer.

connected through a Met-Val-Lys (MVK) sequence designed for enzymatic cleavage by brush border membrane (BBM) enzymes, allowing for the release of the radiolabel without compromising tumor uptake. This represents a promising solution to the problem of renal accumulation. Suzuki et al.[150] extended this technique to ^{64}Cu, focusing on the nuances of charge and enzyme recognition differences compared to ^{68}Ga, further exploring the potential of this approach in reducing renal retention.

The development of labeled Fab and F(ab′)$_2$ fragments is undeniably a lengthy, challenging, and costly endeavor, involving the selection of a suitable fragment, precise radiolabeling, and extensive preclinical testing. The path to clinical application is fraught with regulatory challenges and the complexities of scaling up production processes. While some studies have reported suboptimal tumor uptake and other limitations[151], both successes and failures offer valuable insights that enhance our understanding in pharmacology and biomanufacturing. Despite these challenges, the development of novel antibody fragment imaging agents may offer a more time-efficient and cost-effective alternative compared to full antibody agents. This advantage stems from their faster production, selection, and characterization processes. Fab and F(ab′)$_2$ fragments hold significant potential for medical imaging due to their high affinities, targeted specificity, and rapid clearance from the body. Future advancements in this field will rely on identifying new Fab and F(ab′)$_2$ fragments with optimal imaging characteristics such as high target affinity, selectivity, stability, rapid clearance, and ease of labeling. These developments hold the promise of expanding the capabilities and applications of nuclear imaging.

The primary aim of developing and utilizing Fab and F(ab′)$_2$ fragments for immunoPET/SPECT imaging is to enhance patient management, aid clinicians in refining medical practices, and facilitate the realization of truly personalized medicine. However, it is important to recognize that the majority of immunoPET/SPECT Fab and F(ab′)$_2$ fragment probes have been evaluated primarily in preclinical settings or small patient cohorts. Extensive research is required to advance promising immunoPET/SPECT probes to clinical application and to validate the diagnostic efficacy of those already in clinical use. Moreover, the availability of radionuclides and the ongoing advancement of radiochemistry and coordination chemistry are critical factors that must be addressed to enable widespread clinical adoption of these imaging technologies.

Fab and F(ab′)$_2$ fragments undoubtedly represent a promising platform for drug development. In future advancements, these fragments will prove instrumental not only in constructing targeted drug delivery systems but also in developing bsRICs[152−154]. The design of targeted delivery systems can leverage the robust penetrability and specificity of these fragments while mitigating the impact of structural limitations. Despite the significant advantages offered by Fab and F(ab′)$_2$ fragments, they are not poised to replace full-intact antibodies in imaging applications entirely. The use of longer-lived isotopes like ^{89}Zr for labeling intact antibodies provides sustained imaging data over extended periods. Additionally, pre-targeting strategies that involve administering functionalized antibodies to bind to targets, followed by a positron-emitting labeled molecule that conjugates *in vivo*, allow for the utilization of shorter-lived PET radionuclides[7]. Although antibody fragments are still undergoing exploration and development compared to traditional antibodies used clinically, their outstanding biochemical properties and the current trajectory of

Table 1 Theranostic applications of immunoPET/SPECT imaging using Fab and F(ab′)$_2$ fragments.

Probe name	Imaging	Finding	Limitation	Ref.	Year	Targeting
[^{64}Cu]Cu-DOTA-cetuximab-F(ab′)$_2$	ImmunoPET	The probe showed high TBR in control mice and maintained high TBR in the presence of colitis. Tumor to bowel ratio for [^{64}Cu]Cu-DOTA-cetuximab-F(ab′)$_2$ was 4.42 ± 0.11 in control mice and 3.78 ± 0.06 in the setting of colitis.	The research focused primarily on imaging, with limited exploration of therapeutic applications.	14	2014	EGFR
[^{44}Sc]Sc-CHX-A″-DTPA-cetuximab-Fab	ImmunoPET	PET imaging and biodistribution studies in U87MG tumor-bearing mice showed rapid tumor uptake (12.7 ± 0.7% ID/g at 4 h p.i.) and high tumor-to-background ratios. Blocking studies confirmed the specificity of the radiolabeled Fab fragments for EGFR.	The multi-step synthesis and conjugation process may pose challenges for large-scale production and clinical application	20	2014	EGFR
[^{64}Cu]Cu-NOTA-cetuximab-F(ab′)$_2$	ImmunoPET	The use of protein-A affinity chromatography ensures the removal of Fc fragments, enhancing the binding specificity and therapeutic efficacy of the radiolabeled Fab fragments. The maximum tumor uptake of the purified radiolabeled cetuximab-Fab was 15.2 ± 1.9%ID/g at 6 h p.i.	The process for producing and purifying Fab fragments and radiolabeling them needs to be scaled up for routine clinical use, which may present logistical challenges.	21	2023	EGFR
[^{64}Cu]Cu-DOTA-panitumumab F(ab′)$_2$	ImmunoPET	PET imaging revealed significant tumor uptake and high contrast images within 24 h p.i., indicating the tracer's potential for rapid and specific tumor imaging. Uptake in MDA-MB-231 tumors was 7.2 ± 1.8%ID/g at 2 h p.i.	The study was conducted in mouse models, necessitating further validation in human clinical trials.	22	2021	EGFR
[^{64}Cu]Cu-DOTA-panitumumab F(ab′)$_2$; [^{177}Lu]Lu-DOTA-panitumumab F(ab′)$_2$	ImmunoPET/ImmunoSPECT	[^{64}Cu]Cu-DOTA-panitumumab F(ab′)$_2$ is effective for PET imaging of EGFR-positive HNSCC tumors and can accurately predict the radiation doses from RIT with [^{177}Lu]Lu-DOTA-panitumumab F(ab′)$_2$. In this study, [^{177}Lu]Lu-DOTA-panitumumab F(ab′)$_2$ demonstrated the highest tumor uptake at 24 h, with a value of 18.0 ± 0.4%ID/g, while [^{64}Cu]Cu-DOTA-panitumumab F(ab′)$_2$ had a tumor uptake of 14.9 ± 1.1%ID/g at the same time point.	The study was conducted in mouse models, necessitating further validation in human clinical trials.	23	2021	EGFR
[^{64}Cu]Cu-labeled pmabF(ab′)$_2$-MCP-2PEG$_{2K}$; [^{64}Cu]Cu-labeled pmabF(ab′)$_2$-MCP-8PEG$_{2K}$	ImmunoPET	MCPs with multiple PEG$_{2K}$ chains significantly improve the specificity and contrast of EGFR-targeted PET imaging of pancreatic cancer. In this study, the tumor uptake of [^{64}Cu]Cu-labeled pmabF(ab′)$_2$-PGlu(DOTA)-2PEG$_{2K}$ was higher (7.3 ± 0.2%ID/g) compared to [^{64}Cu]Cu-labeled pmabF(ab′)$_2$-PGlu(DOTA)-8PEG$_{2K}$ (4.9 ± 0.5%ID/g), indicating that fewer PEG chains may enhance tumor targeting efficiency.	The synthesis and conjugation process for MCPs with multiple PEG chains can be complex and may require optimization for large-scale production.	24	2017	EGFR
[^{99m}Tc]Tc-labeled cetuximab F(ab′)$_2$	ImmunoSPECT	The imaging agent provided rapid and sustained high contrast in EGFR-positive tumors, demonstrating its potential utility in clinical settings. In this study, [^{99m}Tc]Tc-labeled cetuximab F(ab′)$_2$ showed peak tumor uptake of 13.51 ± 2.17%ID/g at 16 h p.i.	The study was conducted in mouse models, necessitating further validation in human clinical trials.	25	2022	EGFR

[^{111}In]In-DOTAGA-F(ab′)$_2$-cetuximab; [^{177}Lu]Lu-DOTAGA-F(ab′)$_2$-cetuximab	ImmunoSPECT	By radiolabeling these fragments with ^{111}In and ^{177}Lu, the study addressed the challenges of accurate imaging and effective therapy for EGFR-expressing tumors. [^{111}In]In-DOTAGA-F(ab′)$_2$-cetuximab exhibited peak tumor uptake of 8.0 ± 1.0%ID/g at 24 h p.i., while [^{177}Lu]Lu-DOTAGA-F(ab′)$_2$-cetuximab effectively reduced tumor volume at doses of 4 and 8 MBq, demonstrating its potential as a theranostic agent.	The study was conducted in preclinical models, requiring further validation in clinical trials.	26	2018	EGFR
[^{64}Cu]Cu-NOTA-panitumumab F(ab′)$_2$	ImmunoPET	[^{64}Cu]Cu-NOTA-panitumumab F(ab′)$_2$ fragments are effective for PET imaging of EGFR-positive pancreatic cancer. [^{64}Cu]Cu-NOTA-panitumumab F(ab′)$_2$ exhibited higher tumor uptake in OCIP23 xenografts (up to 12.0 ± 0.9%ID/g) compared to PANC-1 xenografts (6.1 ± 1.1%ID/g), indicating a more effective targeting of EGFR-positive pancreatic tumors in the OCIP23 model.	The study was conducted in mouse models, necessitating further validation in human clinical trials.	27	2015	EGFR
[^{68}Ga]Ga-NOTA-Fab-trastuzumab; [^{68}Ga]Ga-NOTA-F(ab′)$_2$-trastuzumab	ImmunoPET	[^{68}Ga]Ga-NOTA-Fab-trastuzumab and [^{68}Ga]Ga-NOTA-F(ab′)$_2$-trastuzumab were prepared with high radiolabeling yield (>99%) and high radiochemical purity (>98%), requiring no further purification (which is advantageous for further clinical translation). [^{68}Ga]Ga-NOTA-Fab-trastuzumab showed higher tumor uptake (6.7 ± 0.3%ID/g) compared to [^{68}Ga]Ga-NOTA-F(ab′)$_2$-trastuzumab (4.1 ± 0.4%ID/g) at 3 h p.i., indicating better targeting efficiency of the F(ab′) fragment.	The study focused on short-term stability and biodistribution, requiring longer-term studies for comprehensive evaluation.	28	2023	HER2
[^{68}Ga]Ga-NOTA-trastuzumab-Fab[a]	ImmunoPET	^{68}Ga trastuzumab Fab demonstrated specific uptake in HER2/neu-positive breast cancer lesions and lymph nodes, with SUV_{max} ranging from 3 to 5.8. Phase I clinical trial is currently underway.	High physiological uptake in the liver, kidneys, and blood pool could obscure some metastatic sites and reduce imaging contrast.	29	2022	HER2
[^{64}Cu]Cu-NOTA-trastuzumab-F(ab′)$_2$	ImmunoPET	[^{64}Cu]Cu-NOTA-pertuzumab F(ab′)$_2$ is effective for PET imaging of HER2 expression changes in response to trastuzumab treatment. [^{64}Cu]Cu-NOTA-trastuzumab-F(ab′)$_2$ showed varying tumor uptake in SK-OV-3 xenografts depending on the administered mass, with the highest uptake observed at 9.8 ± 5.1%ID/g for a 50 mg dose at 24 h p.i.	The study was conducted in mouse models, necessitating validation in human clinical trials.	30	2017	HER2
[^{64}Cu]Cu-NOTA-Fab-PEG_{24}-EGF	ImmunoPET	[^{64}Cu]Cu-NOTA-Fab-PEG_{24}-EGF showed high specificity (4.9 ± 0.4%ID/g) for HER2 and EGFR, with significantly higher tumor uptake compared to monospecific agents {[^{64}Cu]Cu-NOTA-trastuzumab Fab (1.9 ± 0.3%ID/g) and [^{64}Cu]Cu-NOTA-EGF (0.7 ± 0.2%ID/g)}.	The need for further optimization to reduce non-specific renal uptake and improve overall imaging specificity.	31	2017	HER2
[^{89}Zr]Zr-Df-Fab-PAS_{200}; [^{124}I]I-Fab-PAS_{200}	ImmunoPET	PET imaging confirmed high tumor-to-blood and tumor-to-muscle ratios for both tracers, with [^{89}Zr]Zr-Df-Fab-PAS_{200} showing better *in situ* stability and higher overall tumor uptake (11.1 ± 1.7%ID/g).	The study's findings are based on mouse models, requiring validation in human clinical trials.	11	2015	HER2

(*continued on next page*)

Table 1 (*continued*)

Probe name	Imaging	Finding	Limitation	Ref.	Year	Targeting
[^{89}Zr]Zr-Df-Fab-PAS$_{200}$[a]	ImmunoPET	The PASylated [^{89}Zr]Zr-labeled anti-HER2 Fab fragment ([^{89}Zr]Zr-Df-HER2-Fab-PAS$_{200}$) is a feasible and safe imaging agent for detecting HER2-positive metastatic breast cancer. Phase I clinical trial is currently underway.	The findings are based on a single patient, limiting the generalizability of the results.	32	2020	HER2
[^{99m}Tc]His$_6$-pertuzumab Fab	ImmunoSPECT	DA-MB-361 tumors (intermediate HER2 expression) had a higher uptake (5.6 ± 1.4%ID/g) than MDA-MB-231 tumors (low HER2 expression, 0.8 ± 0.1%ID/g).	The study's findings are based on mouse models, requiring validation in human clinical trials.	33	2021	HER2
[^{68}Ga]Ga-NOTA-F(ab′)$_2$-rituximab; [^{68}Ga]Ga-NOTA-Fab-rituximab	/	[^{68}Ga]Ga-NOTA-F(ab′)$_2$-rituximab exhibited higher tumor uptake (12.7 ± 0.7%ID/g) compared to [^{68}Ga]Ga-NOTA-Fab-rituximab (6.7 ± 0.5%ID/g), indicating a better targeting efficiency of the F(ab′)$_2$ fragment for CD20-positive lymphoma cells.	The study was conducted *in vitro* and in normal mice, necessitating further validation in NHL animal models and clinical trials.	15	2019	CD20
[^{64}Cu]Cu-NOTA-F(a′)$_2$-obinutuzumab	ImmunoPET	The study concluded that [^{64}Cu]Cu-NOTA-F(ab′)$_2$-obinutuzumab is a promising imaging agent for noninvasive evaluation of CD20 expression in lymphoma. [^{64}Cu]Cu-NOTA-F(ab′)$_2$-obinutuzumab showed significantly higher tumor uptake (9.08 ± 1.67%ID/g) compared to [^{64}Cu]Cu-NOTA-F(ab′)$_2$-IgG (1.93 ± 0.26%ID/g), demonstrating better targeting efficiency for CD20-positive lymphoma cells.	The study was conducted in mouse models, necessitating validation in human clinical trials.	34	2021	CD20
[^{64}Cu]Cu-NOTA-Dara-F(ab′)$_2$	ImmunoPET	The [^{64}Cu]Cu-NOTA-Dara-F(ab′)$_2$ fragment showed rapid and high tumor uptake, peaking at 12 h p.i. with 9.5 ± 0.7%ID/g.	High renal uptake of the [^{64}Cu]Cu-NOTA-Dara-F(ab′)$_2$ fragment due to its smaller size, which might limit its application in imaging tumors near the kidneys.	35	2022	CD38
[^{111}In]In-AbD15179-Fab; [^{125}I]I-AbD15179-Fab	ImmunoPET/ImmunoSPECT	[^{111}In]In-AbD15179-Fab showed higher tumor uptake (4.6 ± 1.9%ID/g) compared to [^{125}I]I-AbD15179-Fab (1.6 ± 0.1%ID/g) in high CD44v6-expressing xenografts at 6 h p.i., indicating a better targeting efficiency.	The study used a limited number of tumor models (A431 and H314), requiring further validation in additional models and clinical samples.	36	2014	CD44v6
[^{124}I]I-AbD19384	ImmunoPET	AbD19384 demonstrated significantly higher uptake in CD44v6-positive A431 tumors compared to CD44v6-negative MDA-MB-231 tumors, confirming its specificity.	Initial high uptake in the thyroid, salivary glands, and stomach due to radiocatabolites needs to be addressed.	37	2015	CD44v6
[^{89}Zr]Zr-hCD103.Fab01A; [^{68}Ga]Ga-CD103.Fab01A	ImmunoPET	[^{68}Ga]Ga-hCD103.Fab01A showed higher tumor uptake (5.4 ± 0.3%ID/g) at 3 h p.i. compared to [^{89}Zr]Zr-hCD103.Fab01A, which had a tumor uptake of 2.28 ± 0.1%ID/g at 24 h. The [^{68}Ga]Ga-hCD103.Fab01A tracer also showed potential but	The study was conducted in mouse models, necessitating further validation in human clinical trials.	38	2023	CD103

		had a shorter effective imaging window due to the shorter half-life of ^{68}Ga.				
[^{64}Cu]Cu-MSN-800CW-TRC105(Fab)	ImmunoPET	The study concluded that [^{64}Cu]Cu-MSN-800CW-TRC105(Fab) is an effective dual-modality imaging agent for targeting CD105 in tumor vasculature.	The multi-step synthesis and conjugation process may pose challenges for large-scale production and clinical application.	39	2014	CD105
[^{64}Cu]Cu-NOTA-TRC105-Fab	ImmunoPET	In this study, [^{64}Cu]Cu-NOTA-TRC105-Fab showed higher uptake in the abdominal aortic aneurysm model on day 5 (9.5 ± 0.4%ID/g) compared to day 12 (7.2 ± 1.4%ID/g), indicating effective targeting of CD105 during the early stages of aneurysm progression.	PET imaging's spatial resolution limitations necessitate further studies to confirm the ability to predict aneurysm rupture.	40	2015	CD105
[^{64}Cu]Cu-NOTA-Bs-F(ab′)$_2$	ImmunoPET	In this study, [^{64}Cu]Cu-NOTA-Bs-F(ab′)$_2$ demonstrated significantly higher tumor uptake (47.5 ± 6.7%ID/g) compared to the individual Fab fragments (14.4 ± 1.1%ID/g and 14.3 ± 6.6%ID/g), highlighting the synergistic targeting advantage of the bispecific construct.	The synthesis of bispecific fragments *via* click chemistry may be complex and require optimization for large-scale production.	41	2015	CD105 and EGFR
[^{89}Zr]Zr-Df-F(ab′)$_2$	ImmunoPET	PET imaging demonstrated superior pharmacokinetics and imaging contrast of [^{89}Zr]Zr-Df-F(ab′)$_2$ over the full antibody, with higher tumor uptake (7.5 ± 0.5%ID/g) and lower liver background.	The study's findings are based on mouse models, requiring validation in human clinical trials.	42	2020	PDL1
[^{124}I]I-Durva-F(ab′)$_2$	ImmunoPET	The peak tumor uptake (5.29 ± 0.42%ID/g) of [^{124}I]I-Durva-F(ab′)$_2$ occurred at 12 h p.i., significantly earlier than the 48 h required for [^{124}I]I-Durva.	The study was conducted in preclinical models, necessitating further validation in human subjects.	43	2022	PDL1
[^{124}I]I-HPP-durva F(ab′)$_2$	ImmunoPET	Utilizing SHPP modification to increase the labeling efficiency and specific activity of the antibody fragments.	The study was conducted on only two tumor models (H460 and A549), requiring further validation in additional models and clinical settings.	44	2023	PDL1
[^{89}Zr]Zr-Fab C4	ImmunoPET	Both [^{89}Zr]Zr-Fab C4 and [^{89}Zr]Zr-IgG C4 (H310A/H435Q) provided effective and specific detection of PD-L1 expression in NSCLC models.	The study was conducted in preclinical models, necessitating further validation in human subjects.	45	2022	PDL1
[^{18}F]-FPyOctA-LAP-Fab; [^{89}Zr]Zr-DFO-Fab	ImmunoPET	The study concluded that site-specific radiofluorination using LplA-mediated conjugation produces anti-PD-L1 Fab fragments with superior pharmacokinetics and higher specific activity compared to random radiolabeling methods. [^{89}Zr]Zr-DFO-Fab exhibited higher tumor uptake (1.36 ± 0.11%ID/g) compared to [^{18}F]-FPyOctA-LAP-Fab (0.31 ± 0.12%ID/g) at 4 h p.i.	The enzymatic labeling process, while advantageous, introduces complexity and requires careful optimization for large-scale clinical applications.	46	2022	PDL1
[^{64}Cu]Cu-NOTA-αCD276/Fab	ImmunoPET	IRD-αCD276/Fab showed high tumor uptake and specificity in both subcutaneous and metastatic	The study was conducted in preclinical models,	47	2019	CD276

(*continued on next page*)

Table 1 (*continued*)

Probe name	Imaging	Finding	Limitation	Ref.	Year	Targeting
		tumor models, with significantly higher fluorescence intensity and PET signal compared to control probes.	necessitating further validation in human subjects.			
[^{64}Cu]Cu-NOTA-ipilimumab-F(ab′)$_2$	ImmunoPET	The full antibody provided higher absolute uptake in target tissues, while the F(ab′)$_2$ fragment enabled higher contrast imaging due to faster clearance. [^{64}Cu]Cu-NOTA-ipilimumab demonstrated higher salivary gland uptake (7.00 ± 2.19%ID/g) compared to [^{64}Cu]Cu-NOTA-ipilimumab-F(ab′)$_2$ (2.40 ± 0.86%ID/g) at 24 h p.i.	The study was limited to preclinical models, necessitating further validation in human clinical trials.	48	2019	CTLA
[^{64}Cu]Cu-NOTA-CD4-F(ab′)$_2$	ImmunoPET	In CIA mice, tracer uptake in inflamed joints was significantly higher compared to control mice (15.9 ± 4.4 *vs.* 10.88 ± 0.39%ID/g) ($P < 0.0001$), and PET imaging could distinguish between untreated and dexamethasone (DXM)-treated mice.	Observed non-specific accumulation in severely inflamed tissues, suggesting the need for further refinement.	49	2022	CD4
[^{64}Cu]Cu-NOTA-CD8a-F(ab′)$_2$	ImmunoPET	The tumor uptake (9.25 ± 0.48%ID/g) of [^{64}Cu]Cu-NOTA-CD8a peaked at 3−6 h p.i., with a significant tumor-to-heart ratio increase at 24 and 48 h.	Use of a single tumor model (CT26) limits generalizability; additional models are needed for broader validation.	50	2020	CD8
[^{64}Cu]Cu-DOTA-B-Fab	ImmunoPET	B-Fab showed high stability and immunoreactivity. It allowed differentiation between CA6-positive and CA6-negative tumors as early as 6 h p.i., with a 1.7-fold uptake ratio.	The study was limited to small-animal models, and further validation in human clinical trials is necessary.	51	2015	CA6
[^{177}Lu]Lu-6A10-Fab	ImmunoPET	The initial clinical experience with fractionated iRIT using [^{177}Lu]Lu-labeled 6A10-Fab fragments in glioblastoma patients appears feasible and safe.	The study was conducted on only three patients, limiting the generalizability of the results.	52	2023	CA-XII
[^{89}Zr]Zr-DFO-F(ab′)$_2$ antigal-3	ImmunoPET	The PET/CT imaging revealed specific and selective visualization of thyroid tumors using gal-3 targeting, with no signal detected in the tumor-free thyroid lobe.	Although the F(ab′)$_2$ fragment recognizes both human and mouse gal-3, differences in species-specific expression and immune responses might affect the translational applicability of the findings.	53	2019	Galectin-3
[^{89}Zr]Zr-DFO-PAS$_{200}$-Fab	ImmunoPET	PET/CT imaging demonstrated highly selective and rapid accumulation (11.1 ± 1.7%ID/g) in orthotopic thyroid tumors, with strong contrast images achieved 24 h p.i.	The study was conducted in murine models, requiring further validation in human clinical trials to confirm efficacy and safety.	54	2019	Galectin-3
[^{89}Zr]Zr-Dfo-αGal3-Fab-PAS$_{200}$	ImmunoPET	[^{89}Zr]Zr-Dfo-αGal3-Fab-PAS$_{200}$ tracer is highly specific for Gal3, demonstrating rapid and selective accumulation in thyroid tumors (3.8 ± 0.9%ID/g).	The study was conducted in murine models, requiring further validation in human clinical trials to confirm efficacy and safety.	55	2021	Galectin-3

[^{64}Cu]Cu-NOTA-ALT-836-Fab	ImmunoPET	Tumor-to-muscle ratios were significantly higher in the positive group compared to the blocking and negative groups at all time points. [^{64}Cu]Cu-NOTA-ALT-836-Fab exhibited a tumor uptake of 5.1 ± 0.5%ID/g at 24 h p.i., demonstrating effective targeting of tissue factor in triple-negative breast cancer.	Compared to the full antibody, which may limit absolute tumor uptake and sensitivity in detecting low TF-expressing tumors	56	2015	TF
[^{64}Cu]Cu-NOTA-heterodimer	ImmunoPET	Dual targeting of TF and CD105 with a bispecific heterodimer significantly improves tumor localization and imaging specificity.	The study was conducted in animal models, necessitating further validation in human clinical trials.	57	2016	TF and CD105
[^{64}Cu]Cu-NOTA-heterodimer-ZW800	ImmunoPET	Labeling the heterodimer with ^{64}Cu for PET imaging and ZW800 for NIRF imaging to leverage the advantages of both modalities. [^{64}Cu]Cu-NOTA-heterodimer-ZW800 exhibited significantly higher tumor uptake (21.0 ± 3.4%ID/g) compared to its homodimer counterparts (7.6 ± 3.7%ID/g for ALT836 and 9.6 ± 2.0%ID/g for TRC105), suggesting enhanced targeting efficiency through dual-receptor targeting in pancreatic cancer.	The study was conducted in animal models, necessitating further validation in human clinical trials.	58	2017	TF and CD105
[^{89}Zr]Zr-DFO-Miltuximab-F(ab′)$_2$; [^{89}Zr]Zr-Miltuximab-Fab	ImmunoPET	[^{89}Zr]Zr-Miltuximab is an effective immuno-PET imaging agent for detecting GPC-1-positive tumors such as GBM. Tumor uptake in GBM xenografts was 5.7 ± 0.94%ID/g on day 9 p.i.	Further engineering of antibody fragments is needed to improve their pharmacokinetics and reduce off-target effects.	59	2023	Glypican-1
[^{89}Zr]Zr-αGPC3-F(ab′)$_2$	ImmunoPET	[^{89}Zr]Zr-αGPC3-F(ab′)$_2$ is a promising imaging agent for HCC, offering high tumor specificity, rapid blood clearance, and excellent imaging contrast. [^{89}Zr]Zr-αGPC3-F(ab′)$_2$ exhibited a tumor uptake of 100 ± 21%ID/g at 24 h p.i.	The study was conducted in animal models, necessitating further validation in human clinical trials.	60	2014	Glypican-3
[^{18}F]AlF-hMN-14-Fab [^{18}F]AlF-hMN-14-Fab-AD2 fragments	ImmunoPET	The [^{18}F]AlF-hMN-14-Fab (1.85 ± 0.36%ID/g) and [^{18}F]AlF-hMN-14-Fab-AD2 fragments (2.10 ± 0.46%ID/g) showed higher tumor-to-blood ratios compared to the diabody format, suggesting their superior imaging potential. [^{18}F]AlF-hMN-14-diabody showed the highest tumor uptake (4.61 ± 0.67%ID/g) at 4 h p.i. compared to the other antibody formats.	High liver and kidney uptake of the labeled fragments could interfere with imaging of tumors located in these regions.	13	2014	CEA
[^{124}I]I-5-F(ab′)$_2$	ImmunoPET	[^{124}I]I-5-F(ab′)$_2$ is an effective imaging agent for diagnosing gastric carcinoma. It demonstrated high specificity for hTREM2, rapid clearance from the bloodstream, significant tumor uptake, and excellent imaging contrast (8.5 ± 1.3%ID/g at 24 h).	The study's findings are based on preclinical models, and further research is needed to validate the results in human subjects.	10	2023	TREM2
[^{99m}Tc]Tc-MAG$_3$-5-F(ab′)$_2$; [^{99m}Tc]Tc-MAG$_3$-5-Fab	ImmunoSPECT	The probe showed clear tumor visualization with low non-tumor tissue uptake, indicating its potential for clinical applications in lung cancer imaging.	The study is based on preclinical models, and further validation in clinical settings is required.	61	2024	TREM2

(*continued on next page*)

Table 1 (*continued*)

Probe name	Imaging	Finding	Limitation	Ref.	Year	Targeting
[^{111}In]In-TNC Fab	ImmunoSPECT	The study concluded that [^{111}In]In-TNC Fab imaging effectively identifies inflammatory regions in the hearts of cynomolgus monkeys following MI. The imaging results correlated well with histological findings.	The resolution of SPECT imaging in small primate hearts may be lower than what can be achieved in human hearts, potentially limiting the precision of inflammation detection.	62	2016	TNC
[^{64}Cu]Cu-NOTA-denos-Fab	ImmunoPET	[^{64}Cu]Cu-NOTA-denos-Fab is an effective PET imaging agent for RANKL, providing faster blood clearance and better imaging contrast compared to the full-length antibody (2.72 ± 0.61%ID/mL).	The study primarily used a single xenograft model, necessitating further validation in additional models and clinical samples.	63	2022	RANKL
[^{99m}Tc]Tc-HYNIC-Fab (Tocilizumab)	ImmunoSPECT	^{99m}Tc- or Cy7-labeled Fab(Tocilizumab) fragments are effective imaging agents for detecting IL-6R expression in MM. [^{99m}Tc]Tc-HYNIC-Fab (Tocilizumab) demonstrated varying uptake in MM tumor models, with peak uptake values of 8.68 ± 0.67%ID/g and 6.92 ± 2.21%ID/g for U266 and MM1S tumors, respectively, indicating its potential as an imaging agent for IL-6R expression in myeloma tumors.	The study was conducted in a murine model, and further research is needed to validate the findings in human subjects.	64	2021	IL-6
[^{89}Zr]Zr-xiRA63; [^{89}Zr]Zr-ThioFab-xiRA63	ImmunoPET	[^{89}Zr]Zr-xiRA63 is a promising candidate for specifically targeting and imaging ETA-positive GBM.	The study was conducted in preclinical models, and further validation in human subjects is required.	65	2023	ETA
[^{89}Zr]Zr-DFO-anti-PV1 Bis3	ImmunoPET	High-affinity antibodies and their F(ab′)$_2$ fragments showed specific and prolonged retention in the kidneys, making them promising candidates for kidney-targeted drug delivery.	Focused primarily on the kidney and lung, with less emphasis on potential off-target effects in other organs expressing PV1.	66	2020	PV1
[^{124}I]I-PGN650	ImmunoPET	The first-in-human evaluation of [^{124}I]I-PGN650 demonstrated that the tracer is safe for PET imaging and has acceptable pharmacokinetics.	The observed tumor uptake in patients was lower than expected based on preclinical studies.	67	2017	PS
[^{89}Zr]Zr-DFO-HA-βG-Fab	ImmunoPET	[^{89}Zr]Zr-DFO-HA-βG-Fab is a promising tracer for non-invasive PET imaging of Aspergillus infections.	Some binding was observed in bacterial infections, indicating potential cross-reactivity and a need for further specificity improvement.	68	2024	β-glucans
[^{89}Zr]Zr-LA25	ImmunoPET	[^{89}Zr]Zr-LA25 is an effective PET radiotracer for non-invasive imaging of MAA-rich atherosclerotic lesions. [^{89}Zr]Zr-LA25 demonstrated a significantly higher uptake of 0.022 ± 0.003%ID/g in atherosclerotic rabbit aortas compared to controls, indicating its potential as a radiotracer for imaging atherosclerotic lesions.	The study used mouse and rabbit models, which may not fully replicate human atherosclerosis, necessitating further validation in clinical settings.	69	2018	MAA

[^{89}Zr]Zr-pro-MMP-9 F(ab′)$_2$	ImmunoPET	[^{89}Zr]Zr-pro-MMP-9 F(ab′)$_2$ effectively detect colitis-induced intestinal fibrosis and associated kidney fibrosis.	Further research is needed to validate the findings in human subjects.	19	2020	MMPs

AAA, abdominal aortic aneurysm; ETA, endothelin A receptor; GBM, glioblastoma multiforme; HNSCC, head and neck squamous cell carcinomas; IL-6, interleukin-6; MAA, malondialdehyde-acetaldehyde; MMPs, matrix metalloproteinases; MCPs, metal chelating polymers; MM, multiple myeloma; NSCLC, non-small cell lung cancer; p.i., post-injection; PS, phosphatidylserine; TBR, tumor-to-background ratios; TF, tissue factor; TREM2, triggering receptor expressed on myeloid cells 2; TNC, tenascin-C; RANKL, the receptor activator of nuclear factor kappa B ligand.

[a]Represents entering the clinical trial stage.

antibody drug development suggest that Fab and F(ab′)$_2$ fragments will play a central role in future cancer treatment and diagnostics.

7. Conclusions

In conclusion, while current observations are based on retrospective analyses, the pace of technological innovation within this field of imaging of Fab and F(ab′)$_2$ fragments is both rapid and ambitious. Efforts to adopt more precise and site-specific conjugation chemistries are in progress, alongside the development of theranostic Fab and F(ab′)$_2$ fragments. These advancements aim to harness complementary radionuclide pairs for simultaneous imaging and therapy. ImmunoPET/SPECT imaging utilizing Fab and F(ab′)$_2$ fragments, has emerged as a valuable diagnostic adjunct, showing significant potential to enhance clinical management in the context of cancer. With these ongoing developments, a relatively swift progression toward clinical application is anticipated. Furthermore, immunoPET/SPECT imaging is expected to play a crucial role in evaluating the expanding realm of fragment-based antibody drug conjugates (ADCs), contributing to their refinement and efficacy in therapeutic settings.

Acknowledgments

This work was supported by the University of Wisconsin − Madison and the National Institutes of Health (P30 CA014520 & T32 CA009206, USA), the National Natural Science Foundation of China (82472018, 82171970), Beijing Nova Program (20240484725), Beijing Municipal Science & Technology Commission (Z221100007422027, China), National Key Research and Development Program of China (2024YFE0113500), National High Level Hospital Clinical Research Funding (Interdisciplinary Research Project of Peking University First Hospital, 2023IR17, 2024IR07; Scientific and Technological Achievements Transformation Incubation Guidance Fund Project of Peking University First Hospital, 2024CX18, China).

Author contributions

Wenpeng Huang, Jingwei Zhou, Yanchen Liu: Conceptualization, Formal analysis, Writing − original draft, Writing − review & editing, Visualization. Yihan Yang: Resources. Rachel J. Saladin: Resources. Jessica C. Hsu: Funding acquisition, Writing − review & editing. Lei Kang: Funding acquisition, Writing − review & editing. Weibo Cai: Funding acquisition, Writing − review & editing. All of the authors have read and approved the final manuscript.

Conflicts of interest

Weibo Cai declares conflict of interest with the following corporations: Portrai, Inc., rTR Technovation Corporation, Four Health Global Pharmaceuticals Inc. All other authors declare no conflict of interest.

References

1. Siegel RL, Giaquinto AN, Jemal A. Cancer statistics, 2024. *CA Cancer J Clin* 2024;**74**:12−49.

2. Cortez-Retamozo V, Backmann N, Senter PD, Wernery U, De Baetselier P, Muyldermans S, et al. Efficient cancer therapy with a nanobody-based conjugate. *Cancer Res* 2004;**64**:2853−7.
3. Mankoff DA. A definition of molecular imaging. *J Nucl Med* 2007; **48**:18−21N.
4. Shao F, Pan Z, Long Y, Zhu Z, Wang K, Ji H, et al. Nectin-4-targeted immunoSPECT/CT imaging and photothermal therapy of triple-negative breast cancer. *J Nanobiotechnol* 2022;**20**:243.
5. Badier L, Quelven I. Zirconium 89 and copper 64 for immunoPET: from antibody bioconjugation and radiolabeling to molecular imaging. *Pharmaceutics* 2024;**16**:882.
6. Wei W, Rosenkrans ZT, Liu J, Huang G, Luo QY, Cai W. ImmunoPET: concept, design, and applications. *Chem Rev* 2020;**120**: 3787−851.
7. Fu R, Carroll L, Yahioglu G, Aboagye EO, Miller PW. Antibody fragment and affibody immunoPET imaging agents: radiolabelling strategies and applications. *ChemMedChem* 2018;**13**:2466−78.
8. He XX, Du S, Gao SQ, Chen JY, Cao RJ, Xing ZK, et al. Humanization of fibroblast growth factor 1 single-chain antibody and validation for its antitumorigenic efficacy in breast cancer and glioma cells. *J Cell Mol Med* 2018;**22**:3259−63.
9. Hirasawa S, Kitahara Y, Okamatsu Y, Fujii T, Nakayama A, Ueno S, et al. Facile and efficient chemoenzymatic semisynthesis of Fc-Fusion compounds for half-life extension of pharmaceutical components. *Bioconjug Chem* 2019;**30**:2323−31.
10. Shi D, Xu Z, Cheng Y, Lin Q, Si Z, Fu W, et al. ^{124}I-Labeled immuno-PET targeting hTREM2 for the diagnosis of gastric carcinoma. *Mol Pharm* 2023;**20**:2235−44.
11. Mendler CT, Gehring T, Wester HJ, Schwaiger M, Skerra A. ^{89}Zr-labeled *versus* ^{124}I-labeled αHER2 Fab with optimized plasma half-life for high-contrast tumor imaging *in vivo*. *J Nucl Med* 2015;**56**: 1112−8.
12. Ghani S, Deravi N, Pirzadeh M, Rafiee B, Gatabi ZR, Bandehpour M, et al. Antibody fragment and targeted colorectal cancer therapy: a global systematic review. *Curr Pharm Biotechnol* 2022;**23**:1061−71.
13. Lütje S, Franssen GM, Sharkey RM, Laverman P, Rossi EA, Goldenberg DM, et al. Anti-CEA antibody fragments labeled with [^{18}F]AlF for PET imaging of CEA-expressing tumors. *Bioconjug Chem* 2014;**25**:335−41.
14. Turker NS, Heidari P, Kucherlapati R, Kucherlapati M, Mahmood U. An EGFR targeted PET imaging probe for the detection of colonic adenocarcinomas in the setting of colitis. *Theranostics* 2014;**4**: 893−903.
15. Suman SK, Kameswaran M, Pandey U, Sarma HD, Dash A. Preparation and preliminary bioevaluation studies of ^{68}Ga-NOTA-rituximab fragments as radioimmunoscintigraphic agents for non-Hodgkin lymphoma. *J Label Compd Radiopharm* 2019;**62**:850−9.
16. Wu AM. Antibodies and antimatter: the resurgence of immuno-PET. *J Nucl Med* 2009;**50**:2−5.
17. De Vos J, Devoogdt N, Lahoutte T, Muyldermans S. Camelid single-domain antibody-fragment engineering for (pre)clinical *in vivo* molecular imaging applications: adjusting the bullet to its target. *Expet Opin Biol Ther* 2013;**13**:1149−60.
18. Zhao X, Ning Q, Mo Z, Tang S. A promising cancer diagnosis and treatment strategy: targeted cancer therapy and imaging based on antibody fragment. *Artif Cells, Nanomed Biotechnol* 2019;**47**: 3621−30.
19. Dmochowska N, Tieu W, Keller MD, Hollis CA, Campaniello MA, Mavrangelos C, et al. ^{89}Zr-pro-MMP-9 F(ab′)$_2$ detects colitis induced intestinal and kidney fibrosis. *Sci Rep* 2020;**10**:20372.
20. Chakravarty R, Goel S, Valdovinos HF, Hernandez R, Hong H, Nickles RJ, et al. Matching the decay half-life with the biological half-life: immunoPET imaging with ^{44}Sc-labeled cetuximab Fab fragment. *Bioconjug Chem* 2014;**25**:2197−204.
21. Chakravarty R, Rohra N, Jadhav S, Sarma HD, Jain R, Chakraborty S. Biochemical separation of Cetuximab-Fab from papain-digested antibody fragments and radiolabeling with ^{64}Cu for potential use in radioimmunotheranostics. *Appl Radiat Isot* 2023; **196**:110795.
22. Lu W, Cong Y, Yang D, Chen D, Yang G, Wang Y, et al. Engineered antibody fragment against the urokinase plasminogen activator for fast delineation of triple-negative breast cancer by positron emission tomography. *Mol Pharm* 2021;**18**:1690−8.
23. Ku A, Kondo M, Cai Z, Meens J, Li MR, Ailles L, et al. Dose predictions for [^{177}Lu]Lu-DOTA-panitumumab F(ab′)$_2$ in NRG mice with HNSCC patient-derived tumour xenografts based on [^{64}Cu]Cu-DOTA-panitumumab F(ab′)$_2$-implications for a PET theranostic strategy. *EJNMMI Radiopharm Chem* 2021;**6**:25.
24. Lu Y, Boyle AJ, Cao PJ, Hedley D, Reilly RM, Winnik MA. EGFR-targeted metal chelating polymers (MCPs) harboring multiple pendant PEG2K chains for microPET/CT imaging of patient-derived pancreatic cancer xenografts. *ACS Biomater Sci Eng* 2017;**3**:279−90.
25. Shi D, Zhang Y, Xu Z, Si Z, Cheng Y, Cheng D, et al. Noninvasive evaluation of EGFR expression of digestive tumors using ^{99m}Tc-MAG3-Cet-F(ab′)$_2$-based SPECT/CT Imaging. *Mol Imaging* 2022; **2022**:3748315.
26. Bellaye PS, Moreau M, Raguin O, Oudot A, Bernhard C, Vrigneaud JM, et al. Radiolabeled F(ab′)$_2$-cetuximab for theranostic purposes in colorectal and skin tumor-bearing mice models. *Clin Transl Oncol* 2018;**20**:1557−70.
27. Boyle AJ, Cao PJ, Hedley DW, Sidhu SS, Winnik MA, Reilly RM. MicroPET/CT imaging of patient-derived pancreatic cancer xenografts implanted subcutaneously or orthotopically in NOD-scid mice using ^{64}Cu-NOTA-panitumumab F(ab′)$_2$ fragments. *Nucl Med Biol* 2015;**42**:71−7.
28. Suman SK, Mukherjee A, Pandey U, Chakraborty A, Rakshit S, Tawate M, et al. ^{68}Ga-labeled trastuzumab fragments for immuno-PET imaging of human epidermal growth factor receptor 2 expression in solid cancers. *Cancer Biother Radiopharm* 2023;**38**:38−50.
29. Rathore Y, Shukla J, Laroiya I, Deep A, Lakhanpal T, Kumar R, et al. Development ^{68}Ga trastuzumab Fab and bioevaluation by PET imaging in HER2/neu expressing breast cancer patients. *Nucl Med Commun* 2022;**43**:458−67.
30. Lam K, Chan C, Reilly RM. Development and preclinical studies of ^{64}Cu-NOTA-pertuzumab F(ab′)$_2$ for imaging changes in tumor HER2 expression associated with response to trastuzumab by PET/CT. *mAbs* 2017;**9**:154−64.
31. Kwon LY, Scollard DA, Reilly RM. ^{64}Cu-labeled trastuzumab Fab-PEG$_{24}$-EGF radioimmunoconjugates bispecific for HER2 and EGFR: pharmacokinetics, biodistribution, and tumor imaging by PET in comparison to monospecific agents. *Mol Pharm* 2017;**14**: 492−501.
32. Richter A, Knorr K, Schlapschy M, Robu S, Morath V, Mendler C, et al. First in-human medical imaging with a PASylated ^{89}Zr-labeled anti-HER2 Fab-fragment in a patient with metastatic breast cancer. *Nucl Med Mol Imag* 2020;**54**:114−9.
33. Facca VJ, Al-Saden N, Ku A, Reilly RM. Imaging of HER2-positive tumors in NOD/SCID mice with pertuzumab Fab-hexahistidine peptide immunoconjugates labeled with [^{99m}Tc]-(I)-tricarbonyl complex. *Mol Imag Biol* 2021;**23**:495−504.
34. Kang L, Li C, Rosenkrans ZT, Engle JW, Wang R, Jiang D, et al. Noninvasive evaluation of CD20 expression using ^{64}Cu-Labeled F(ab′)$_2$ Fragments of obinutuzumab in lymphoma. *J Nucl Med* 2021; **62**:372−8.
35. Kang L, Li C, Yang Q, Sutherlin L, Wang L, Chen Z, et al. ^{64}Cu-labeled daratumumab F(ab′)$_2$ fragment enables early visualization of CD38-positive lymphoma. *Eur J Nucl Med Mol Imag* 2022;**49**: 1470−81.
36. Haylock AK, Spiegelberg D, Nilvebrant J, Sandström K, Nestor M. *In vivo* characterization of the novel CD44v6-targeting Fab fragment AbD15179 for molecular imaging of squamous cell carcinoma: a dual-isotope study. *EJNMMI Res* 2014;**4**:11.
37. Haylock AK, Spiegelberg D, Mortensen AC, Selvaraju RK, Nilvebrant J, Eriksson O, et al. Evaluation of a novel type of imaging probe based on a recombinant bivalent mini-antibody construct for

detection of CD44v6-expressing squamous cell carcinoma. *Int J Oncol* 2016;**48**:461−70.
38. Fan X, Ważyńska MA, Kol A, Perujo Holland N, Fernandes B, van Duijnhoven SMJ, et al. Development of [^{89}Zr]Zr-hCD103.Fab01A and [^{68}Ga]Ga-hCD103.Fab01A for PET imaging to noninvasively assess cancer reactive T cell infiltration: Fab-based CD103 immunoPET. *EJNMMI Res* 2023;**13**:100.
39. Chen F, Nayak TR, Goel S, Valdovinos HF, Hong H, Theuer CP, et al. *In vivo* tumor vasculature targeted PET/NIRF imaging with TRC105 (Fab)-conjugated, dual-labeled mesoporous silica nanoparticles. *Mol Pharm* 2014;**11**:4007−14.
40. Shi S, Orbay H, Yang Y, Graves SA, Nayak TR, Hong H, et al. PET imaging of abdominal aortic aneurysm with ^{64}Cu-labeled anti-CD105 antibody Fab fragment. *J Nucl Med* 2015;**56**:927−32.
41. Luo H, Hernandez R, Hong H, Graves SA, Yang Y, England CG, et al. Noninvasive brain cancer imaging with a bispecific antibody fragment, generated *via* click chemistry. *Proc Natl Acad Sci U S A* 2015;**112**:12806−11.
42. Bridgwater C, Geller A, Hu X, Burlison JA, Zhang HG, Yan J, et al. ^{89}Zr-Labeled anti-PD-L1 antibody fragment for evaluating *in vivo* PD-L1 levels in melanoma mouse model. *Cancer Biother Radiopharm* 2020;**35**:549−57.
43. Cheng Y, Shi D, Xu Z, Gao Z, Si Z, Zhao Y, et al. ^{124}I-labeled monoclonal antibody and fragment for the noninvasive evaluation of tumor PD-L1 expression *in vivo*. *Mol Pharm* 2022;**19**:3551−62.
44. Cheng Y, Shi D, Ye R, Fu W, Ma P, Si Z, et al. Noninvasive evaluation of PD-L1 expression in non-small cell lung cancer by immunoPET imaging using an acylating agent-modified antibody fragment. *Eur J Nucl Med Mol Imag* 2023;**50**:1585−96.
45. Bouleau A, Nozach H, Dubois S, Kereselidze D, Chevaleyre C, Wang CI, et al. Optimizing immuno-PET imaging of tumor PD-L1 expression: pharmacokinetic, biodistribution, and dosimetric comparisons of ^{89}Zr-labeled anti-PD-L1 antibody formats. *J Nucl Med* 2022;**63**:1259−65.
46. Tran VL, Bouleau A, Nozach H, Richard M, Chevaleyre C, Dubois S, et al. Impact of radiolabeling strategies on the pharmacokinetics and distribution of an anti-PD-L1 PET ligand. *Mol Pharm* 2022;**19**:3673−80.
47. Bao R, Wang Y, Lai J, Zhu H, Zhao Y, Li S, et al. Enhancing anti-PD-1/PD-L1 immune checkpoint inhibitory cancer therapy by CD276-targeted photodynamic ablation of tumor cells and tumor vasculature. *Mol Pharm* 2019;**16**:339−48.
48. Ehlerding EB, Lee HJ, Jiang D, Ferreira CA, Zahm CD, Huang P, et al. Antibody and fragment-based PET imaging of CTLA-4$^+$ T-cells in humanized mouse models. *Am J Cancer Res* 2019;**9**:53−63.
49. Clausen AS, Christensen C, Christensen E, Cold S, Kristensen LK, Hansen AE, et al. Development of a ^{64}Cu-labeled CD4$^+$ T cell targeting PET tracer: evaluation of CD4 specificity and its potential use in collagen-induced arthritis. *EJNMMI Res* 2022;**12**:62.
50. Kristensen LK, Christensen C, Alfsen MZ, Cold S, Nielsen CH, Kjaer A. Monitoring CD8a$^+$ T cell responses to radiotherapy and CTLA-4 blockade using [^{64}Cu]NOTA-CD8a PET imaging. *Mol Imag Biol* 2020;**22**:1021−30.
51. Ilovich O, Natarajan A, Hori S, Sathirachinda A, Kimura R, Srinivasan A, et al. Development and validation of an immuno-PET tracer as a companion diagnostic agent for antibody-drug conjugate therapy to target the CA6 epitope. *Radiology* 2015;**276**:191−8.
52. Roll W, Müther M, Böning G, Delker A, Warneke N, Gildehaus FJ, et al. First clinical experience with fractionated intracavitary radioimmunotherapy using [^{177}Lu]Lu-6A10-Fab fragments in patients with glioblastoma: a pilot study. *EJNMMI Res* 2023;**13**:78.
53. De Rose F, Braeuer M, Braesch-Andersen S, Otto AM, Steiger K, Reder S, et al. Galectin-3 targeting in thyroid orthotopic tumors opens new ways to characterize thyroid cancer. *J Nucl Med* 2019;**60**:770−6.
54. Peplau E, De Rose F, Reder S, Mittelhäuser M, Scafetta G, Schwaiger M, et al. Development of a chimeric antigen-binding fragment directed against human galectin-3 and validation as an immuno-positron emission tomography tracer for the sensitive *in vivo* imaging of thyroid cancer. *Thyroid* 2020;**30**:1314−26.
55. Peplau E, De Rose F, Eichinger A, Reder S, Mittelhäuser M, Scafetta G, et al. Effective rational humanization of a PASylated anti-galectin-3 Fab for the sensitive PET imaging of thyroid cancer *in vivo*. *Sci Rep* 2021;**11**:7358.
56. Shi S, Hong H, Orbay H, Graves SA, Yang Y, Ohman JD, et al. ImmunoPET of tissue factor expression in triple-negative breast cancer with a radiolabeled antibody Fab fragment. *Eur J Nucl Med Mol Imag* 2015;**42**:1295−303.
57. Luo H, England CG, Shi S, Graves SA, Hernandez R, Liu B, et al. Dual targeting of tissue factor and CD105 for preclinical PET imaging of pancreatic cancer. *Clin Cancer Res* 2016;**22**:3821−30.
58. Luo H, England CG, Goel S, Graves SA, Ai F, Liu B, et al. ImmunoPET and near-infrared fluorescence imaging of pancreatic cancer with a dual-labeled bispecific antibody fragment. *Mol Pharm* 2017;**14**:1646−55.
59. Ghosh S, Fletcher NL, Huda P, Houston ZH, Howard CB, Lund ME, et al. Pharmacokinetics and biodistribution of ^{89}Zr-Miltuximab and its antibody fragments as glypican-1 targeting immuno-PET agents in glioblastoma. *Mol Pharm* 2023;**20**:1549−63.
60. Sham JG, Kievit FM, Grierson JR, Chiarelli PA, Miyaoka RS, Zhang M, et al. Glypican-3-targeting F(ab′)$_2$ for ^{89}Zr PET of hepatocellular carcinoma. *J Nucl Med* 2014;**55**:2032−7.
61. Shi D, Fu W, Tan H, Lin Q, Shi H, Cheng D. Preclinical evaluation of ^{99m}Tc-MAG3-5-Fab targeting TREM2 in lung cancer mouse models: a comparison with ^{99m}Tc-MAG3-5-F(ab′)$_2$. *Mol Pharm* 2024;**21**:303−12.
62. Ageyama N, Kurosawa H, Fujimoto O, Uehara T, Hiroe M, Arano Y, et al. Successful inflammation imaging of non-human primate hearts using an antibody specific for tenascin-C. *Int Heart J* 2019;**60**:151−8.
63. Dewulf J, Hrynchak I, Geudens S, Pintelon I, Vangestel C, Sereno J, et al. Improved characteristics of RANKL immuno-PET imaging using radiolabeled antibody Fab fragments. *Pharmaceutics* 2022;**14**:939.
64. Camacho X, Perroni C, Machado CL, de Godoi Carneiro C, de Souza Junqueira M, Faria D, et al. 99mTechnetium- or Cy7-labeled Fab (Tocilizumab) as potential multiple myeloma imaging agents. *Anti Cancer Agents Med Chem* 2021;**21**:1883−93.
65. Hautiere M, Vivier D, Pineau D, Denis C, Kereselidze D, Herbet A, et al. ImmunoPET imaging-based pharmacokinetic profiles of an antibody and its Fab targeting endothelin A receptors on glioblastoma stem cells in a preclinical orthotopic model. *Eur J Nucl Med Mol Imag* 2023;**50**:3192−201.
66. Li Q, Peterson N, Hanna RN, Kuszpit K, White J, Allen KL, et al. Antibody fragment F(ab′)$_2$ targeting caveolae-associated protein PV1 for selective kidney targeting and retention. *Mol Pharm* 2020;**17**:507−16.
67. Laforest R, Dehdashti F, Liu Y, Frye J, Frye S, Luehmann H, et al. First-in-man evaluation of ^{124}I-PGN650: a PET tracer for detecting phosphatidylserine as a biomarker of the solid tumor microenvironment. *Mol Imaging* 2017;**16**:1536012117733349.
68. Lai J, Shah S, Martinez-Orengo N, Knight R, Alemu E, Turner ML, et al. PET imaging of aspergillus infection using Zirconium-89 labeled anti-β-glucan antibody fragments. *Eur J Nucl Med Mol Imag* 2024;**51**:3223−34.
69. Senders ML, Que X, Cho YS, Yeang C, Groenen H, Fay F, et al. PET/MR imaging of malondialdehyde-acetaldehyde epitopes with a human antibody detects clinically relevant atherothrombosis. *J Am Coll Cardiol* 2018;**71**:321−35.
70. Andersen DC, Reilly DE. Production technologies for monoclonal antibodies and their fragments. *Curr Opin Biotechnol* 2004;**15**:456−62.
71. Zettlitz KA, Tavaré R, Tsai W-TK, Yamada RE, Ha NS, Collins J, et al. ^{18}F-labeled anti-human CD20 cys-diabody for same-day immunoPET in a model of aggressive B cell lymphoma in human CD20 transgenic mice. *Eur J Nucl Med Mol Imag* 2019;**46**:489−500.

72. Wingler LM, McMahon C, Staus DP, Lefkowitz RJ, Kruse AC. Distinctive activation mechanism for angiotensin receptor revealed by a synthetic nanobody. *Cell* 2019;**176**:479−490.e12.
73. Li C, Wang Y, Liu T, Niklasch M, Qiao K, Durand S, et al. An *E. coli*-produced single-chain variable fragment (scFv) targeting hepatitis B virus surface protein potently inhibited virion secretion. *Antivir Res* 2019;**162**:118−29.
74. Xavier S, Gopi Mohan C, Nair S, Menon KN, Vijayachandran LS. Generation of humanized single-chain fragment variable immunotherapeutic against EGFR variant III using baculovirus expression system and *in vitro* validation. *Int J Biol Macromol* 2019;**124**:17−24.
75. Nelson AL, Reichert JM. Development trends for therapeutic antibody fragments. *Nat Biotechnol* 2009;**27**:331−7.
76. Rafiq S, Yeku OO, Jackson HJ, Purdon TJ, van Leeuwen DG, Drakes DJ, et al. Targeted delivery of a PD-1-blocking scFv by CAR-T cells enhances anti-tumor efficacy *in vivo*. *Nat Biotechnol* 2018;**36**:847−56.
77. Rabenhold M, Steiniger F, Fahr A, Kontermann RE, Rüger R. Bispecific single-chain diabody-immunoliposomes targeting endoglin (CD105) and fibroblast activation protein (FAP) simultaneously. *J Control Release* 2015;**201**:56−67.
78. Yang W, Hu Q, Xu Y, Liu H, Zhong L. Antibody fragment-conjugated gemcitabine and paclitaxel-based liposome for effective therapeutic efficacy in pancreatic cancer. *Mater Sci Eng C* 2018;**89**:328−35.
79. Kim M, Pyo S, Kang CH, Lee CO, Lee HK, Choi SU, et al. Folate receptor 1 (FOLR1) targeted chimeric antigen receptor (CAR) T cells for the treatment of gastric cancer. *PLoS One* 2018;**13**:e0198347.
80. Liu W, Zhao W, Bai X, Jin S, Li Y, Qiu C, et al. High antitumor activity of sortase A-generated anti-CD20 antibody fragment drug conjugates. *Eur J Pharmaceut Sci* 2019;**134**:81−92.
81. Volz J, Mammadova-Bach E, Gil-Pulido J, Nandigama R, Remer K, Sorokin L, et al. Inhibition of platelet GPVI induces intratumor hemorrhage and increases efficacy of chemotherapy in mice. *Blood* 2019;**133**:2696−706.
82. Bensimon C, Redshaw R. Antibody radiolabeling. In: Shire SJ, Gombotz W, Bechtold-Peters K, Andya J, editors. *Current trends in monoclonal antibody development and manufacturing*. New York, NY: Springer; 2010. p. 323−44.
83. Chomet M, van Dongen GAMS, Vugts DJ. State of the art in radiolabeling of antibodies with common and uncommon radiometals for preclinical and clinical immuno-PET. *Bioconjug Chem* 2021;**32**:1315−30.
84. Page RL, Garg PK, Vaidyanathan G, Zalutsky MR. Preclinical evaluation and PET imaging of ^{18}F-labeled Mel-14 F(ab′)$_2$ fragment in normal dogs. *Nucl Med Biol* 1994;**21**:911−9.
85. Otsuka FL, Welch MJ, Kilbourn MR, Dence CS, Dilley WG, Wells SA. Antibody fragments labeled with fluorine-18 and gallium-68: *in vivo* comparison with indium-111 and iodine-125-labeled fragments. *Int J Rad Appl Instrum B* 1991;**18**:813−6.
86. McBride WJ, Sharkey RM, Karacay H, D'Souza CA, Rossi EA, Laverman P, et al. A novel method of ^{18}F radiolabeling for PET. *J Nucl Med* 2009;**50**:991−8.
87. Drake CR, Sevillano N, Truillet C, Craik CS, VanBrocklin HF, Evans MJ. Site-specific radiofluorination of biomolecules with 8-[^{18}F]-fluorooctanoic acid catalyzed by lipoic acid ligase. *ACS Chem Biol* 2016;**11**:1587−94.
88. Oliveira BL, Guo Z, Bernardes GJL. Inverse electron demand Diels−Alder reactions in chemical biology. *Chem Soc Rev* 2017;**46**:4895−950.
89. Meyer JP, Adumeau P, Lewis JS, Zeglis BM. Click chemistry and radiochemistry: the first 10 years. *Bioconjug Chem* 2016;**27**:2791−807.
90. Yoshida C, Sogawa C, Tsuji AB, Sudo H, Sugyo A, Uehara T, et al. Development of positron emission tomography imaging by ^{64}Cu-labeled Fab for detecting ERC/mesothelin in a mesothelioma mouse model. *Nucl Med Commun* 2010;**31**:380−8.
91. Yoshida C, Tsuji AB, Sudo H, Sugyo A, Sogawa C, Inubushi M, et al. Development of positron emission tomography probe of ^{64}Cu-labeled anti-C-kit 12A8 Fab to measure protooncogene C-kit expression. *Nucl Med Biol* 2011;**38**:331−7.
92. Dearling JLJ, Voss SD, Dunning P, Snay E, Fahey F, Smith SV, et al. Imaging cancer using PET−the effect of the bifunctional chelator on the biodistribution of a ^{64}Cu-labeled antibody. *Nucl Med Biol* 2011;**38**:29−38.
93. Zhang Y, Hong H, Engle JW, Bean J, Yang Y, Leigh BR, et al. Positron emission tomography imaging of CD105 expression with a ^{64}Cu-labeled monoclonal antibody: NOTA is superior to DOTA. *PLoS One* 2011;**6**:e28005.
94. Heskamp S, Raavé R, Boerman O, Rijpkema M, Goncalves V, Denat F. ^{89}Zr-immuno-positron emission tomography in oncology: state-of-the-art ^{89}Zr Radiochemistry. *Bioconjug Chem* 2017;**28**:2211−23.
95. Price TW, Greenman J, Stasiuk GJ. Current advances in ligand design for inorganic positron emission tomography tracers ^{68}Ga, ^{64}Cu, ^{89}Zr and ^{44}Sc. *Dalton Trans* 2016;**45**:15702−24.
96. Hernandez R, Valdovinos HF, Yang Y, Chakravarty R, Hong H, Barnhart TE, et al. ^{44}Sc: an attractive isotope for peptide-based PET imaging. *Mol Pharm* 2014;**11**:2954−61.
97. van der Meulen NP, Bunka M, Domnanich KA, Müller C, Haller S, Vermeulen C, et al. Cyclotron production of ^{44}Sc: from bench to bedside. *Nucl Med Biol* 2015;**42**:745−51.
98. Kerdjoudj R, Pniok M, Alliot C, Kubíček V, Havlíčková J, Rösch F, et al. Scandium(III) complexes of monophosphorus acid DOTA analogues: a thermodynamic and radiolabelling study with ^{44}Sc from cyclotron and from a ^{44}Ti/^{44}Sc generator. *Dalton Trans* 2016;**45**:1398−409.
99. Luo J, Solimini NL, Elledge SJ. Principles of cancer therapy: oncogene and non-oncogene addiction. *Cell* 2009;**136**:823−37.
100. Saraon P, Pathmanathan S, Snider J, Lyakisheva A, Wong V, Stagljar I. Receptor tyrosine kinases and cancer: oncogenic mechanisms and therapeutic approaches. *Oncogene* 2021;**40**:4079−93.
101. Zhang X, Simons M. Receptor tyrosine kinases endocytosis in endothelium: biology and signaling. *Arterioscler Thromb Vasc Biol* 2014;**34**:1831−7.
102. Zhang Y. Targeting epidermal growth factor receptor for cancer treatment: abolishing both kinase-dependent and kinase-independent functions of the receptor. *Pharmacol Rev* 2023;**75**:1218−32.
103. Ma T, Sun X, Cui L, Gao L, Wu Y, Liu H, et al. Molecular imaging reveals trastuzumab-induced epidermal growth factor receptor downregulation *in vivo*. *J Nucl Med* 2014;**55**:1002−7.
104. Boyle AJ, Cao PJ, Cai Z, Chan C, Hedley DW, Reilly RM. Radioimmunotherapy of human pancreatic cancer xenografts in NOD-scid mice with [^{64}Cu]Cu-NOTA-panitumumab F(ab′)$_2$ alone or combined with radiosensitizing gemcitabine and the PARP inhibitor, rucaparib. *Nucl Med Biol* 2020;**84**−**85**:46−54.
105. Schlapschy M, Binder U, Börger C, Theobald I, Wachinger K, Kisling S, et al. PASylation: a biological alternative to PEGylation for extending the plasma half-life of pharmaceutically active proteins. *Protein Eng Des Sel* 2013;**26**:489−501.
106. Mendler CT, Friedrich L, Laitinen I, Schlapschy M, Schwaiger M, Wester HJ, et al. High contrast tumor imaging with radio-labeled antibody Fab fragments tailored for optimized pharmacokinetics *via* PASylation. *mAbs* 2015;**7**:96−109.
107. Pavlasova G, Mraz M. The regulation and function of CD20: an "enigma" of B-cell biology and targeted therapy. *Haematologica (Roma)* 2020;**105**:1494−506.
108. Gozzetti A, Ciofini S, Simoncelli M, Santoni A, Pacelli P, Raspadori D, et al. Anti CD38 monoclonal antibodies for multiple myeloma treatment. *Hum Vaccines Immunother* 2022;**18**:2052658.
109. Ma L, Dong L, Chang P. CD44v6 engages in colorectal cancer progression. *Cell Death Dis* 2019;**10**:30.

110. Anz D, Mueller W, Golic M, Kunz WG, Rapp M, Koelzer VH, et al. CD103 is a hallmark of tumor-infiltrating regulatory T cells. *Int J Cancer* 2011;**129**:2417−26.
111. Karzai FH, Apolo AB, Cao L, Madan RA, Adelberg DE, Parnes H, et al. A phase I study of TRC105 anti-endoglin (CD105) antibody in metastatic castration-resistant prostate cancer. *BJU Int* 2015;**116**: 546−55.
112. Zhang Y, Zhang Z. The history and advances in cancer immunotherapy: understanding the characteristics of tumor-infiltrating immune cells and their therapeutic implications. *Cell Mol Immunol* 2020;**17**:807−21.
113. Nimmagadda S. Quantifying PD-L1 expression to monitor immune checkpoint therapy: opportunities and challenges. *Cancers (Basel)* 2020;**12**:3173.
114. Berghmans E, Jacobs J, Deben C, Hermans C, Broeckx G, Smits E, et al. Mass spectrometry imaging reveals neutrophil defensins as additional biomarkers for anti-PD-(L)1 immunotherapy response in NSCLC patients. *Cancers (Basel)* 2020;**12**:863.
115. Wu S, Hu C, Hui K, Jiang X. Non-immune functions of B7-H3: bridging tumor cells and the tumor vasculature. *Front Oncol* 2024;**14**: 1408051.
116. Hossen MM, Ma Y, Yin Z, Xia Y, Du J, Huang JY, et al. Current understanding of CTLA-4: from mechanism to autoimmune diseases. *Front Immunol* 2023;**14**:1198365.
117. Takeuchi A, Saito T. CD4 CTL, a cytotoxic subset of $CD4^+$ T cells, their differentiation and function. *Front Immunol* 2017;**8**:194.
118. Kearse KP, Smith NL, Semer DA, Eagles L, Finley JL, Kazmierczak S, et al. Monoclonal antibody DS6 detects a tumor-associated sialoglycotope expressed on human serous ovarian carcinomas. *Int J Cancer* 2000;**88**:866−72.
119. Lopus M, Oroudjev E, Wilson L, Wilhelm S, Widdison W, Chari R, et al. Maytansine and cellular metabolites of antibody-maytansinoid conjugates strongly suppress microtubule dynamics by binding to microtubules. *Mol Cancer Therapeut* 2010;**9**:2689−99.
120. Gondi G, Mysliwietz J, Hulikova A, Jen JP, Swietach P, Kremmer E, et al. Antitumor efficacy of a monoclonal antibody that inhibits the activity of cancer-associated carbonic anhydrase XII. *Cancer Res* 2013;**73**:6494−503.
121. Fiedler L, Kellner M, Oos R, Böning G, Ziegler S, Bartenstein P, et al. Fully automated production and characterization of ^{64}Cu and proof-of-principle small-animal PET imaging using ^{64}Cu-labelled CA XII targeting 6A10 Fab. *ChemMedChem* 2018;**13**:1230−7.
122. Li J, Vasilyeva E, Wiseman SM. Beyond immunohistochemistry and immunocytochemistry: a current perspective on galectin-3 and thyroid cancer. *Expert Rev Anticancer Ther* 2019;**19**:1017−27.
123. Song L, Tang J, Owusu L, Sun MZ, Wu J, Zhang J. Galectin-3 in cancer. *Clin Chim Acta* 2014;**431**:185−91.
124. Ren Z, Xue Y, Liu L, Zhang X, Pei J, Zhang Y, et al. Tissue factor overexpression in triple-negative breast cancer promotes immune evasion by impeding T-cell infiltration and effector function. *Cancer Lett* 2023;**565**:216221.
125. Saito T, Sugiyama K, Hama S, Yamasaki F, Takayasu T, Nosaka R, et al. High expression of glypican-1 predicts dissemination and poor prognosis in glioblastomas. *World Neurosurg* 2017;**105**: 282−8.
126. Omuro A, DeAngelis LM. Glioblastoma and other malignant gliomas: a clinical review. *JAMA* 2013;**310**:1842−50.
127. Zhou F, Shang W, Yu X, Tian J. Glypican-3: a promising biomarker for hepatocellular carcinoma diagnosis and treatment. *Med Res Rev* 2018;**38**:741−67.
128. Lei J, Wu L, Zhang N, Liu X, Zhang J, Kuang L, et al. Carcinoembryonic antigen potentiates non-small cell lung cancer progression *via* PKA−PGC-1α axis. *Mol Biomed* 2024;**5**:19.
129. Richard M, Martin Aubert S, Denis C, Dubois S, Nozach H, Truillet C, et al. Fluorine-18 and radiometal labeling of biomolecules *via* disulfide Rebridging. *Bioconjug Chem* 2023;**34**:2123−32.
130. Molgora M, Liu YA, Colonna M, Cella M. TREM2: a new player in the tumor microenvironment. *Semin Immunol* 2023;**67**:101739.
131. Imanaka-Yoshida K. Tenascin-C in heart diseases-the role of inflammation. *Int J Mol Sci* 2021;**22**:5828.
132. Boyce BF, Xing L. The RANKL/RANK/OPG pathway. *Curr Osteoporos Rep* 2007;**5**:98−104.
133. Ridker PM, Rane M. Interleukin-6 signaling and anti-interleukin-6 therapeutics in cardiovascular disease. *Circ Res* 2021;**128**:1728−46.
134. Bowman RL, Wang Q, Carro A, Verhaak RGW, Squatrito M. GlioVis data portal for visualization and analysis of brain tumor expression datasets. *Neuro Oncol* 2017;**19**:139−41.
135. Vasaikar S, Tsipras G, Landázuri N, Costa H, Wilhelmi V, Scicluna P, et al. Overexpression of endothelin B receptor in glioblastoma: a prognostic marker and therapeutic target?. *BMC Cancer* 2018;**18**: 154.
136. Delanaye P, Mariat C, Krzesinski JM, Cavalier E. Paricalcitol for reduction of albuminuria in diabetes. *Lancet* 2011;**377**:636−7.
137. Perez-Gomez MV, Sanchez-Niño MD, Sanz AB, Martín-Cleary C, Ruiz-Ortega M, Egido J, et al. Horizon 2020 in diabetic kidney disease: the clinical trial pipeline for add-on therapies on top of renin angiotensin system blockade. *J Clin Med* 2015;**4**:1325−47.
138. Dolman MEM, Harmsen S, Storm G, Hennink WE, Kok RJ. Drug targeting to the kidney: advances in the active targeting of therapeutics to proximal tubular cells. *Adv Drug Deliv Rev* 2010;**62**: 1344−57.
139. Marchetti GM, Burwell TJ, Peterson NC, Cann JA, Hanna RN, Li Q, et al. Targeted drug delivery *via* caveolae-associated protein PV1 improves lung fibrosis. *Commun Biol* 2019;**2**:92.
140. Tkachenko E, Tse D, Sideleva O, Deharvengt SJ, Luciano MR, Xu Y, et al. Caveolae, fenestrae and transendothelial channels retain PV1 on the surface of endothelial cells. *PLoS One* 2012;**7**:e32655.
141. Valadon P, Garnett JD, Testa JE, Bauerle M, Oh P, Schnitzer JE. Screening phage display libraries for organ-specific vascular immunotargeting *in vivo*. *Proc Natl Acad Sci USA* 2006;**103**:407−12.
142. Gow NAR, Latge JP, Munro CA. The fungal cell wall: structure, biosynthesis, and function. *Microbiol Spectr* 2017;**5**. Available from: https://doi.org/10.1128/microbiolspec.funk-0035-2016.
143. Binder CJ, Papac-Milicevic N, Witztum JL. Innate sensing of oxidation-specific epitopes in health and disease. *Nat Rev Immunol* 2016;**16**:485−97.
144. Biel C, Faber KN, Bank RA, Olinga P. Matrix metalloproteinases in intestinal fibrosis. *J Crohns Colitis* 2024;**18**:462−78.
145. Yue TTC, Ge Y, Aprile FA, Ma MT, Pham TT, Long NJ. Site-Specific ^{68}Ga radiolabeling of trastuzumab Fab *via* methionine for immuno-PET imaging. *Bioconjug Chem* 2023;**34**:1802−10.
146. Wissler HL, Ehlerding EB, Lyu Z, Zhao Y, Zhang S, Eshraghi A, et al. Site-specific immuno-PET tracer to image PD-L1. *Mol Pharm* 2019;**16**:2028−36.
147. Weisser NE, Hall JC. Applications of single-chain variable fragment antibodies in therapeutics and diagnostics. *Biotechnol Adv* 2009;**27**: 502−20.
148. Zettlitz KA, Tsai W-TK, Knowles SM, Salazar FB, Kobayashi N, Reiter RE, et al. [^{89}Zr]A2cDb immuno-PET of prostate cancer in a human prostate stem cell antigen knock-in (hPSCA KI) syngeneic model. *Mol Imag Biol* 2020;**22**:367−76.
149. Uehara T, Yokoyama M, Suzuki H, Hanaoka H, Arano Y. A Gallium-67/68-labeled antibody fragment for immuno-SPECT/PET shows low renal radioactivity without loss of tumor uptake. *Clin Cancer Res* 2018;**24**:3309−16.
150. Suzuki H, Kise S, Kaizuka Y, Watanabe R, Sugawa T, Furukawa T, et al. Copper-64-labeled antibody fragments for immuno-PET/radioimmunotherapy with low renal radioactivity levels and amplified tumor-kidney ratios. *ACS Omega* 2021;**6**:21556−62.
151. Schneider DW, Heitner T, Alicke B, Light DR, McLean K, Satozawa N, et al. *In vivo* biodistribution, PET imaging, and tumor accumulation of ^{86}Y- and ^{111}In-antimindin/RG-1, engineered antibody fragments in LNCaP tumor-bearing nude mice. *J Nucl Med* 2009;**50**:435−43.
152. Syvänen S, Edén D, Sehlin D. Cationization increases brain distribution of an amyloid-beta protofibril selective $F(ab')_2$ fragment. *Biochem Biophys Res Commun* 2017;**493**:120−5.

153. Kwon LY, Cai Z, Al-Mahrouki A, Reilly RM. Bispecific radioimmunoconjugates exploit receptor heterogeneity for positron emission tomography of tumors expressing HER2 and/or EGFR. *iScience* 2024;**27**:109750.

154. Bonvicini G, Syvänen S, Andersson KG, Haaparanta-Solin M, López-Picón F, Sehlin D. ImmunoPET imaging of amyloid-beta in a rat model of Alzheimer's disease with a bispecific, brain-penetrating fusion protein. *Transl Neurodegener* 2022;**11**:55.